

TECHNICAL UNIVERSITY OF MUNICH

DEPARTMENT OF PHYSICS

EXPERIMENTAL PHYSICS WITH COSMIC PARTICLES

In-situ study of the ambient background at
Cascadia Basin, Canada, for the Pacific
Ocean Neutrino Explorer

Author:
Nikhita KHERA
Matrikel Nr: 03686229

Supervisor:
Prof. Dr. Elisa RESCONI

July 10, 2019



Abstract

The detection of high energetic cosmic rays and cosmic neutrinos has challenged scientists since their first discovery. New methods and experiments are needed to gain better understanding of the highest energetic processes and particles and new sites for large scale neutrino telescopes need to be tested and probed. We introduce the path finder experiment "STRings for Absorption length in Water" (STRAW), which is situated at the Cascadia Basin site in the Pacific Ocean. In June 2018, STRAW was first deployed by Ocean Networks Canada and has been collecting data since then. The two 120 meters tall mooring lines at a depth of about 2600 meters are instrumented by three light sources POCAMs ("Precision Optical Calibration Modules") and five light sensors sDOMs ("SRAW Digital Optical Module"). In this work, we describe the characterization of the gain, linearity, dark rates and transit time spread of the photomultiplier tubes used in the sDOMs. The main background of STRAW is bioluminescence produced by deep sea organisms. We present the upgrade STRAW-b, which will consist of an additional 450 meter long string with 10 modules. For this upgrade we present the proposed and ongoing design and the investigation of two spectrometer modules. For the stand-alone spectrometer, the response at different distances for different colored LEDs will be presented. On the other hand for the PMT spectrometer, the estimated rates for different wavelengths and there comparison to the sDOM rates will be described. These spectrometers will be deployed to further investigate and examine the background bioluminescent radiation.

Acknowledgement

With boundless respect and appreciation, I would like to extend my heartfelt gratitude to everyone who helped me bring this study into reality. I would like to extend my profound gratitude:

To my professor and adviser, Prof. Dr. Elisa Resconi, whose expertise, consistent guidance, ample time, constant support and consistent advices helped me bring this work into success;

To my supervisor, I.C. Rea, for her constructive comments, suggestions, and critiquing, which helped me improve immensely;

To Kai Krings for always offering a helping hand with software installations and evenly to Christian Fruck for constantly keeping me in touch with programming while answering all my silly queries concerning it;

To Martina Karl for always being warm, friendly and motivating;

To Laura Winter for all the great coffee;

To all the members of ECP for always being open and helpful;

And lastly to my parents, Sushma Khera and Dr. Anil Khera and my sister Natasha, for their unending encouragement, support and understanding.

- Nikhita Khera

Contents

Abstract	i
Acknowledgement	ii
List of Figures	v
List of Tables	viii
1 INTRODUCTION	1
1.1 Cosmic Ray Discovery	1
1.2 Cosmic Ray Spectrum	1
1.3 Air Showers	4
1.4 Detection	4
1.4.1 Cherenkov Detectors	5
1.4.2 Fluorescence Detectors	7
1.4.3 Radio Antennas	8
1.5 Gammas as Cosmic Messengers	8
1.5.1 Bremsstrahlung and Synchrotron Radiation	9
1.5.2 Matter Anti-Matter Annihilation	10
1.5.3 Inverse Compton Scattering	10
1.6 High Energy Gamma Ray Sources	10
1.6.1 Supernova Remnants	10
1.6.2 Pulsars and Pulsar Wind Nebula	11
1.6.3 Active Galactic Nuclei	13
1.6.4 Gamma Ray Bursts	14
1.7 Neutrinos as Cosmic Messengers	15
2 NEUTRINO ASTRONOMY	16
2.1 Motivation to Neutrino Astronomy	16
2.2 Candidate Astrophysical Neutrino Sources	16
2.2.1 Solar Neutrinos	17
2.2.2 Geo-neutrinos	19
2.2.3 Supernova neutrinos	19
2.2.4 Atmospheric Neutrinos	21
2.2.5 Relic Neutrinos	23
2.3 Neutrino Oscillations	23
2.4 Neutrino Interactions	26
2.5 Neutrino Detection	28
2.5.1 KM3NET	29
2.5.2 ICECUBE	30
2.5.3 SUPER-KAMIOKANDE	32
2.5.4 BAIKAL/GVD	34

3	Strings for Absorption Length in Water (STRAW)	36
3.1	STRAW Concept and Design	36
3.1.1	Optical properties of sea water	37
3.2	The Modules	38
3.3	POCAM	40
3.4	SDOM	42
3.4.1	Housing	43
3.4.2	Photomultiplier tubes	44
3.4.3	Detection principle of PMTs	45
3.4.4	PMT Characterization	47
3.4.5	Data readout	57
3.5	Testing, Deployment and First Data	57
4	STRAW-b	60
4.1	Background radiation in the deep-sea	60
4.2	Bioluminescence	61
4.2.1	Bioluminescence spectrum	61
4.3	Motivation for STRAW-b	63
4.4	Modules	64
4.4.1	Standard Module	64
4.4.2	Specialized Modules	65
4.5	Spectrometer Module (I)	65
4.5.1	Mini-spectrometer	66
4.5.2	Preliminary investigation of C12880MA	70
4.5.3	Results	71
4.6	Spectrometer Module (II)	74
4.6.1	Setup	74
4.6.2	Rate estimation	76
5	Conclusion	82



List of Figures

1.1	<i>Victor Hess on a balloon [39]</i>	1
1.2	<i>Flux of cosmic rays vs. energy [121]</i>	2
1.3	<i>Gamma induced and Hadron induced Air Showers [105]</i>	5
1.4	<i>Left: The waves emitted by an electron travelling slower than light in water. The spherical light wave emitted in position (b) does not catch up with the one emitted previously in position (a). Centre: The electron goes faster than light in the medium. The spherical waves catch up, generating a conical wave front which follows the corpuscle. Right: The formula gives the angle of the Cherenkov wavefront with respect to the corpuscle direction as a function of its speed. [7]</i>	6
1.5	<i>(a) Water Cherenkov Detector [59], (b) Imaging Air Cherenkov Telescope from H.E.S.S [18], (c) Schematic view of a fluorescence telescope of the Pierre Auger Observatory [60]</i>	7
1.6	<i>Map of the Pierre Auger Observatory. The four telescope sites are marked in blue with lines indicating the field of view of the telescopes. The surface detector stations are represented by black dots. [119]</i>	8
1.7	<i>The charged particle moving through a magnetic field is accelerated in a circular motion. The synchrotron light is emitted from the electron, causing an energy loss of the particle. Figure taken from [56]</i>	9
1.8	<i>The electron (marked with -) moves into the vicinity of a nucleus (marked with +). The electron is accelerated towards the nucleus and emits bremsstrahlung in the process. Figure taken from [6]</i>	9
1.9	<i>Matter-Antimatter Annihilation [42]</i>	10
1.10	<i>Inverse Compton Scattering [20]</i>	10
1.11	<i>Association between a pulsar and a supernova remnant [29]. The pulsar moves away from its original location, the center of explosion.</i>	12
1.12	<i>Artistic representation of an AGN [4]</i>	14
1.13	<i>Illustration of a gamma-ray burst [13].</i>	15
2.1	<i>pp chain in the Sun [77]</i>	18
2.2	<i>Core collapse supernova [23].</i>	20
2.3	<i>Neutrino production from cosmic rays [99]. The primary particle, the cosmic ray hits a nuclei in the atmosphere. An example particle cascade is depicted in this figure, starting with the decay of two pions and producing atmospheric neutrinos. There are twice as many muon neutrinos produced as electron neutrinos.</i>	21
2.4	<i>An example Feynman diagram of charge current ν_μ interaction [113].</i>	26
2.5	<i>An example Feynman diagram of neutral current ν_μ interaction [113].</i>	27
2.6	<i>Some event signature topologies for different neutrino flavors and interactions in ANTARES. (a)CC ν_μ interaction, (b) CC ν_τ interaction, tracing the double bang signature, (c) CC ν_e interaction and (d) a NC interaction producing a hadronic shower [90].</i>	28
2.7	<i>Impression of the KM3NET detector [21]</i>	30
2.8	<i>Sketch of IceCube detector [58].</i>	31

2.9	<i>The Super-Kamiokande detector, in cutaway, showing the inner and outer detector, partially filled with water [97].</i>	32
2.10	<i>Two simulated events displayed for the Super-Kamiokande detector. Left: a muon event. Notice the cleaner outer ring of the Cherenkov cone. Right: an electron event. Notice that the ring is much more ragged due to the many particles of the electromagnetic shower and multiple scattering of the shower particles [69].</i>	33
3.1	<i>Detailed Sketch of the STRAW strings (courtesy Kilian Holzappel) with precise specifications and geometry of all the modules [70].</i>	39
3.2	<i>Simulation of a POCAM assembly giving aside view of all its components [93].</i>	40
3.3	<i>Final POCAM module prior to shipment to Canada. Visible is the housing, one integrating sphere, the mounting structures and the instrument connector including its safety clamp [70].</i>	41
3.4	<i>(left) sDOM housing design by F. Henningsen [92], (right) The interior design of the sDOM showing the upper half with the PMT and its electronics mounted under the aluminium plate [70].</i>	42
3.5	<i>Hamamatsu PMT R12199 [26].</i>	43
3.6	<i>PMT base C12842-02 MOD [117]</i>	43
3.7	<i>Dimensional outline and basing diagram [117].</i>	45
3.8	<i>Cross section of a head on type PMT [118].</i>	46
3.9	<i>Spectral response parameters for R12199 (peak at 420 nm) [94].</i>	47
3.10	<i>Setup scheme for the characterization of the PMTs [94].</i>	48
3.11	<i>Typical Gain characteristics of R12199 [94].</i>	49
3.12	<i>(a)Single photoelectron distribution at 1300 V and (b) Gain vs. supply voltage for AC4082.</i>	50
3.13	<i>Gain vs. supply voltage for every PMT (tested with its own socket) of STRAW [70].</i>	50
3.14	<i>Dark rate trend in Hz for one of the sDOM PMTs [94].</i>	52
3.15	<i>Saturation trend for three sDOM PMTs. Number of electrons vs the input Light Power(W)</i>	54
3.16	<i>Saturation at different values of HV. Anode charge divided by the gain in units of elementary charge (e- collected at the first dynode) vs. the number of photons impinging on the PMT [70].</i>	55
3.17	<i>Setup for TTS measurement [94].</i>	55
3.18	<i>Transit time spread trend at different HV for some PMTs used in STRAW: the value decreases with the increasing power supply [94].</i>	56
3.19	<i>Dark rates recorded by all five sDOMs for five minutes at a readout rate of 3 Hz. In this representation the fine structure of the flashes most likely caused by bioluminescence are visible [70].</i>	58
4.1	<i>Representative spectra from extremes of each group of zooplankton (a) ctenophores with extremes at 464 nm and 502 nm. (b) medusae with extremes at 441 nm and 502 nm, irregularity in the second spectrum is due to smoothing of relatively noisy signal. (c) siphonophores: in this group, several species produced two colors of luminescence; surprisingly, Bargmannia elongata which emitted blue light (446 nm) and green light (493 nm) provided best examples of both extremes for siphonophores [88].</i>	62
4.2	<i>Relationship between wavelength of maximum emission and depth [88].</i>	63
4.3	<i>Pyrosome entangled on the STRAW string [courtesy I.C.Rea]</i>	63
4.4	<i>STRAW-b string outline [Courtesy C. Spannfellner].</i>	64
4.5	<i>Sketch of the standard module in STRAW-b showing the mounting system and the glass sphere with the lower half for the electronics and upper half for the specialized instrumentation [Courtesy C. Spannfellner].</i>	65
4.6	<i>Mini spectrometer C12880MA from Hamamatsu [5].</i>	66

4.7	<i>Dimensional sketch (units:mm) of C12880MA [108].</i>	67
4.8	<i>(top): C12880MA structure, (bottom): Exemplary connection of C12880MA on the circuit board C13016 connected via USB to the computer. [108]</i>	68
4.9	<i>Wavelength - pixel relationship for C12880MA</i>	69
4.10	<i>Setup within the dark box showing an LED matrix that sends light through the teflon sphere to the spectrometer and the photodiode placed symmetrically on either side of the integrating sphere axis.</i>	70
4.11	<i>Closeup of the photocathode and mini-spectrometer arrangement</i>	70
4.12	<i>The dark rate spectrum (grey), the total spectrum (pink) and the dark rate subtracted spectrum (green) of the 374 nm LED at 0 cm from the integrating sphere and 1 s integration time</i>	71
4.13	<i>Another dark rate spectrum (grey), the total spectrum (pink) and the dark rate subtracted spectrum (green) of the 613 nm LED at 50 cm from the integrating sphere and 1 s integration time</i>	72
4.14	<i>Distance vs. counts for 374nm</i>	73
4.15	<i>(left) Distance vs. counts for 405 nm (right) Distance vs. counts in log scale for 405 nm</i>	73
4.16	<i>(left) Distance vs. counts for 465 nm (right) Distance vs. counts in log scale for 465 nm</i>	73
4.17	<i>(left) Distance vs. counts for 613nm (right) Distance vs. counts in log scale for 613nm</i>	74
4.18	<i>Hamamatsu R1924A 1 inch PMT [103].</i>	74
4.19	<i>Specifications of the PMT spectrometer</i>	75
4.20	<i>(left) Top view sketch of the spectrometer module. Black rings are the bandpass filters and the numbers on the axis are to get an idea of the dimensions of the components (right) 3D sketch of the module (Courtesy C. Spannfellner)</i>	75
4.21	<i>Choice range of filters based on an exemplary bioluminescence spectrum taken from [88]. The x-axis is the wavelength in nm and y-axis is the relative intensity</i>	76
4.22	<i>Quantum efficiency of the PMT R1924A [103].</i>	77
4.23	<i>Bioluminescence spectrum of nectophores [88].</i>	77
4.24	<i>Transmittances of all the bandpass filters used [17].</i>	78
4.25	<i>Rate comparison between STRAW sDOMs and PMT spectrometer. Here x-axis is the wavelength in nm and y-axis represents the rate in Hz.</i>	79
4.26	<i>Rate estimation at different wavelngths</i>	80



List of Tables

3.1	<i>PMT R12199 Specifications</i> [117],[94]	44
4.1	Mean wavelengths of luminescence for groups of organisms tested [88]	63



INTRODUCTION

1.1 Cosmic Ray Discovery

Ionizing radiation was assumed to be coming from the radioactivity in the Earth, until in 1909, Theodor Wulf, with an electrometer, measured that the radiation does not drop on the Eiffel tower as much as was expected. This led him to think whether there was another component of radiation coming from elsewhere [102].

To test Wulf's discovery, Austrian physicist Victor Hess, in the year 1911-12 made a series of ascents in a balloon, taking measurements of the radiation in the atmosphere at different altitudes. But he found "no essential change" [39]. In April 1912, during a near-total eclipse of the Sun, when Hess ascended to 5300 meters and saw no decrease in the radiation he reasoned that since the radiation could not be coming from the sun, it had to be coming from further out in space. He reported "The results of my observation are best explained by the assumption that a radiation of very great penetrating power enters our atmosphere from above" [40], for which he received a Nobel Prize in 1936.



Figure 1.1: *Victor Hess on a balloon*
[39]

1.2 Cosmic Ray Spectrum

Earth's surface is constantly hit by highly energetic particles that travel through the

Milky Way including our solar system - called *Cosmic Rays*. *Primary cosmic rays*, which are those originally produced in various astrophysical processes, are mostly protons, 10% of the primaries are helium nuclei and less than 1% are heavier nuclei of elements such as carbon, iron and lead. When this primary cosmic ray interacts with the Earth's atmosphere showers of photons, electrons, pions, positrons, and muons are produced. This cascade of secondary interactions are called *secondary cosmic rays*. [40]

Figure 1.2 shows how the cosmic ray flux changes with energy. The more energetic a cosmic ray is, the rarer it is. Cosmic rays have been observed to have energies from 10^9 eV to over 10^{20} eV. Over this range the flux ϕ of cosmic rays (i.e. the number of particles arriving per unit area per solid angle per unit time) falls off with a power law,

$$\phi \propto e^{-\gamma} \quad ; \quad \gamma \sim 2.7 - 3.1 \quad (1.1)$$

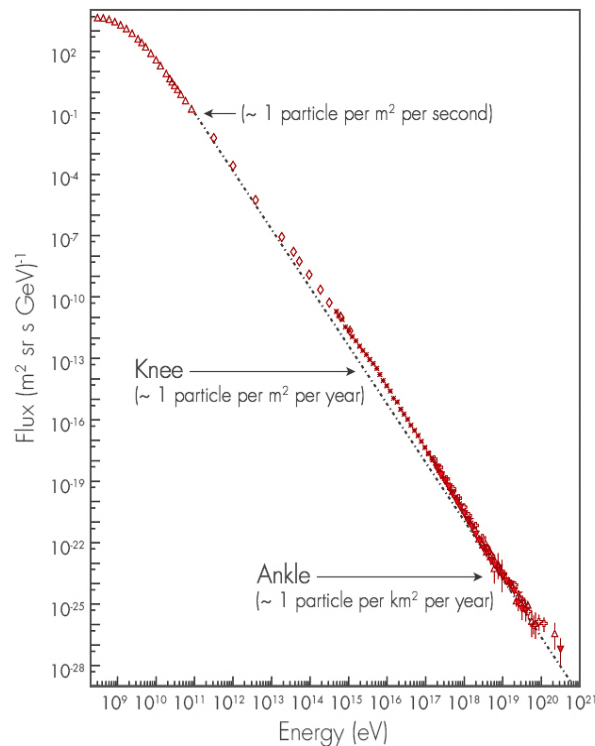


Figure 1.2: Flux of cosmic rays vs. energy [121]

The curve is nearly smooth with the exception of three noticeable points called the – *Knee*, *Ankle* and *the GZK cutoff*, where its slope changes.

The origin of these changes in the steepness of the spectrum is still the subject of intense study, but it is assumed that they distinguish between populations of cosmic rays originating from different mechanisms [9]. Current suggestions are that the cosmic rays with energies less than about 10^{10} eV are primarily solar cosmic rays produced in solar flares, while those with energies between 10^{10} eV and the knee at 10^{15} eV are galactic cosmic rays produced in the shocks of supernova remnants (*mechanism: Fermi acceleration*). The origin of the cosmic rays with energies between the knee and ankle is unclear ; they are thought to be produced within the Galaxy, but the energies are too high for them to be accelerated by the shocks of supernova remnants. The origin of the ultra-high energy cosmic rays (UHECRs) below the ankle is also unknown, but many have suggested that these may be created outside of our galaxy [9].

Thus from the knee to the ankle there is a transition from galactic sources to extra-galactic sources (active galactic nuclei, gamma ray bursts etc). In this case, the existence of UHECRs with energies above 5×10^{19} eV shows a clear cut off that is in agreement with the GZK but it is not yet clear if this is due to the GZK or it is caused by the intrinsic spectra of the sources. At energies beyond this Greisen-Zatsepin-Kuzmin limit (GZK limit), cosmic rays should interact with the radiation of the cosmic microwave background. Due to this interaction, the energy of the cosmic rays is reduced to values below the GZK limit also called the GZK cutoff or source exhaustion [16].

The acceleration of cosmic rays occurs mainly due to a shock driven acceleration (*first order fermi acceleration*), which is a fundamental process found on any scale in the universe: from solar flares to star explosions (supernovae) to rapidly spinning stars (pulsars) to the emissions of super-bright galaxies known as *active galactic nuclei* [121]. All are cases of matter flowing faster than the speed of sound, producing an expanding shock wave that accumulates cosmic ray particles (protons and others). The particles reflect back and forth across the shock wave, trapped between the magnetic field of the plasma and the vacuum of empty space, gradually gaining energy with every bounce and eventually escaping [121].

1.3 Air Showers

High energy primary cosmic ray particles interact with air nuclei near the top of the atmosphere, initiating a cascade of secondary interactions that yield a shower of electrons, photons and muons [49]. These air showers can be gamma induced or hadron induced.

Gamma induced air showers, also called *Electromagnetic Showers*, start with electron-positron *pair production*. These $e^+ - e^-$ pairs radiate new gamma rays via the process of *bremsstrahlung*, which further undergo pair production, thereby increasing the number of e^+ , e^- , and γ .

In a *hadron induced shower*, a high energy proton interacts with atmospheric particles, producing pions and kaons, which being unstable, further generate hadronic, muonic and electromagnetic components of the air shower. The decays involved are,

$$\pi^0 \longrightarrow \gamma + \gamma, \quad (1.2a)$$

$$\pi^+ \longrightarrow \mu + \nu_\mu, \quad (1.2b)$$

$$K^+ \longrightarrow \mu + \nu_\mu, \quad (1.2c)$$

$$K^\pm \longrightarrow \pi^\pm + \pi^0. \quad (1.2d)$$

The air shower profile and spread reveals the primary particle responsible for its generation i.e. a hadron or a gamma. Hadronic showers spread wider than electromagnetic showers as can be seen in Figure 1.3. The lateral distribution of the shower provides information about its energy and the direction while the longitudinal profile depends on its energy as well as its composition. The Gaisser–Hillas function, can parameterize the longitudinal profile of the number of charged particles [44].

1.4 Detection

Arriving cosmic ray particles travel at high energies and therefore their velocities are near the speed of light. Hence the products of the collision tend to move in the same direction as that of the primary, spreading laterally to some extent. The forward moving secondaries, when travelling faster than light in the given medium, tend to produce a widespread flash of light due to *the Cherenkov effect*. Some secondary particles in air may also emit

fluorescence light due to their interaction with the nitrogen molecules in air. [65]

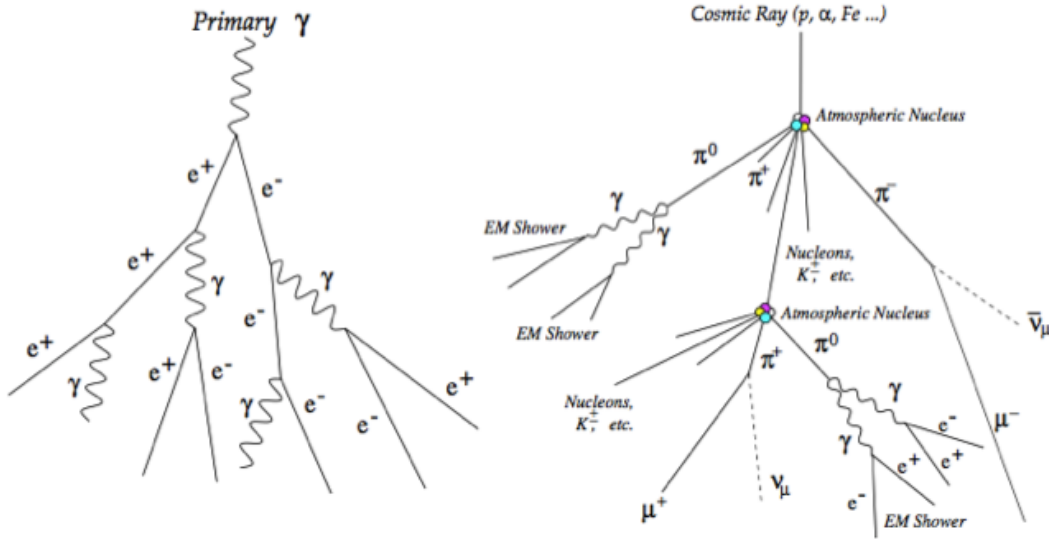


Figure 1.3: *Gamma induced and Hadron induced Air Showers* [105]

1.4.1 Cherenkov Detectors

When a charged particle moves inside a polarizable medium, it excites its molecules higher energy states. Upon returning to their ground state, the molecules emit some photons in the form of electromagnetic radiation. According to the Huygens principle, the emitted waves move out spherically at the phase velocity of the medium. If the particle motion is slow, the radiated waves bunch up slightly in the direction of motion, but they do not cross. However if the particle moves faster than the light speed, the emitted waves add up constructively leading to a coherent radiation at angle θ with respect to the particle direction, known as Cherenkov radiation. [62]

The signature of the effect is a cone of emission in the direction of particle motion. Figure 1.4 shows a schematic of the Cherenkov radiation showing the typical spherical wavefront and the resulting radiation. The number of photons from Cherenkov radiation at a given wavelength and the angle of radiation is given by

$$\frac{\partial^2 N}{\partial x \partial \lambda} = 2\pi\alpha \left[1 - \frac{1}{\beta^2} \right] \frac{1}{\lambda^2}, \quad (1.3)$$

where $\alpha = 1/137$ is the fine structure constant [62]. Unlike the fluorescence or emission spectra, the Cherenkov radiation spectrum given by the above formula is continuous and its density is inversely related to the wavelength squared. Therefore, the number of photons increases as the wavelength decreases. That explains why most of the Cherenkov radiation seems blue and mostly in UV range.

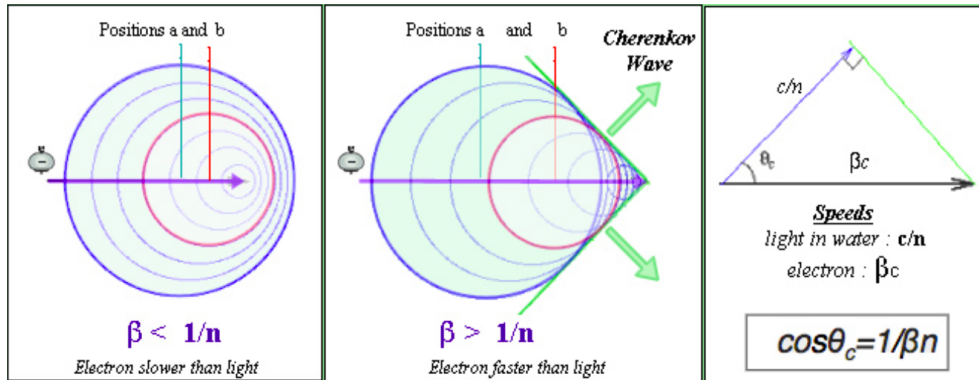


Figure 1.4: Left: The waves emitted by an electron travelling slower than light in water. The spherical light wave emitted in position (b) does not catch up with the one emitted previously in position (a). Centre: The electron goes faster than light in the medium. The spherical waves catch up, generating a conical wave front which follows the corpuscle. Right: The formula gives the angle of the Cherenkov wavefront with respect to the corpuscle direction as a function of its speed. [7]

1.4.1.1 Water Cherenkov Detector

Water cherenkov detectors principally detect the Cherenkov light from the air shower particles in the water tanks built on the ground (Figure 1.5a). This detection is relatively efficient in water due to its high refractive index. The Cherenkov light is emitted into a forward cone that surrounds the direction of motion of the charged particle, which is then detected by the PMTs that are located in these detector tanks. The energy of the primary cosmic ray particle can hence be determined based on the amount of light that is detected by the PMTs whereas the timing gives the information about the direction of the cosmic rays [59]. Various experiments use water Cherenkov detectors, the most prominent one being The Pierre Auger Observatory [64].

1.4.1.2 Air Cherenkov Detector

Air Cherenkov Detectors also called *IAC*Ts (Imaging Air Cherenkov Telescopes) (Figure 1.5b), map the Cherenkov light from air showers with large

mirrors onto a fast camera in the focal plane of the mirrors and thereby measure the angular distribution of the Cherenkov light from the air shower [18]. IACTs are a part of many gamma ray astronomy experiments like MAGIC, H.E.S.S, CTA etc.

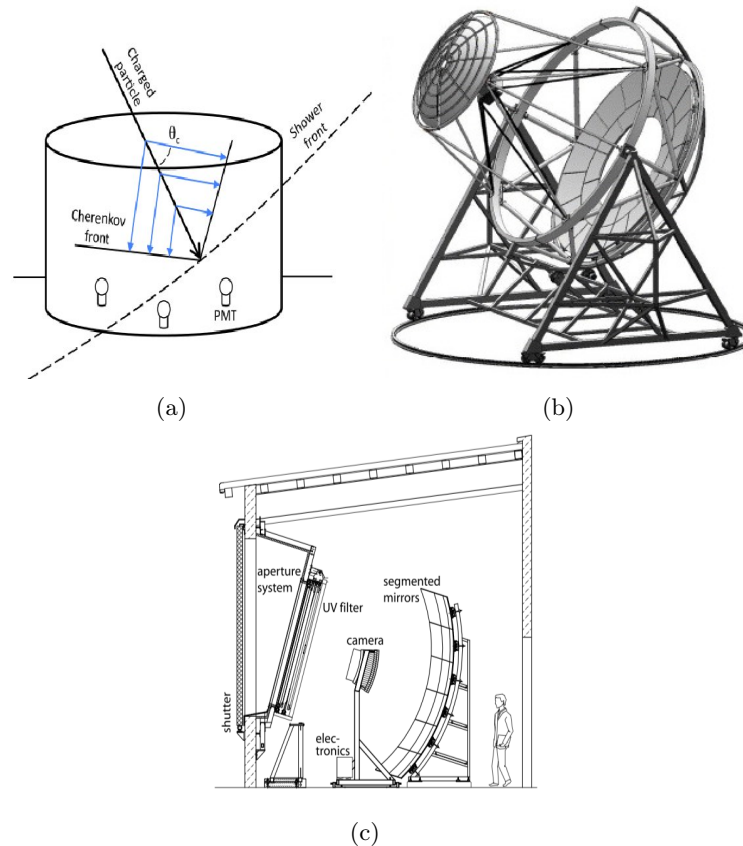


Figure 1.5: (a) Water Cherenkov Detector [59], (b) Imaging Air Cherenkov Telescope from H.E.S.S [18], (c) Schematic view of a fluorescence telescope of the Pierre Auger Observatory [60]

1.4.2 Fluorescence Detectors

The charged particles in air showers also interact with atmospheric nitrogen, causing it to emit ultraviolet light via a process called fluorescence. This light is invisible to the human eye - but not to the optical detectors. This detection method uses these detectors to observe the trail of *nitrogen fluorescence* and track the development of air showers by measuring the brightness of the emitted light. By studying the longitudinal profile of the showers, these detectors yield information about the composition of air showers [19]. Pierre Auger Observatory uses 27 such fluorescence detectors at four different places (Figure 1.5c). Figure 1.6 shows the map

of the detector sites of Pierre Auger Observatory [119].

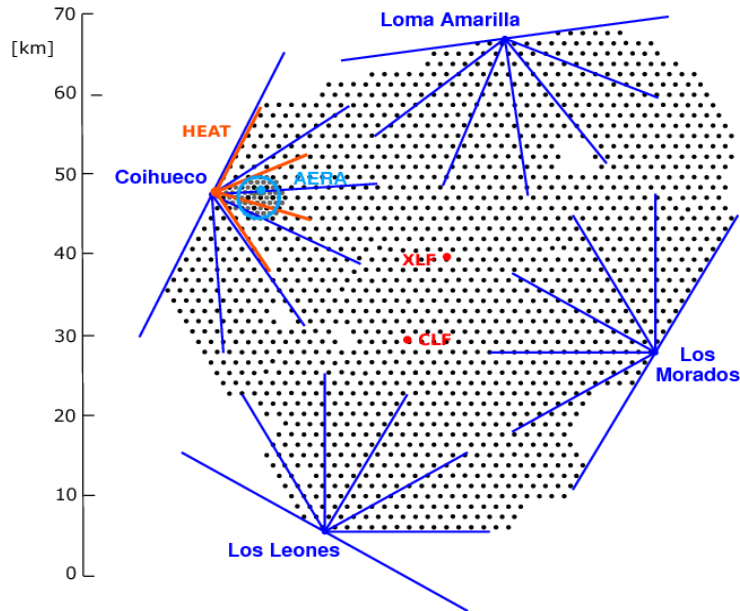


Figure 1.6: *Map of the Pierre Auger Observatory. The four telescope sites are marked in blue with lines indicating the field of view of the telescopes. The surface detector stations are represented by black dots. [119]*

1.4.3 Radio Antennas

Finally, air showers emit radio waves due to the deflection of electrons and positrons by the geomagnetic field. As advantage over the optical techniques, radio detection is possible at all times and not only during dark and clear nights. Thus, several modern experiments, e.g., Tunka Rex of TAIGA (Tunka Advanced Instrument for cosmic ray physics and Gamma Astronomy) [112], LOFAR (Low Frequency Array) [82], or the Pierre Auger Observatory [91] use radio antennas in addition to particle detectors and optical techniques. [38]

1.5 Gammas as Cosmic Messengers

Gamma ray astronomy is the observation of cosmic photons with energies above 100 keV [50]. Gammas above 30 GeV are referred to as very high energy (VHE) gamma-rays. They point towards their sources as long as the energy doesn't get too high. With increasing energy, gammas are more likely to get absorbed in electron pair production interactions with ambient radiation fields. In their sources, VHE γ -rays can be produced

through various processes [61]. These processes are briefly explained in the following sections.

1.5.1 Bremsstrahlung and Synchrotron Radiation

A magnetic field could exert a force on a charged particle moving in it causing the particle to radiate, often in the gamma-ray region of the electromagnetic spectrum. If the electron is accelerated in the electrostatic field around a nucleus it is called *bremstrahlung* (Figure 1.8). When the acceleration takes place in a static magnetic field the process is called *synchrotron radiation* (Figure 1.7). Supernovae and supernova remnants produce a lot of synchrotron radiation. [120] [27]

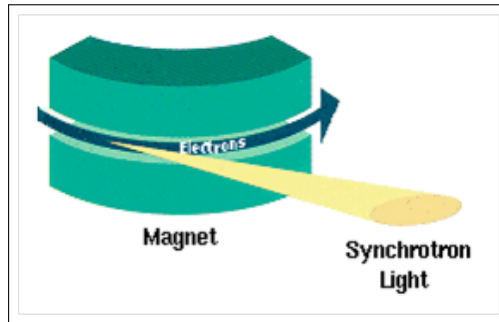


Figure 1.7: The charged particle moving through a magnetic field is accelerated in a circular motion. The synchrotron light is emitted from the electron, causing an energy loss of the particle. Figure taken from [56]

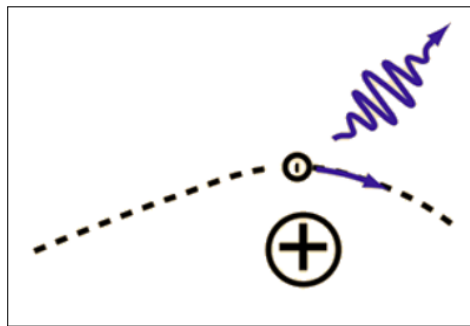


Figure 1.8: The electron (marked with -) moves into the vicinity of a nucleus (marked with +). The electron is accelerated towards the nucleus and emits bremsstrahlung in the process. Figure taken from [6]

1.5.2 Matter Anti-Matter Annihilation

As shown in figure 1.9 when a particle of matter collides with its anti-matter twin, they annihilate each other. This *matter-antimatter annihilation* produces a pair of gammas of a specific wavelength depending on the mass of the annihilating particles.

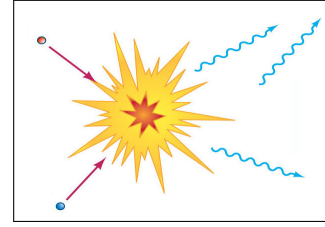


Figure 1.9: Matter-Antimatter Annihilation [42]

1.5.3 Inverse Compton Scattering

Inverse Compton Scattering occurs when a photon and an energetic charged particle (say an electron) scatter off of each other (figure 1.10). In this process, the kinetic energy of the particle can be transferred to the photon and hence can increase its energy into the γ ray regime [36].

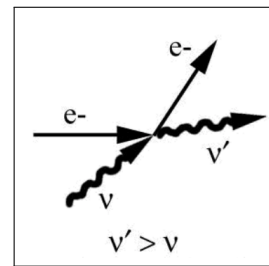


Figure 1.10: Inverse Compton Scattering [20]

1.6 High Energy Gamma Ray Sources

After years of theoretical studies and rigorous experimenting, the knowledge about the galactic cosmic ray sources still remains rather limited. The main complication in determining the production sites and acceleration mechanism of cosmic rays arises from the diffusion of charged particles in interstellar magnetic fields. The charged particles in the cosmic rays lose their directional information on their way from the source to Earth. Also the original source spectra of accelerated particles are significantly modified by this diffusion. Neutrinos and γ rays - the uncharged components of the cosmic radiation, thus hold the power to directly reveal the sites of particle acceleration. [85]

Before moving on to neutrino astronomy, this section will cover a very brief and phenomenological introduction to some known or potential sources - both galactic and extra galactic - of very high-energy γ rays.

1.6.1 Supernova Remnants

Although the exact nature of cosmic-ray sources in the Galaxy is not yet firmly well known, supernova remnants are contemplated to be the most

plausible candidates both from the theoretical and the observational point of view [116]

A supernova remnant (SNR) is a diffuse, expanding nebula that results from a supernova explosion [34]. It is bounded by an expanding shock wave and consists of ejected material expanding from the explosion and the interstellar material it sweeps up and shocks along the way [55]. Although not necessarily visible at optical wavelengths, SNRs tend to be powerful X-ray and radio emitters due to interactions with the surrounding interstellar medium. They typically last several hundred thousand years before dispersing into the interstellar medium, during which time they evolve [116].

The shockwave accelerates electrons, protons and ions, via the process of Fermi acceleration, to velocities very close to the speed of light. It is believed that most cosmic rays in our galaxy are a part of the gas in the interstellar medium, until they are caught in a supernova shock wave. By rattling back and forth across the shock wave, these particles gain energy and become highly energetic cosmic rays [33]. At the site of the 1054 supernova is one of the most remarkable objects in the sky, *the Crab Nebula*, now about 10 light-years across [35]. It is one of the most famous SNR.

1.6.2 Pulsars and Pulsar Wind Nebula

A supernova explosion can leave behind two bits of evidence for its passing: a pulsar and a supernova remnant [29].

A *pulsar* is a spinning neutron star, about 1.4 times as massive as the Sun but with a diameter of only 20 kilometers. Pulsars release enormous amounts of energy in terms of a strong plasma wind and relativistic particles [106]. They have very strong magnetic fields which funnel jets of particles out along the two magnetic poles. These accelerated particles produce very powerful beams of light - like from a rotating lighthouse [24].

A pulsar also has a wind, and charged particles, sometimes accelerated to near the speed of light, form a nebula around the pulsar: *a Pulsar Wind Nebula (PWN)* [43]. Processes creating pulsar wind nebulae are complicated and they evolve through various phases before creating a so-called relic nebula, which is visible as a wind bubble, shell nebula, or as a bow-shock [45]

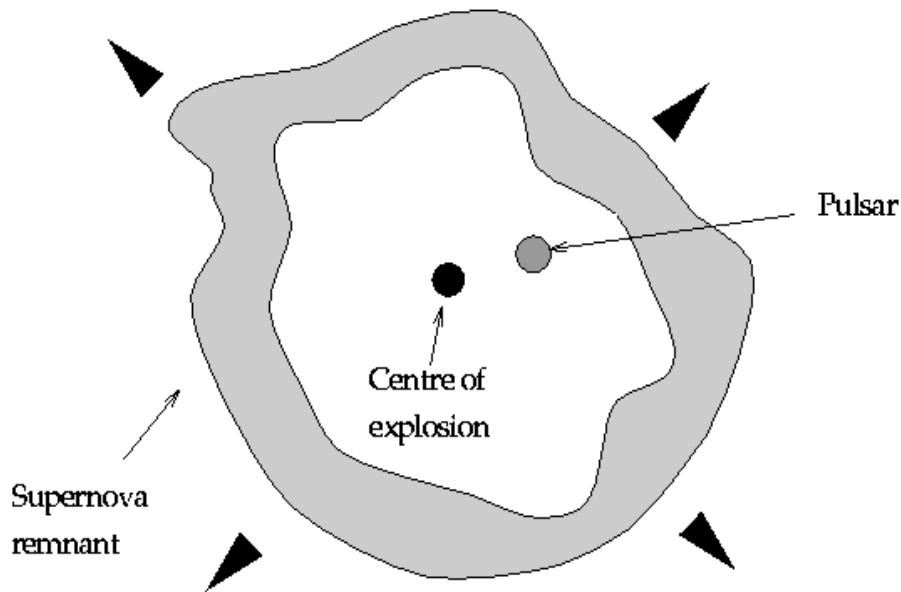


Figure 1.11: Association between a pulsar and a supernova remnant [29]. The pulsar moves away from its original location, the center of explosion.

The emission from PWN can be divided into two broad categories – one originating from the relativistic particles within the nebula and the other produced by material that has been swept up by the nebula. The former is a combination of synchrotron radiation and Inverse Compton radiation associated with the up-scattering of ambient photons. The latter however is a result of the expanding PWN into the surrounding supernova ejecta, which heats the ejecta. The resulting emission is a combination of radiation from shocked gas and continuum emission from dust condensed from the cold ejecta in the early adiabatic expansion of the SNR [114].

The Crab Nebula is the best-known member of this class; indeed, it is generally regarded as the ‘standard candle’ for high-energy astrophysics. Its emission over more than 15 decades in energy shows it to be an effective particle accelerator [28]. Figure 1.11 shows a sketch of an association between a pulsar and a supernova remnant. Pulsars generally move away from the center of the supernova remnant with which they are associated, since they usually have quite high velocities [29].

1.6.3 Active Galactic Nuclei

The supremely massive representative of compact accreting objects is the so-called Active Galactic Nuclei (AGN). They are a candidate source of high and ultra-high energy cosmic rays [46]. AGN reside amongst the most luminous objects in the universe. They source their energy from accretion processes onto super-massive black holes of 10^6 to 10^9 of solar masses. While they are typically accreting about two solar masses per year, they release an immense amount of radiated energy. Much of the energy output of AGNs is of a non-thermal (non-stellar) type of emission, with many AGN being strong emitters of X-rays, radio and ultraviolet radiation, as well as optical radiation. Most of this energy is emitted from a region that is by a factor 10^8 more compact than the host galaxy. [11]

AGN can vary in luminosity on short (hours or days) timescales. This means that the light or energy-emitting source must be of order light hours or light days (respectively) in size, and gives clues as to the energy mechanism [3].

Numerous subclasses of AGN have been defined based on their observed characteristics. They are thought to be powered by supermassive black holes, which lie at the center of massive galaxies. However, the black holes themselves do not emit visible or radio light (i.e. they are “black”) – the light we see from AGNs comes from a disk of gas and stars called an accretion disk, which surrounds the black hole. Intense heat and light is emitted from this accretion disk, caused by friction produced from the material swirling around, and eventually into, the black hole.

AGNs are typically more than 100 times brighter than their host galaxies. They also emit jets from their central regions, which can be larger in extent than the host galaxy. When an AGN jet interacts with the gas surrounding the galaxy, radio waves are emitted which can be seen as “radio lobes” by radio telescopes [30].

1.6.3.1 Blazar

A blazar is an AGN with its jets pointing at the earth. Like other forms of active galactic nuclei (AGN), blazars are the most luminous and energetic objects in the known universe [37].

Figure 1.12 (adapted from [4]) shows an artistic representation of an

Active Galactic Nuclei. The central black region shows the supermassive black hole. The accretion disc around the black hole consists of rotating material, the heat and friction of the particles producing luminosities outshining the host galaxy. The jet is indicated with blue lines, being emitted perpendicular to the accretion disc.

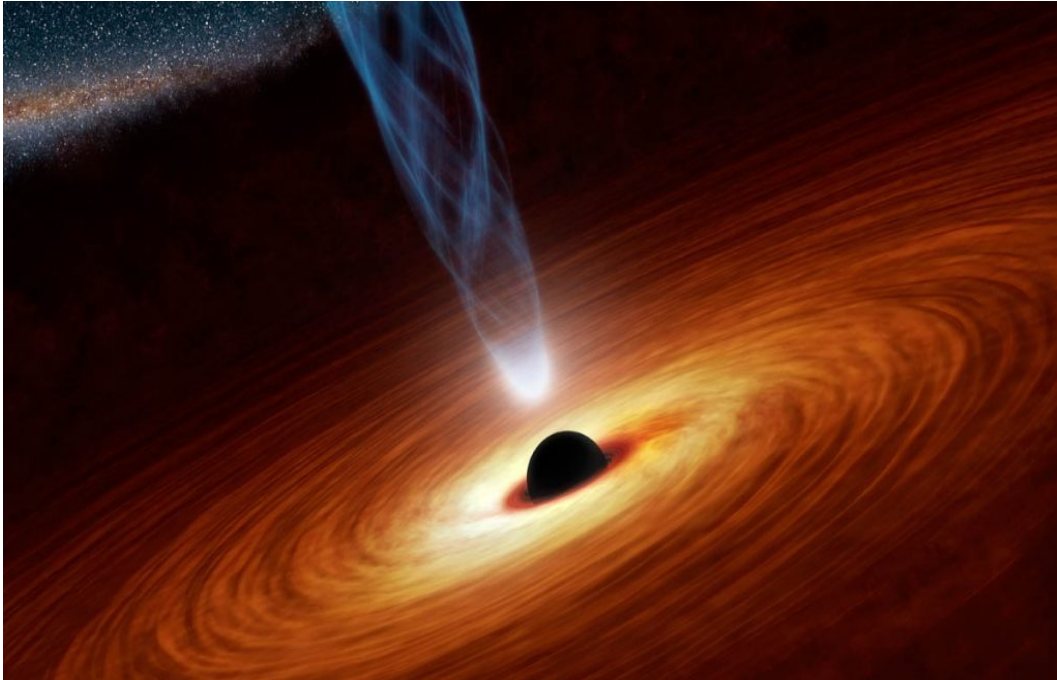


Figure 1.12: *Artistic representation of an AGN [4]*

1.6.4 Gamma Ray Bursts

Another possible source candidate of UHECRs are Gamma Ray Bursts (GRBs). A GRB is an astrophysical phenomenon of a short, but very intense flare of gamma rays from space [67]. Gamma ray astronomers have observed these explosions, which are extremely energetic, in various distant galaxies. According to the internal shock model, the prompt emission in gamma-rays is expected to come from internal collisions inside the ejected material, accelerating particles to the highest energies [67]. GRBs shine hundreds of times brighter than a typical supernova and about 10^{18} times brighter than the Sun. When a GRB erupts, it is briefly the brightest source of cosmic gamma-ray photons in the observable Universe [14].

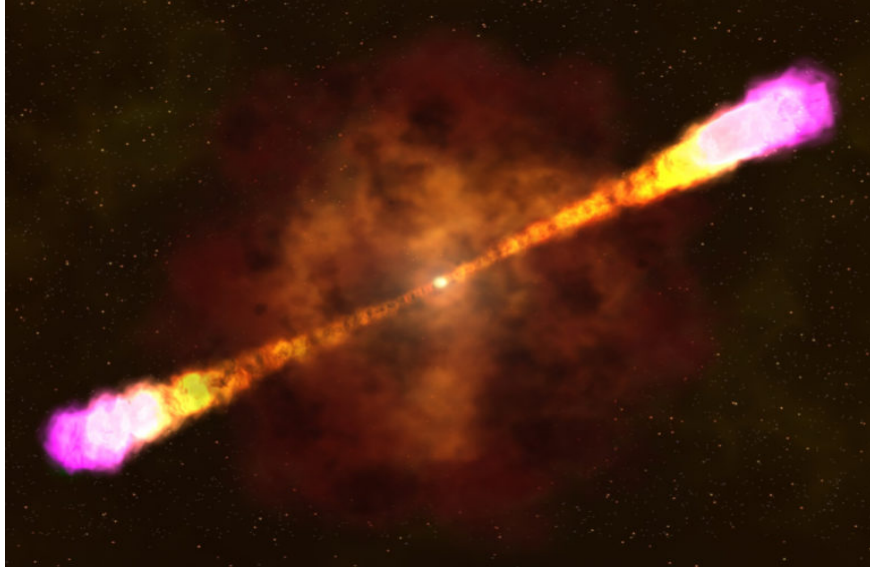


Figure 1.13: *Illustration of a gamma-ray burst [13].*

GRBs can last from ten milliseconds to several hours. After an initial flash of gamma rays, a longer-lived "afterglow" is usually emitted at longer wavelengths (X-ray, ultraviolet, optical, infrared, microwave and radio) [51]. Figure 1.13 shows the most common type of gamma-ray burst, thought to occur when a massive star collapses, forms a black hole, and blasts particle jets outward at nearly the speed of light.

1.7 Neutrinos as Cosmic Messengers

Just like gammas, neutrinos are expected to be produced in both galactic and extragalactic objects. For example, they are produced in the processes that power stars, the most near-by of them being our Sun. It emits electron neutrinos with energies in the MeV range. These neutrinos have been observed by several experiments like the Super-Kamiokande experiment [84], Borexino [63] and Sudbury Neutrino Observatory [71] and have been used to study properties of the neutrinos itself, like the oscillation between different leptonic flavors of neutrinos [107].

In the subsequent chapter we talk more meticulously about neutrinos, discussing a few potential sources of high energy neutrinos, followed by introduction to neutrino oscillations, neutrino production models and finally giving a brief overview of some currently running neutrino telescopes.



NEUTRINO ASTRONOMY

2.1 Motivation to Neutrino Astronomy

The disadvantage of classical astronomies like observations in the radio, infrared, optical, ultraviolet, X-ray, or gamma-ray band is related to the fact that electromagnetic radiation is quickly absorbed in matter. Neutrinos on the other hand have extremely small interaction probabilities which proves to be an advantage for astronomy.

The optimal astronomical messenger:

- Should not be influenced by magnetic fields.
- Should not decay from source to Earth.
- Must be penetrating so that one can look into the central part of the sources.
- Should not be absorbed by interstellar or intergalactic dust or by infrared or blackbody photons. [87]

These four requirements are fulfilled by neutrinos and hence make them ideal cosmic messengers. As mentioned above neutrinos have very small cross section with matter, which enables them to escape very dense astrophysical environments, where e.g. photons can be trapped. This small interaction cross section however, also makes them hard to detect. To facilitate neutrino detection one needs huge detection volumes. [83]

2.2 Candidate Astrophysical Neutrino Sources

If the sources and acceleration mechanisms of charged cosmic rays or VHE γ -rays involved hadronic interactions, they could also be sources of highly

energetic neutrinos [107].

Neutrinos are known to be coming from both artificial and natural sources. The two principal types of artificial neutrino sources are fission reactors, producing electron-type anti-neutrinos from beta decays of fission fragments, and proton accelerators, producing muon neutrinos (or antineutrinos) from pion decays in flight.

However, one of the most important discoveries in neutrino physics, the phenomenon of neutrino oscillations, came about not through the use of artificial neutrino sources, but by using neutrinos produced naturally in the Sun and in the Earth's atmosphere. Astrophysical neutrinos can provide information both on the physics of neutrinos and on important astrophysical phenomena such as supernovae and active galaxies. [100] [78]

2.2.1 Solar Neutrinos

In this section, we introduce the theoretical description of the solar neutrinos.

Solar neutrinos are produced in the core of the Sun through various nuclear fusion reactions, each of which occurs at a particular rate and leads to its own spectrum of neutrino energies. The main contribution comes from the proton-proton reaction [54].



This p-p reaction is dominant in light stars like our Sun. The pp neutrinos amount to more than 90% of the solar neutrino flux coming to Earth. The fusion of proton plus proton (pp) to deuterium plus positron plus neutrino is responsible for 98% of the energy production of the sun. Therefore these pp-neutrinos are the most plentiful, and the most reliably estimated. [1]

The neutrino flux from the Sun is enormous: about 60 billion per square centimetre per second. Even given the neutrino's reluctance to interact, it seems that detecting solar neutrinos should be a reasonably practical task. Unfortunately, the vast majority of pp neutrinos have very low energy, $< 0.42\text{MeV}$. Most methods of neutrino detection are not sensitive to such low-energy neutrinos, so most experiments rely on the higher energy ${}^7\text{Be}$

and ^8B neutrinos produced in the pp-II and pp-III side chains (the pep and hep neutrinos (Figure 2.1) also have high energies, but are very rare). [77]

The Sun is a pure electron – neutrino source. It does not produce electron antineutrinos and, in particular, no other neutrino flavours. Solar neutrinos have been instrumental in studying neutrino oscillations; results from solar neutrino experiments are still a key input into calculations of neutrino mixing angles. Some experiments that are trying to measure the flux of solar neutrinos are GALLEX, SAGE, Borexino and Super-Kamiokande. [78]

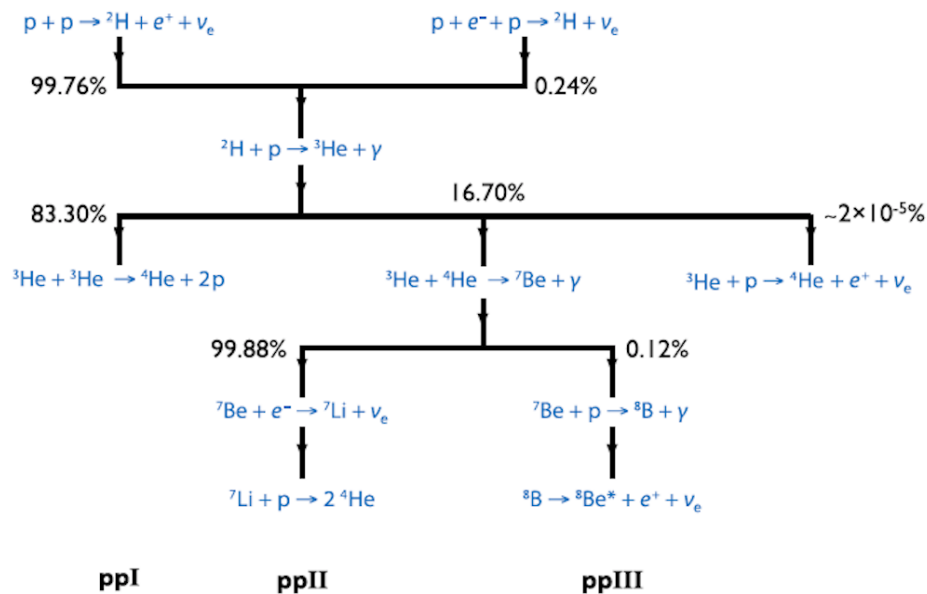


Figure 2.1: *pp chain in the Sun* [77]

2.2.1.1 The Solar neutrino problem

An interesting thing happened when scientists started looking for the electron neutrinos from the Sun in the 1960s. Only about one third to one half of the predicted number of neutrinos actually showed up in detectors. This was called *the solar neutrino problem* [31]. As measurements of the sun improved and the solar model was validated, researchers looked more and more to new physics beyond the Standard Model to explain the neutrino deficit. The breakthrough came with data from two experiments-Super-Kamiokande and the Sudbury Neutrino Observatory - that discovered the

solution to the solar neutrino problem: *neutrino oscillations*. Roughly two-thirds of the electron neutrinos coming from the sun change their flavor as they travel, arriving as muon or tau neutrinos. Evidence that neutrinos changed type also proved that they have mass, something not predicted by the Standard Model. [31]

2.2.2 Geo-neutrinos

A geoneutrino is a neutrino or antineutrino emitted in decay of radionuclide naturally occurring in the Earth. Most geoneutrinos are electron antineutrinos originating in β -decay branches of ^{40}K , ^{232}Th and ^{238}U . Together these decay chains account for more than 99% of the present-day radiogenic heat generated inside the Earth [52]. Even though the geo-neutrino flux at the Earth surface is some $10^6 \text{cm}^{-2} \text{s}^{-1}$, their detection is challenging as antineutrinos interact with matter only through the weak interaction, thus the probability of such interactions, and possible detection, is very small [68].

Scientists at the KamLAND experiment in Japan and the Borexino detector in Italy have been studying geoneutrinos, though not exclusively. Researchers spot geoneutrinos when an antineutrino smacks into the material in a detector, causing a reaction called inverse beta decay. [15]



The positron quickly annihilates with an electron inside the detector, producing flashes of light that are then recorded. Another signal emerges when the neutron is captured by a nearby proton. By looking for the twin signals, scientists can rule out problematic background noise and confirm the neutrino interaction with high accuracy [15].

2.2.3 Supernova neutrinos

When a massive star at the end of its life collapses to a neutron star, it radiates almost all of its binding energy in the form of neutrinos, most of which have energies in the range 10-30 MeV. These neutrinos come in all flavors, and are emitted over a timescale of several tens of seconds [23].

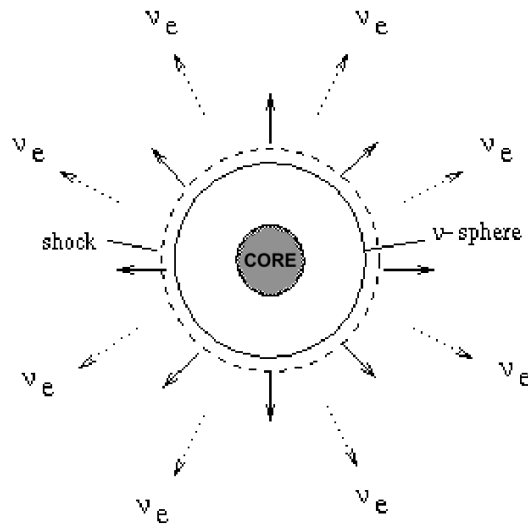


Figure 2.2: *Core collapse supernova [23].*

Core collapse supernovae (figure 2.2) arise when a massive star comes to the end of its life. All stars generate energy from nuclear fusion reactions, initially using hydrogen; when the hydrogen in the central regions runs out, stars like the Sun will eventually switch to fusing helium into carbon – which requires much higher central temperatures – before dying as a white dwarf. Stars with more than 8 times the mass of the Sun can continue this process of fusing heavier elements through successively heavier isotopes, until they form a core of iron. Once the star has formed an iron core, it is predestined to become either a core collapse supernovae, a neutron star or a stellar black hole. When the core becomes too massive to support itself against gravity, it collapses, and in these conditions of extreme heat and pressure the protons and electrons combine together to form neutrons, releasing electron-neutrinos. Conditions are so hot that even more neutrinos are made thermally, as neutrino-antineutrino pairs: in fact, even though to us it's the light from the supernova that is spectacular, 99% of the energy released by a core-collapse supernova comes in the form of neutrinos. [79]

The neutrino signal emerges from the core of a star promptly after core collapse, whereas the photon signal may take hours or days to emerge from the stellar envelope. The neutrino luminosity of a gravitational collapse-driven supernova is typically 100 times its optical luminosity [23].

Colgate and White's theory of supernova neutrino production [74] was confirmed in 1987, when neutrinos from Supernova 1987A were detected. The water-based detectors *Kamiokande II* and *IMB* detected 11 and 8 antineutrinos respectively, while the scintillator-based *Baksan detector* found 5 neutrinos, in a burst less than 13 seconds long. The neutrino signal from the supernova arrived at earth several hours before the arrival of the first electromagnetic radiation, as expected from the evident fact that the latter emerges along with the shock wave.[53]

Information from a supernova can be used to learn more about neutrinos, such as how they change over long distances and setting limits on how massive they can be. They can also be used to learn more about the life cycle of stars and the formation of neutron stars and black holes [32].

2.2.4 Atmospheric Neutrinos

Atmospheric neutrinos are typically produced around 15 kilometers above Earth's surface. They form when a cosmic ray, an energetic particle from space, crashes into Earth's atmosphere [99].

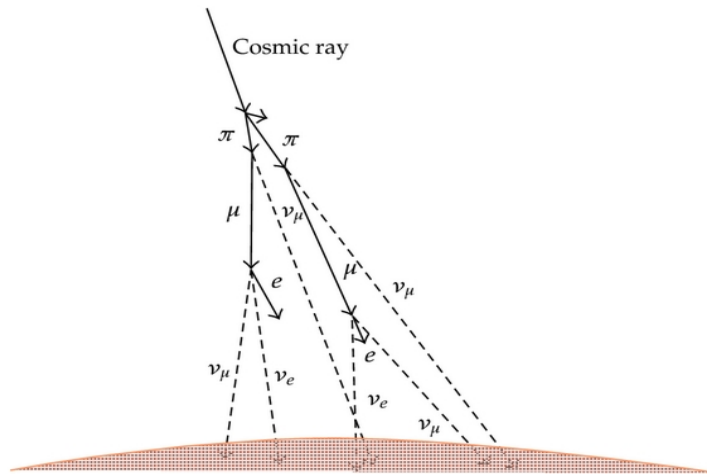


Figure 2.3: *Neutrino production from cosmic rays [99]. The primary particle, the cosmic ray hits a nuclei in the atmosphere. An example particle cascade is depicted in this figure, starting with the decay of two pions and producing atmospheric neutrinos. There are twice as many muon neutrinos produced as electron neutrinos.*

As mentioned in Chapter 1, cosmic rays are a radiation of high energy particles arriving at the Earth from the Universe. In the GeV/nucleon

energy region, these cosmic-ray particles are mostly protons, about 5% are Helium nuclei and a still smaller fraction of heavier nuclei [98].

These cosmic ray particles, after entering into the Earth’s atmosphere, interact with the nuclei in the high altitude atmosphere. Typically, in these high-energy nuclear interactions, many π mesons, and less abundantly K mesons, are produced. Since these mesons are unstable, they decay to other particles. For example, a π^+ decays to a muon (μ^+) and a ν_μ . The produced muon (μ^+) is also unstable and decays to a positron (e^+), a $\bar{\nu}_\mu$ and a ν_e . Similar decay processes occur for π^- and K mesons. In this manner, neutrinos are produced when a cosmic-ray particle enters the atmosphere [99]. Figure 2.3 shows schematically the production of neutrinos in the atmosphere. These neutrinos are called atmospheric neutrinos.

$$\pi^+ \longrightarrow \mu^+ + \nu_\mu \quad (2.3a)$$

$$\pi^- \longrightarrow \mu^- + \bar{\nu}_\mu \quad (2.3b)$$

$$\mu^+ \longrightarrow e^+ + \nu_e + \bar{\nu}_\mu \quad (2.3c)$$

$$\mu^- \longrightarrow e^- + \bar{\nu}_e + \nu_\mu \quad (2.3d)$$

If all the muons decayed before reaching the ground, we would expect to see two muon-neutrinos for every electron-neutrino (one muon-neutrino associated with the production of the muon, one of each produced when it decays). Early observations of atmospheric neutrinos were contradictory, with some experiments observing approximately the expected ratio while others saw significantly fewer muon-neutrinos than expected: the Atmospheric Neutrino Anomaly. After some years of disagreement, data from Super-Kamiokande finally convinced everyone that the deficit was real and a consequence of neutrino oscillations. The atmospheric neutrino anomaly along with the solar neutrino problem is a definitive evidence for neutrino oscillation. [80]

2.2.4.1 Neutrinos from cosmic accelerators

Recalling from chapter one, most cosmic rays may come from supernova remnants and the more energetic ones may originate in active galaxies or gamma-ray bursts - *cosmic accelerators*.

The neutrinos generated from these sources carry far more energy than any other kind of neutrino we see here on Earth—and more than we could

hope to produce in any of our experiments. The most energetic neutrinos ever witnessed were cosmic neutrinos captured by the IceCube experiment, a neutrino telescope made of a cubic kilometer of Antarctic ice. Researchers witnessed neutrinos with petaelectronvolts of energy, or one thousand trillion electronvolts. [8]

2.2.5 Relic Neutrinos

Just like the cosmic microwave background (CMB) radiation left over from the Big Bang, there is a background of low-energy neutrinos in our Universe [53]. This cosmic neutrino background (CNB or $C\nu B$) is the universe's background particle radiation composed of neutrinos. They are sometimes known as *relic neutrinos* [48]. These "Big Bang" neutrinos could provide the earliest insight into the youngest state of our universe.

2.3 Neutrino Oscillations

Contrary to predictions of the standard model, the flavor of neutrinos change as they travel. A neutrino might start out as an electron neutrino, but as it moves, it may morph into a muon neutrino or a tau neutrino, changing flavors as it goes. Looking at how neutrinos change as they travel yields valuable information about the particles [22]. Perhaps the most important thing to know about neutrinos is that they come in three types, or flavors: electron neutrino (ν_e), muon neutrino (ν_μ), tau neutrino (ν_τ).



Each flavor of neutrino is considered a fundamental particle and they are associated with three similarly named fundamental particles, the electron, muon and tau. When a neutrino interaction happens, this partner lepton often shows up, which helps in identifying the neutrino flavor that generated this lepton.

Neutrinos are produced in astronomical sites with some initial composition of the above mentioned flavors. For instance:

1. in the Sun they are electron neutrinos, since the matter is proton-rich and certain nuclear species transform according to $p \rightarrow n + e^+ + \nu_e$

2. in supernovae, all types of neutrinos and antineutrinos are produced, due to all types of reactions, including the pair radiation $N + N \rightarrow N + N + \nu_l + \bar{\nu}_l$ with $l = e, \mu, \tau$

3. in cosmic ray collisions, around their sites of production, they are mostly electron and muon neutrinos and anti-neutrinos, since they are due to light meson decays such as $\pi^+ \rightarrow \mu^+ + \nu_\mu$ followed by $\mu^+ \rightarrow e^+ + \nu_e + \bar{\nu}_\mu$

However, for neutrinos to change flavor, neutrinos had to possess mass. Once produced, therefore, the neutrinos and antineutrinos with given flavor $l = e, \mu, \tau$ cannot propagate unperturbed, since they are not states with definite mass. They are rather superpositions of states with given mass. [111]

One of the most sensitive methods to observe small neutrino masses is to study neutrino flavor oscillations. If neutrinos have finite masses, each flavor eigenstate (e.g. ν_μ) can be expressed by a combination of mass eigenstates (ν_1, ν_2, ν_3). The relation between the mass eigenstates (ν_1, ν_2, ν_3) and the flavor eigenstates (ν_μ, ν_e, ν_τ) can be expressed by

$$\begin{pmatrix} \nu_e \\ \nu_\mu \\ \nu_\tau \end{pmatrix} = U \begin{pmatrix} \nu_1 \\ \nu_2 \\ \nu_3 \end{pmatrix} \quad (2.4)$$

where U is the mixing matrix. The mixing matrix U (Pontecorvo–Maki–Nakagawa–Sakata OR **PMNS Matrix**) is expressed by

$$U = \begin{pmatrix} c_{12}c_{13} & s_{12}c_{13} & s_{13}e^{-i\delta} \\ -s_{12}c_{23} - c_{12}s_{23}s_{13}e^{i\delta} & c_{12}c_{23} - s_{12}s_{23}s_{13}e^{i\delta} & s_{23}c_{13} \\ s_{12}s_{23} - c_{12}c_{23}s_{13}e^{i\delta} & c_{12}s_{23} - s_{12}c_{23}s_{13}e^{i\delta} & c_{23}c_{13} \end{pmatrix} \quad (2.5)$$

where c_{ij} and s_{ij} represent $\cos \theta_{ij}$ and $\sin \theta_{ij}$ respectively [99].

As already mentioned, high energy neutrinos are produced in astrophysical sources mainly through the decay of charged pions, in $p\gamma$, pp , pn interactions. Therefore, neutrino fluxes of different flavors are expected to be at the source in the ratio:

$$\nu_e : \nu_\mu : \nu_\tau = 1 : 2 : 0 \quad (2.6)$$

Neutrino oscillations will induce flavor changes while neutrinos propagate through the Universe. One has to consider mass eigenstates $\nu_m = \nu_1, \nu_2, \nu_3$ in the propagation, instead of weak flavor eigenstates $\nu_l = \nu_e, \nu_\mu, \nu_\tau$. The weak flavor eigenstates ν_l are linear combinations of the mass eigenstates ν_m through the elements of the mixing matrix U as seen in eqn. 2.4 is [73] :

$$\nu_l = \sum_{m=1}^3 U_{lm} \nu_m \quad (2.7)$$

The oscillation probability in the simple case of only two flavors, for instance (ν_μ, ν_τ) and one mixing angle θ_{23} , is [73]:

$$\nu_\mu = \nu_2 \cos \theta_{23} + \nu_3 \sin \theta_{23} \quad (2.8a)$$

$$\nu_\tau = -\nu_2 \sin \theta_{23} + \nu_3 \cos \theta_{23} \quad (2.8b)$$

$$(2.8c)$$

The probability for a neutrino produced in a flavor state ν_μ to be observed in a flavor state ν_τ after traveling a distance L through the vacuum is

$$P(\nu_\mu \rightarrow \nu_\tau) = \sin^2 2\theta_{23} \sin^2\left(\frac{1.27 \Delta m_{23}^2 (eV^2) L (km)}{E_\nu (GeV)}\right) \quad (2.9)$$

where E_ν is the neutrino energy, θ_{23} is the mixing angle between the flavor eigenstates and the mass eigenstates, and Δm_{23}^2 is the mass-squared difference of the neutrino mass eigenstates ($\equiv |m_2^2 - m_3^2|$) [99].

The above 2-flavor oscillation formula has to be generalized to three-flavor oscillations. In the three-flavor oscillation framework, neutrino oscillations are parametrized by three mixing angles ($\theta_{12}, \theta_{23},$ and θ_{13}), three mass squared differences ($\Delta m_{12}^2, \Delta m_{23}^2,$ and Δm_{13}^2 ; among the three Δm^2 's, only two are independent), and one CP phase (δ). θ_{23} and Δm_{23}^2 are most relevant to present atmospheric neutrino experiments. θ_{12} and Δm_{12}^2 are most relevant to solar and long baseline reactor neutrino experiments. θ_{13} was most recently measured by accelerator-based long baseline and reactor neutrino oscillation experiments. [99]

According to these neutrino oscillation parameters, the ratio of fluxes of neutrinos from astrophysical origin (i.e. very large baseline L) in eqn. 2.6

changes to a flux ratio at Earth as [73]

$$\nu_e : \nu_\mu : \nu_\tau = 1 : 1 : 1 \quad (2.10)$$

2.4 Neutrino Interactions

While the previous sections were dedicated to the sources, production mechanisms and types of cosmic neutrinos, this section deals with the interactions of neutrinos at (or rather inside) the Earth and the detection of these interactions.

Since neutrinos are very light, electrically neutral leptons, they interact only through the weak force (and as all matter, through gravitation).

When neutrinos encounter a matter, target reactions takes place with both electrons and nucleons. However, for neutrinos with energies in the range $1\text{PeV} \leq E_\nu \leq 100\text{PeV}$ the cross-section for *neutrino + electron* reactions is very small compared with the cross-section for *neutrino + nucleon* reactions. Hence the total neutrino interaction cross sections are dominated to a very large extent by these deep inelastic scattering reactions of the neutrino on the nucleon.

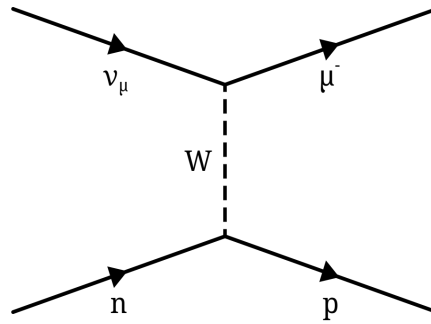


Figure 2.4: An example Feynman diagram of charge current ν_μ interaction [113].

Neutrinos interact via weak interactions.

- "Charged-current interaction" (CC) mediated by particles that carry an electric charge (the W^+ or W^- bosons), and is responsible for the beta decay phenomenon [57]. Here the neutrino interacts with a nucleon and converts into the equivalent charged lepton where finally detectors detect this charged lepton (by detecting the cherenkov radiation emitted by this charged lepton in the medium)

- "Neutral-current interaction" (NC) mediated by a neutral particle, the Z boson [57]. This is where the neutrino remains a neutrino, but transfers energy and momentum to whatever it interacted with – this energy transfer is detected, either because the target recoils or because it breaks up.

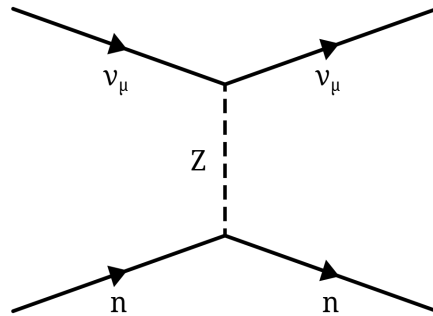


Figure 2.5: An example Feynman diagram of neutral current ν_μ interaction [113].

In principle, charged-current interactions are easier to work with, because electrons and muons have characteristic signatures in particle detectors and are thus fairly easy to identify. They also have the advantage that they “flavour-tag” the neutrino: if an electron is produced, it came from an electron-neutrino. However, there must be enough available energy to allow the mass of the lepton to be created from $E = mc^2$ – this means that for very low-energy neutrinos (e.g. solar and reactor neutrinos) charged-current interactions are only possible for electron-neutrinos. [76]

Schematic views of a ν_e , ν_μ and ν_τ CC events and of a NC event are shown in Fig. 2.6. Neutrino and anti-neutrino reactions are not distinguishable; thus, no separation between particles and anti-particles can be made.

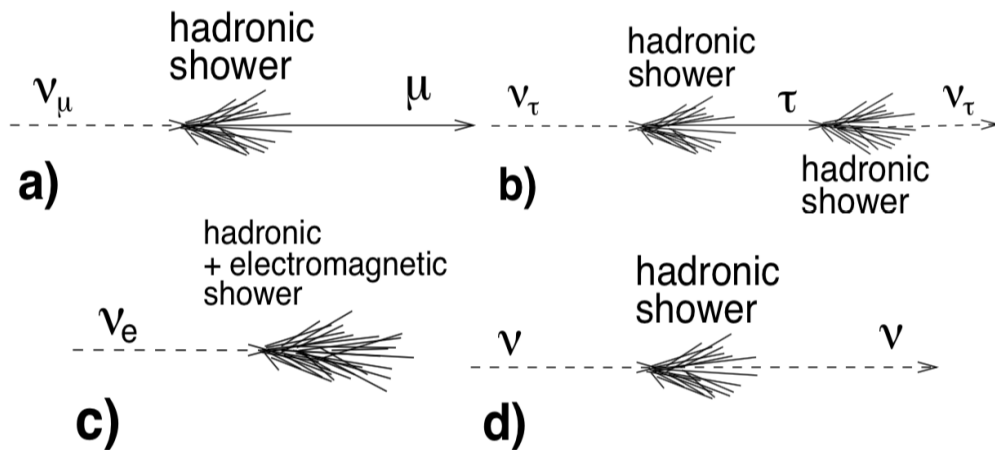


Figure 2.6: *Some event signature topologies for different neutrino flavors and interactions in ANTARES. (a) CC ν_μ interaction, (b) CC ν_τ interaction, tracing the double bang signature, (c) CC ν_e interaction and (d) a NC interaction producing a hadronic shower [90].*

2.5 Neutrino Detection

Neutrino interaction cross sections are very small. Therefore, huge target masses are needed for their detection, and the detection can only be indirect, i.e. through the detection of the interaction products. Several distinctive detector technologies have been used in neutrino experiments throughout the years, subject to the needs of the area of study. Suitable topographies of a neutrino experiment must typically include many of the following [76]:

- **Low energy threshold**, so that low-energy neutrinos can be detected and studied (especially for *solar neutrinos*)
- **Good angular resolution**, so that the direction of the detected particle can be accurately reconstructed (especially for *astrophysical neutrinos*)
- **Good particle identification**, so that electrons and muons can be well separated (essential for *oscillation experiments*)
- **Good energy measurement**, so that the energy of the neutrino can be reconstructed (useful for oscillation measurements and astrophysics)

- **Good time resolution**, so that the time evolution of transient signals can be studied (essential for *supernova neutrinos*, and important for other astrophysical sources)
- **Charge identification**, so that leptons and antileptons can be separated (will be essential for neutrino factory experiments)

It is not possible to have all of these things in one experiment – for example, experiments with very low energy threshold tend not to have good angular or energy resolution. Neutrino physicists select the most appropriate technology depending on the aims of a particular experiment [76]. In the following sections, we will discuss different neutrino experiments.

2.5.1 KM3NET

At the bottom of the Mediterranean Sea, an enormous detector is being constructed that will study cosmic neutrinos that have passed straight through the Earth. Numerous scientific and technical challenges need to be overcome to make this possible. The principle of the KM3NET (acronym for Cubic Kilometer Neutrino Telescope) detector is based on the very accurate measurement of the arrival time of the cherenkov radiation wavefront generated by the charged lepton [21] [2].

As the chances of neutrino interactions are so small, the measurements would be performed in an enormous volume of water to be able to detect enough neutrino interactions. The KM3NeT detector will have a total volume of 3 km^3 , and will thus be able to detect several cosmic neutrinos per year. The detector (see Figure 2.7) is made up of detection lines, each of which has 18 digital optical modules (DOMs). These are thick glass spheres, which each contain 31 photomultiplier tubes (PMTs): highly sensitive sensors that detect the Cherenkov radiation. The vertical distance between the spheres is 40m: a detection line is 760m long. The distance between the lines is about 100m. The detector is located at a depth of 3.5 km under the surface on the seabed. With a height of 760m the detector still has 2.7km of water above it. No sunlight penetrates to that depth. However, there is some light from radioactive decay (^{40}K is a radioactive component of sea salt) and from organisms that produce light, a phenomenon called *bioluminescence*, which will be discussed in detail later. But these light sources do not move through the detector with con-

siderable speed, making them easily distinguishable from a neutrino signal. Another source of background are the Atmospheric muons which will also be briefly introduced in chapter 4. [21] [2]

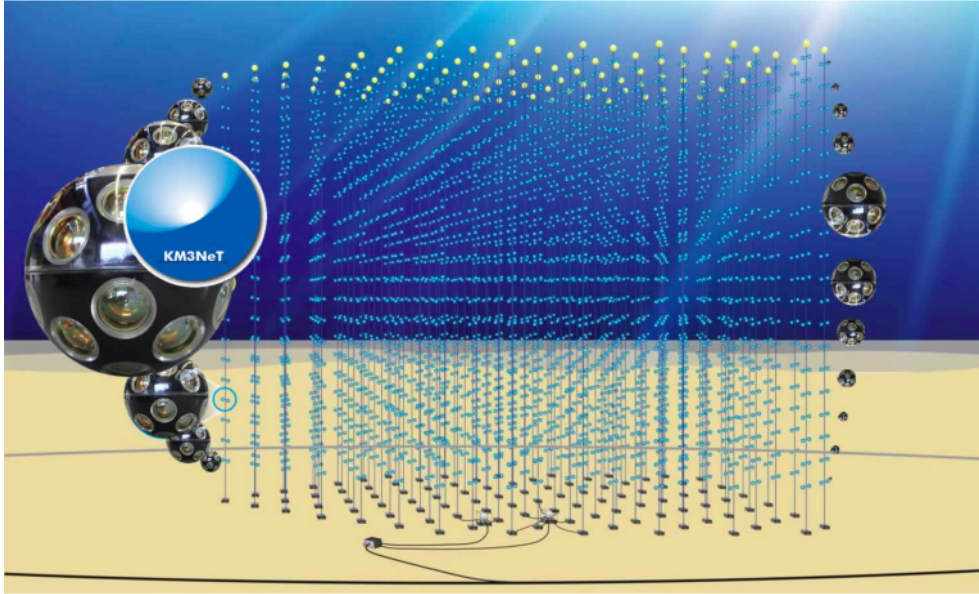


Figure 2.7: *Impression of the KM3NET detector [21]*

KM3NeT is not the first neutrino telescope of this type. The ANTARES detector, which is located near Toulon in France at a depth of 2.5 km, has been detecting neutrinos since 2007.

2.5.2 ICECUBE

The South Pole is a home to the world's largest neutrino detector - IceCube.

IceCube is an international collaboration which has constructed and is operating the world's largest neutrino telescope. Its main mission is the discovery and exploration of Galactic and extragalactic sources of high-energy neutrino emission. However, the detector is also well suited for the search for dark matter (WIMPs) and the measurement of cosmic rays, neutrino oscillations and several other topical questions in particle and astroparticle physics. [101]

While photographs of IceCube often show a building sitting on the snowy surface, the real work is done below. The multipurpose experiment includes a surface array, IceTop, an array of stations that sit above

the strings. IceTop serves as a calibration detector for IceCube, as well as detecting air showers from primary cosmic rays, and their flux and composition. [110]

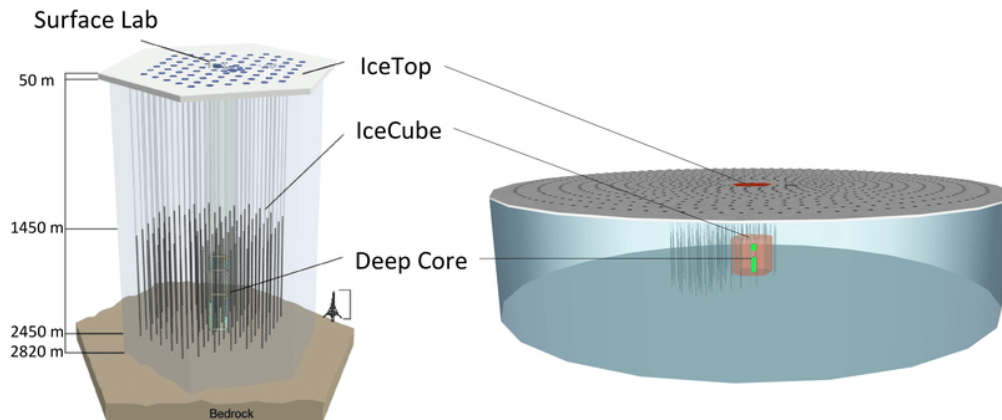


Figure 2.8: *Sketch of IceCube detector [58].*

The dense inner subdetector, DeepCore, is the powerhouse of the IceCube experiment. Each of the IceTop stations are made up of strings attached to digital optical modules (DOMs) that are deployed on a hexagonal grid spaced 125 meters apart. Several hundred scientists and engineers have constructed and deployed over 5,000 OF THESE individual photosensors in 86 separate 1.5-mile-deep holes melted in the polar ice cap with a custom-designed hot-water drill. Over the course of seven summer seasons these sensors were installed. The IceCube array was fully installed in early 2011 and has been taking data continuously ever since [81]. This array of ice-bound detectors can sense with great precision when a neutrino flies through and interacts with a few Earthly particles that generate dim patterns of bluish Cherenkov light, given off when charged particles move through a medium like ice at close to light speed. Figure 2.8 shows a sketch of the Icecube detector. Deep within the ice, IceCube is able to hunt for neutrinos that come from the sun, from within the Milky Way, and from outside the galaxy.

IceCube successfully detected the so called "IceCube-170922A neutrino" – and traced it back to a small patch of sky in the constellation Orion and pinpointed the cosmic source: a flaring black hole the size of a billion suns, 3.7 billion light years from Earth, known as blazar TXS 0506+056

[81], [75].

In addition, design work is now underway on a next generation neutrino observatory, IceCube-Gen2, with the goal to instrument a volume of 10km^3 , and deliver a substantial increase in sensitivity to astrophysical neutrinos of all flavors. IceCube-Gen2 would build upon the existing IceCube detector infrastructure, and would take advantage of the very long absorption lengths found in the glacial ice near the IceCube detector to add additional instrumentation with significantly larger string separation distances. Building this larger instrument would be achieved with a comparable number of strings used in the existing IceCube detector, and would target neutrino energies above ~ 50 TeV with high efficiency. [58]

2.5.3 SUPER-KAMIOKANDE

Super-Kamiokande is a large water Cherenkov detector, the construction of which started in 1991 and the observations began on April 1st, 1996. The Super-Kamiokande is operated by an international collaboration of about 150 people and about 40 institutes [25].

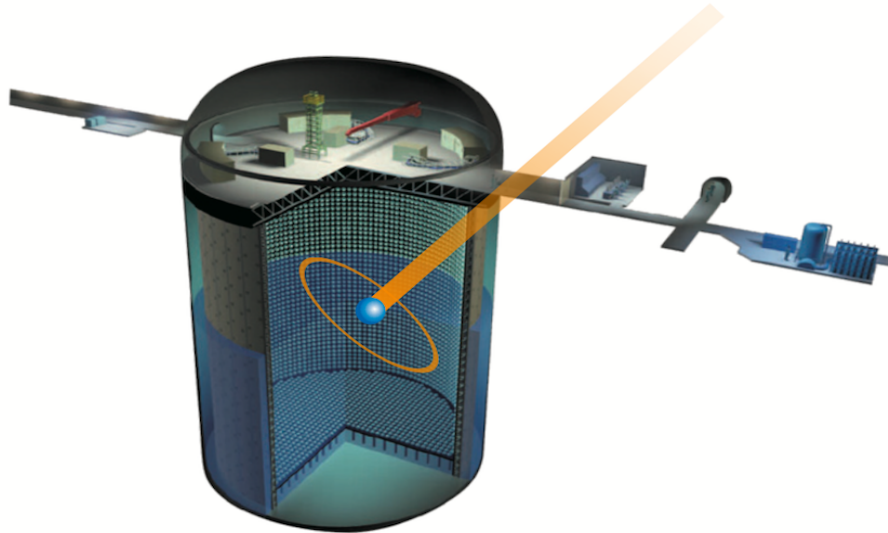


Figure 2.9: *The Super-Kamiokande detector, in cutaway, showing the inner and outer detector, partially filled with water [97].*

The Super-Kamiokande detector consists of a stainless-steel tank, 39.3m diameter and 41.4m tall, filled with 50,000 tons of ultra pure water (figure 2.9). About 13,000 photo-multipliers are installed on the tank wall. The

detector is located at 1,000 meter underground in the Kamioka-mine, Hida-city, Gifu, Japan.[25]

The PMT support structure divides the tank into two distinct, optically isolated volumes, the inner detector (ID) and the outer detector (OD). The inwarded PMTs are installed to the ID wall and the outwarded PMTs to the OD wall. The inward-facing 11,129 photo-multiplier-tubes (PMTs) are instrumented in the inner tank. The Cherenkov light emitted by charged particles running in water is detected by these sensors. After 2002, in order to avoid chain reactions of implosions even if a single PMT implosion happen, all of inner PMTs are covered with acrylic and fiberglass shields. The main purpose of the outer detector is to distinguish the neutrino events from the cosmic ray muon events. The cosmic ray muons are background sources of the neutrino observation. [10]

Because the neutrinos are electrically neutral, the Cherenkov light is emitted when the neutrinos scatter with the water. On the other hand, because the cosmic ray muon have an electric charge, the Cherenkov light is immediately emitted when the cosmic ray muon enters the detector. Therefore, in case of cosmic ray muons the OD PMTs almost have hits, while in case of neutrinos, the OD PMTs have few hits. This difference enables to roughly distinguish between neutrinos and cosmic ray muon events. [12]

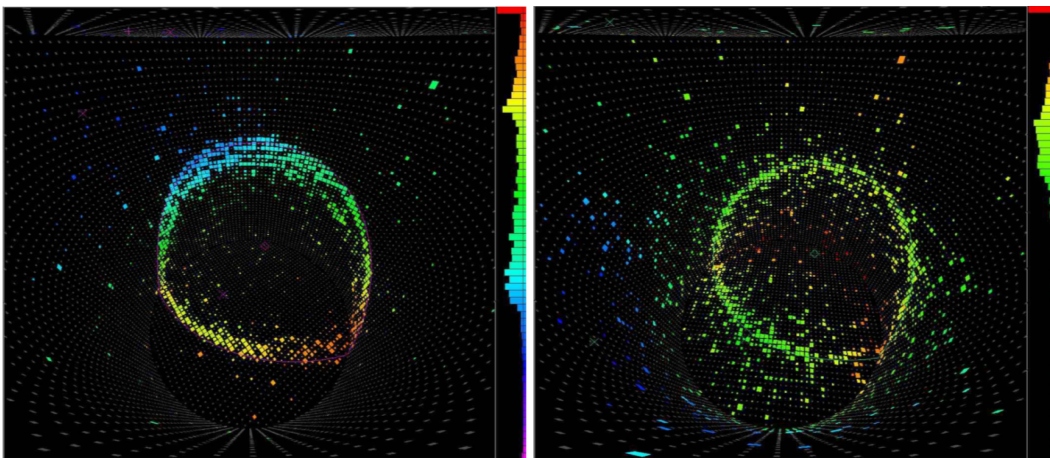


Figure 2.10: *Two simulated events displayed for the Super-Kamiokande detector. Left: a muon event. Notice the cleaner outer ring of the Cherenkov cone. Right: an electron event. Notice that the ring is much more ragged due to the many particles of the electromagnetic shower and multiple scattering of the shower particles [69].*

Shown in Figure 2.10 is the signal in the photomultipliers of the detectors. The color code indicates arrival time. When a charged particle flies through the detector, the cherenkov cone can be seen by the PMTs as depicted in the figure. One of the purposes of the Super-Kamiokande experiment is to reveal the neutrino properties through the observation of solar neutrinos, atmospheric neutrinos and man-made neutrinos. In 1998, Super Kamiokande measured neutrino oscillation from the observation of atmospheric neutrinos. Neutrino oscillation describes a change of neutrino type in their flight. In 2001, solar neutrino oscillation was measured when observing solar neutrinos. In 2011, the third neutrino oscillation mode was detected by man-made neutrino observation. [10], [12]

The picture in Fig. 2.10 is the event display of a muon neutrino detected by the Super-Kamiokande. The colored points indicate the quantity of the detected light by each PMT. The Cherenkov ring emitted by a muon is displayed [69].

2.5.4 BAIKAL/GVD

The Baikal Deep Underwater Neutrino Telescope (BDUNT) is a neutrino detector conducting research below the surface of Lake Baikal (Russia) since 2003. At 1.1km beneath the surface of the world's deepest lake and pointing towards the centre of the Earth, it is one of the most unusual telescopes on the planet [41]. The first detector was started in 1990 and completed in 1998. It was upgraded in 2005 and again starting in 2015 to build the Baikal Gigaton Volume Detector (Baikal-GVD.) BDUNT has studied neutrinos coming through the Earth with results on atmospheric muon flux. BDUNT picks up a lot of atmospheric neutrinos created by cosmic rays interacting with the atmosphere — as opposed to cosmic neutrinos which can give clues to cosmic events and are therefore of greater interest to physicists [47].

The original NT-200 design was deployed in stages 3.6 km from shore at a depth of 1.1 km. The first part, NT-36 with 36 optical modules (OMs) at 3 short strings, was put into operation and took data up to March 1995. NT-72 ran 1995–1996 then was replaced by the four-string NT-96 array. Over its 700 days of operation, 320,000,000 muon events were collected with NT-36, NT-72, and NT-96. Beginning April 1997, NT-144, a six-string array took data. The full NT-200 array with 192 modules was

completed April 1998. In 2004-2005 it was updated to NT-200+ with three additional strings around NT-200 at distance of 100 meters, each with 12 modules. [47]

The successful, more than 10 year long operation of the the NT200 Baikal neutrino telescope proved the feasibility and efficiency of neutrino detection in natural media, which made it possible to pass to development and implementation of projects of new generation setups with a sensitive volume of ~ 1 km³. The first stage of 3 strings was switched on in April 2013. During 2015 the GVD demonstration cluster with 192 optical modules was successfully operated. In 2016 this array was upgraded to the baseline configuration with 288 OMs on eight vertical strings. It is expected to be completed around 2020. [66]



Strings for Absorption Length in Water (STRAW)

ONC (Ocean Networks Canada), an initiative of the University of Victoria, in British Columbia, operates undersea sensor networks around Canada and they support interdisciplinary science through a wide variety of instruments connected by undersea cables that provide ample power and gigabits per second of communication capability. Of particular note, the ONC deep-sea infrastructure at Cascadia Basin dark site (N47°46' W127°46') , at a depth of ~ 2600 m b.s.l., provides a number of the ideal prerequisites for a possible large scale neutrino telescope. To this end, since late 2017 a pathfinder mission emerged named “STRings for Absorption length in Water” (STRAW) with the aim to build and deploy photosensors and calibration instrumentation. In June 2018 STRAW was deployed at the Cascadia Basin site and has been collecting data since then. [70]

The target of the STRAW project is the investigation of the Cascadia Basin for its feasibility as a possible new large scale neutrino telescope site by characterizing the optical properties of its deep waters. Ultimately this will enable the evaluation of the site and its compatibility to host a potential large-volume neutrino telescope. In what follows, I will refer to the previous theses related to STRAW [86] [92] along with [70].

3.1 STRAW Concept and Design

STRAW was built and deployed with a vision of being a new large-scale neutrino facility in the Pacific. The main aims of STRAW are

1. To principally deduce the attenuation properties of the sea water thus allowing the measurement of the absorption and scattering length of

the water at Cascadia Basin in the wavelength range between 350 nm and 600 nm, and

2. The characterization of the overall ambient background light produced by the bioluminescence of deep-sea living organisms and the ^{40}K dissolved in the sea water [70].

Following the norm of the existing neutrino telescopes, the design of STRAW includes PMT light sensors, LED calibration light sources, and specific choices about the readout electronics and deployment strategy. The STRAW detector is a two-string geometry made of two vertical mooring lines instrumented with light emitter and light sensor modules mounted at different heights above the sea floor. The light emitter module is based on the design of the Precision Optical Calibration Module (POCAM), which provides an isotropic and short-pulsed flash of light. The light sensor module named the STRAW Digital Optical Module (sDOM) uses two 3" PMTs encapsulated in a titanium cylinder similar to the one of the POCAM. The entire PMTs' readout and data acquisition system is also included in the module [70].

3.1.1 Optical properties of sea water

Seawater is an nearly homogenous dielectric material, thus interference does not significantly affect light propagation. Therefore the optics can be seen as the propagation of whole wave packages. Keeping in mind one of the primary goals of STRAW, the processes of absorption and scattering have to be characterised. Both effects depend on the distance the photon has travelled and are described by an exponential law. [115]

The absorption length $L(\lambda)$ and the scattering length $S(\lambda)$ are defined as the distance, when e^{-1} of the initial photons are absorbed or scattered or in general *attenuated*. The measurement of the attenuation length L_T in water is realized by emitting a flash of photons of known intensity I_0 and wavelength λ from one of the POCAMs and detecting it at a known distance r in one of the sDOMs with effective collection area A_{det} [70], and measuring an intensity $I(r)$ [115]

$$I(r) = \frac{I_0}{4\pi r^2} \exp(-r\mu) A_{det} \quad (3.1)$$

where μ is the attenuation coefficient and is simply the inverse of the attenuation length L_T .

$$\implies I(r) = \frac{I_0}{4\pi r^2} \exp\left(\frac{-r}{L_T}\right) A_{det} \quad (3.2)$$

From the look of the absorption spectrum in pure water [72] as well as in sea water [115], it is known that the absorption length is highest for the wavelength band around $460nm$ and decreases quickly in the UV as well as towards the red region of the spectrum. Fortunately, this is also the most sensitive wavelength band for the detection of Cherenkov light, especially when using PMTs. Expected maximum values for the absorption length are around $50m$; therefore a geometry has been chosen that covers distances from $20m$ to $90m$ [70]. The geometry also incorporates a fair amount of symmetry to allow for a study of systematic uncertainties on a module to module basis. The STRAW detector aims to probe the absorption and scattering of the deep Pacific water near the Cascadia Basin.

3.2 The Modules

As mentioned in the previous section the STRAW detector array hosts two long mooring lines spaced nearly 40 m apart, with a total of three light emitters and five light sensors. These modules are spaced at about 20 m from each other. With this setup the distances between the modules extend over few attenuation lengths in any expectable case.

Figure 3.1 shows a detailed mechanical sketch of the STRAW mooring lines with exact geometries of all the modules involved. Each string is attached to a buoy at the top and an anchor at the bottom. The strings have a length of 140 m in total with instruments at the heights of 30 m, 50 m, 70 m and 110 m. The strings consist of two steel wire ropes each, which are kept apart by spacers. The strings are referred to as string Blue and string Yellow. The use of double strings prevents the rotation of the modules around the strings, making sure that the modules of the two strings face each other. There are four modules on each string which are connected to a mini junction box at the bottom, developed by ONC. [86]

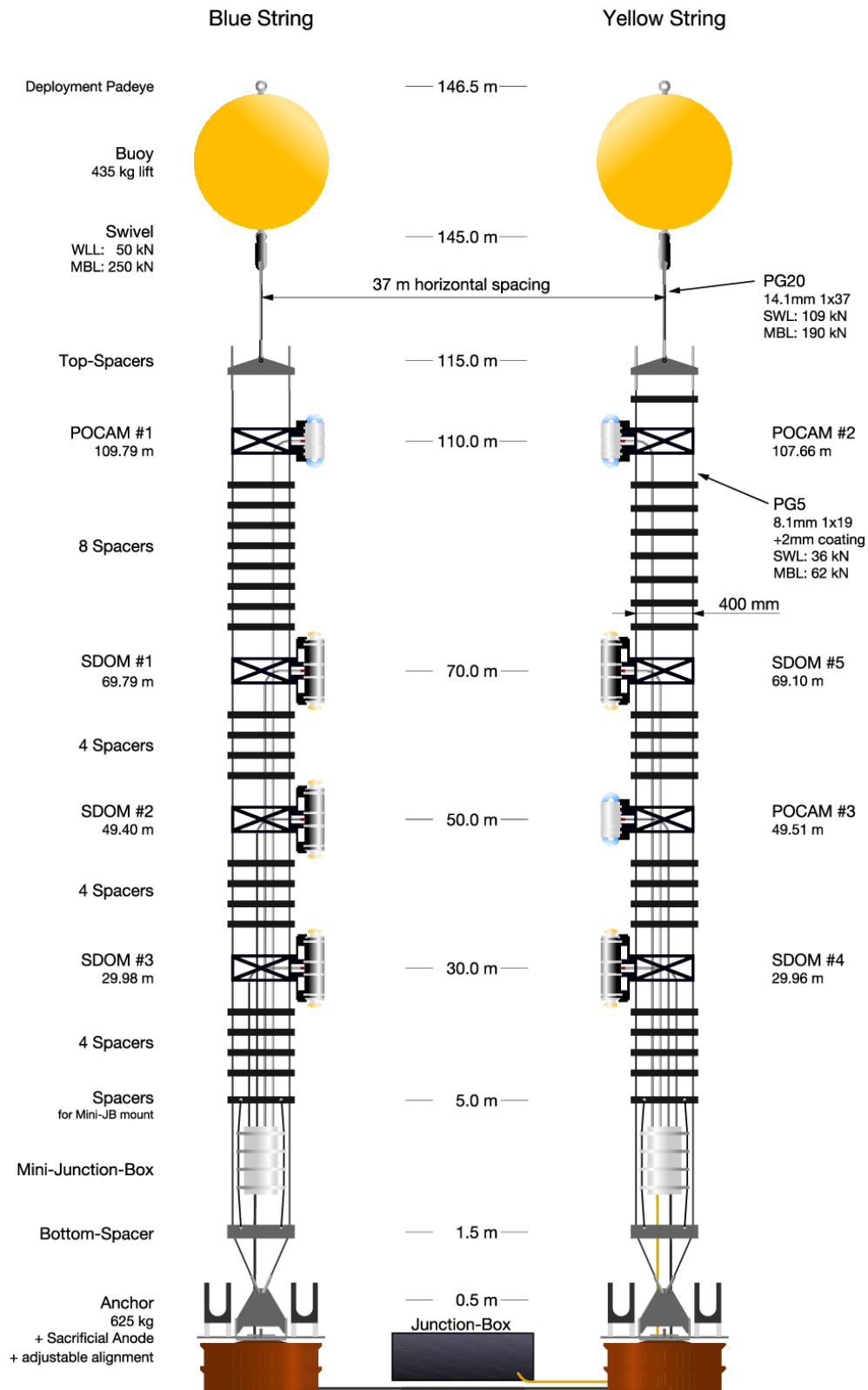


Figure 3.1: Detailed Sketch of the STRAW strings (courtesy Kilian Holzapfel) with precise specifications and geometry of all the modules [70].

3.3 POCAM

The Precision Optical Calibration Module (POCAM) was initially designed to act as a calibration device for IceCube Gen2 [96] to improve the understanding of the optical properties of ice [70]. For the STRAW project, the POCAM was iterated and a second generation was developed. This new version uses LED flashers of four different wavelengths in the 365 - 600 nm range. This LED flasher is based on a modified version of the Kapustinsky LED pulsing circuit [92] which provides nanosecond light pulses. With the implementation of in-situ self-calibration using integrated photosensors, the POCAM acts as an isotropic light source emitting light flashes with known intensity. As a result the POCAMs are used to emit intense (10^9 photons), adjustable (via the supply voltage), isotropic, nanosecond light flashes that are observed by the surrounding sDOM units. [92]



Figure 3.2: *Simulation of a POCAM assembly giving aside view of all its components [93].*

One major challenge faced by the author of [92] when using LEDs was to achieve a high level of intensity and isotropy with these flashes while keeping the nanosecond timing - the former being necessary to illuminate

the large detector volume homogeneously, and the latter allowing one to differentiate between direct and scattered light. The adjustable light intensity is required in order to be able to detect single photons over a large range of distances and for different possible attenuation lengths.

A rendering of the final structure of the POCAM can be seen in Figure 3.2. As it can be noticed, the external part is composed by two glass hemispheres that are connected to a cylindrical housing. In order to achieve a high-pressure resistance and to withstand temperature changes, all while avoiding corrosion, the cylindrical part of the housing is made from titanium. Moreover for the glass hemispheres, an optically enhanced borosilicate glass (N-BK7) has been used, which provides a transmissivity of $>95\%$ in the range between 350 nm and 600 nm [86]. Within each hemisphere, on top of the LED array are the semi-transparent teflon (PTFE) integrating spheres. These PTFE sphere in each hemisphere aim to isotropically diffuse the anisotropic emission from the LEDs so as to homogeneously illuminate the water. A detailed study of the isotropy achieved can be found in [92]. Lastly, electrical supply and control are enabled by a connector located in the center of the cylinder.

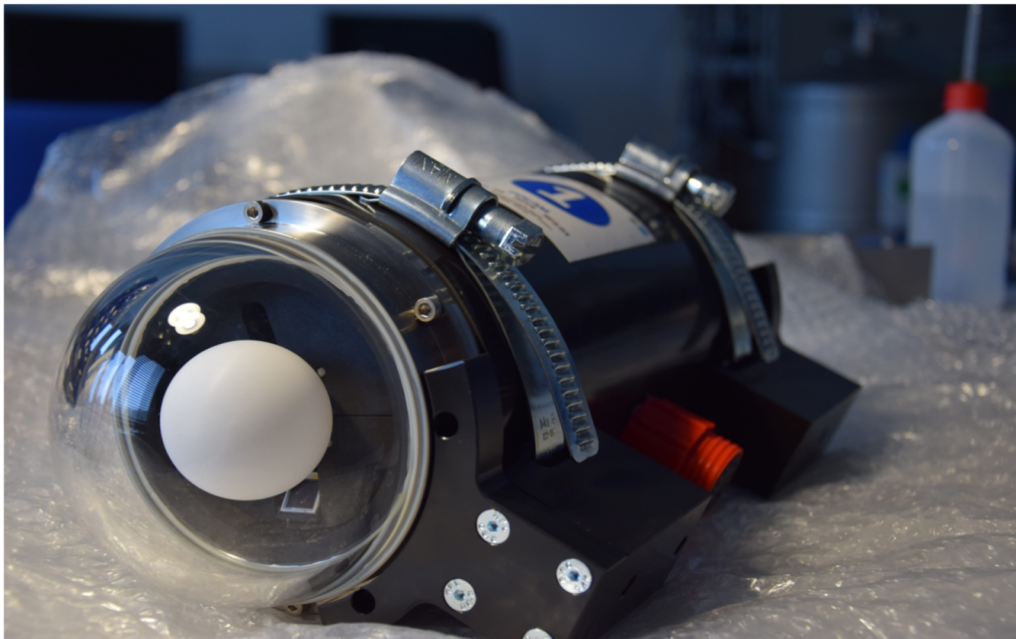


Figure 3.3: *Final POCAM module prior to shipment to Canada. Visible is the housing, one integrating sphere, the mounting structures and the instrument connector including its safety clamp [70].*

The first prototype of the POCAM has been successfully installed and tested within the GVD neutrino telescope in spring of 2017. It was deployed within the detector 1000 m below the surface of Lake Baikal and several calibration runs were performed. Preliminary analyses confirm the expected attenuation length of the Baikal water which is also subject of ongoing research. [93]

A detailed study of all the components involved in the STRAW POCAM - from the housing to the integrating spheres to the LED flasher board and even the electronic involved- can be found in [92].

3.4 SDOM

The STRAW light sensor module is called the STRAW Digital Optical Module or the *sDOM*. It is designed to capture the flashes of light that the POCAM emits and thereby provide an estimate of the light attenuation length at the Cascadia Basin.

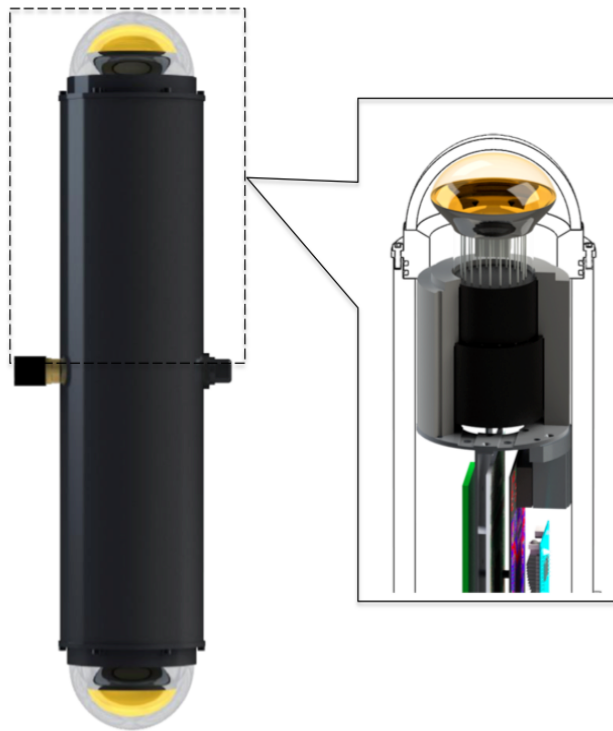


Figure 3.4: (left) *sDOM* housing design by F. Henningsen [92], (right) The interior design of the *sDOM* showing the upper half with the PMT and its electronics mounted under the aluminium plate [70].

Unlike the POCAM, the sDOM was very specifically designed for the STRAW project. Just like the POCAM makes use of two integrating spheres at the two ends of the cylindrical titanium housing, the sDOM makes use of two hemispherical photomultipliers to allow nearly isotropic light detection. This STRAW sensor can also monitor the background light produced by the ambient bioluminescence and radioactivity (mainly ^{40}K). All elements of the readout, data acquisition system and file storage are included inside the housing of the sDOM, making it an independent instrument that can communicate via Ethernet and RS485. [86]



Figure 3.5: *Hamamatsu PMT R12199* [26].

3.4.1 Housing

The housing of sDOMs is based on the concept used for the POCAM, since the latter had already been successfully tested in deep waters. The housing consists of the same type of titanium cylinder and two hemispheres on each end as the POCAM, however, significantly longer, with an overall length of 60cm, allowing enough room for two PMTs with their bases, readout electronics, communication, internal mounting and heat dissipation. This design can withstand an outside pressure of up to 600 bar, far exceeding the conditions present at Cascadia Basin. [70]

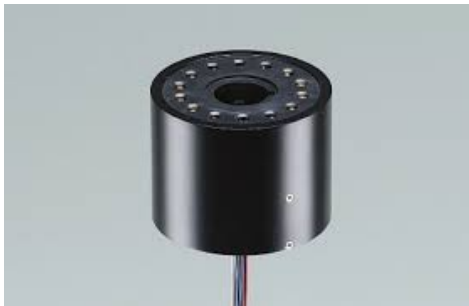


Figure 3.6: *PMT base C12842-02 MOD* [117]

Additionally, the sDOM housing was subjected to a number of environmental and stress tests to ensure that the module would withstand deployment and operation at a depth of 2.6 km b.s.l.. For power and data connections, a penetrator is mounted in the sDOM along with a vacuum plug for degassing. These are both identical as the one used for the POCAM.

Figure 3.4 shows a design of the sDOM housing which resembles the

Table 3.1: PMT R12199 Specifications [117],[94]

Parameter	Description/Value	Unit
Spectral Response	300 to 650	nm
Wavelength of Maximum Response	420	nm
Window Material	Borosilicate glass	—
Photocathode Material	Bialkali	—
Photocathode Minimum Effective Area	72	mm
Dynode Structure	Circular and linear-focused	—
Dynode Number of Stages	10	—
Base	JEDEC No. B14-38	—
Operating Ambient Temperature	30 to +50	°C

housing of the POCAM. Moreover, this sDOM housing was subjected to a number of environmental tests to analyse its suitability in the deep sea environment.

3.4.2 Photomultiplier tubes

As has been mentioned earlier, and similar to any other detector, sDOMs also has a functional unit - the PMT (Photomultiplier tubes). Each sDOM is equipped with two 3" R12199 PMTs (3.5) from Hamamatsu Photonics.

These are concave-convex windowed PMTs, instrumented with a Bialkali photocathode and Borosilicate glass window, giving a spectral response in the 300 - 600 nm range, having an average 25% peak quantum efficiency at 420 nm. The PMT is powered by an active (Cockroft-Walton) base, C12842-02 MOD (3.6), customized for STRAW by Hamamatsu. This high voltage power supply ensures high output linearity of photomultiplier tubes while maintaining low power consumption. Figure 3.7 shows a dimensional outline of PMT R12199 along with its base and table 3.1 gives its the specifications. [117], [94]

The sDOM is equipped with a DC/DC converter that transforms the 48 V system supply voltage to 5 V for the PMT. The socket uses the 5 V power supply and an analog control input, which is 1/1000 of the PMT HV. The control voltage for the PMT (0 V to 1.5 V) is produced using a pulse width modulator (PWM). The PMTs are placed inside the two glass hemispheres. In order to avoid reflections, refractive losses and a limited field of view, the PMTs are glued to the glass hemispheres ($n_{\text{Glas}} = 1.53$) using optical gel (Wacker SilGel 612, $n_{\text{Gel}} = 1.4$ at 589 nm) with good transmission between 350 nm and 600 nm. [70]

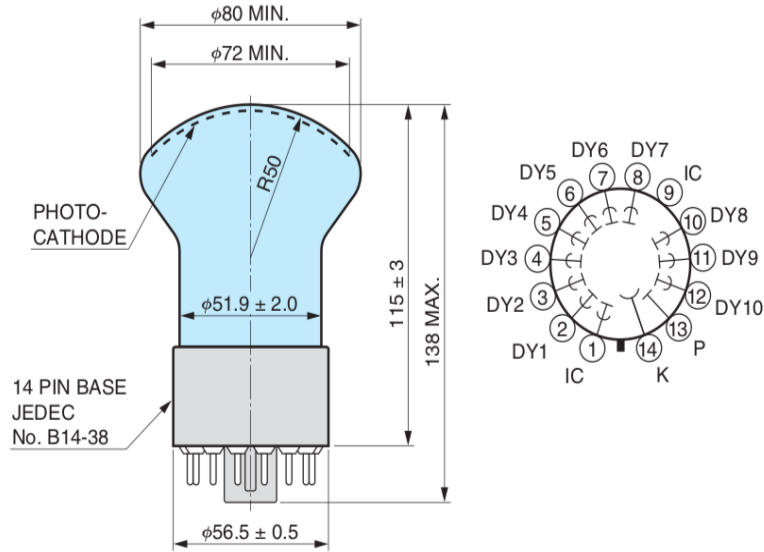


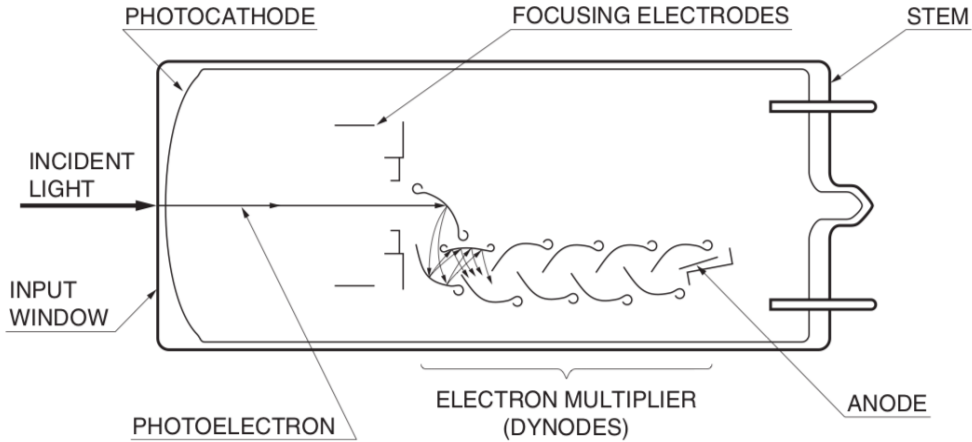
Figure 3.7: Dimensional outline and basing diagram [117].

3.4.3 Detection principle of PMTs

This section will briefly give an overview of the prime features of a photomultiplier tube construction and basic operating characteristics.

The PMT is a photosensitive device consisting of an input window, a photocathode, focusing electrodes, an electron multiplier (dynodes) and an anode in a vacuum tube, as shown in Figure 3.8. It works on the principle of photoelectric effect. In simple words when light hits the photocathode, the photocathode emits photoelectrons into vacuum. Photoelectrons are accelerated and focused by the focusing electrode onto the first dynode where they are multiplied by means of secondary electron emission. This secondary emission is repeated at each of the successive dynodes. The multiplied electrons are collected at the anode to produce output signal. [117]

The photocathode of a photomultiplier converts the energy of incident photons into photoelectrons. The conversion efficiency (photocathode sensitivity) varies with the incident light wavelength. This relationship between the photocathode and the incident light wavelength is referred to as the spectral response characteristics. The spectral response range is determined by the photocathode material on the long wavelength edge, and by the window material on the short wavelength edge. [118]



TPMHC0048EA

Figure 3.8: Cross section of a head on type PMT [118].

Spectral response is usually expressed in terms of quantum efficiency and radiant sensitivity. *Quantum efficiency (QE)* is defined as the ratio of the number of photoelectrons emitted from the photocathode to the number of incident photons. It's customarily stated in percentage. In the simplest form QE can be written as follows:

$$QE = \frac{\text{Number of photoelectrons}}{\text{Number of photons}} \times 100 (\%) \quad (3.3)$$

Radiant sensitivity (S) on the other hand is defined as the photoelectric current generated by the photocathode divided by the incident radiant flux at a given wavelength, expressed in units of amperes per watts (A/W). The equation of S is as follows:

$$S = \frac{\text{Photoelectric current}}{\text{Radiant power of light}} \times (A/W) \quad (3.4)$$

Finall there is also a relation between these two spectral response quantities i.e. QE and S which at a certain wavelength (λ) is given by:

$$QE = \frac{S \times 1240}{\lambda} \times 100 (\%) \quad (3.5)$$

where λ is the wavelength in nm.

Figure 3.9 that has been adapted from [94], shows how the quantum efficiency and radiant sensitivity changes for the R12199 PMT. Here we can see that the peak response of the PMT is at around 420nm.

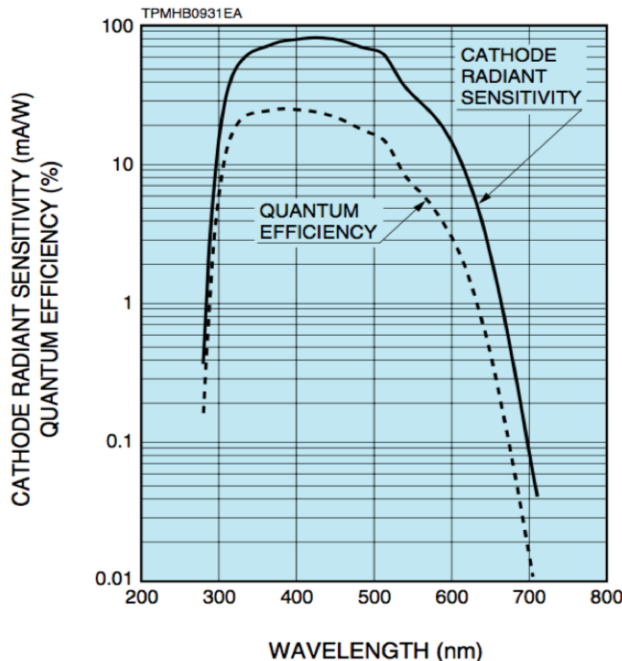


Figure 3.9: Spectral response parameters for R12199 (peak at 420 nm) [94].

3.4.4 PMT Characterization

One of the two main focusses of this work was the characterization of the PMTs used in the STRAW sDOMS. This section describes the important characteristics of photomultiplier tube operation and their evaluation methods, as well as their usage. As a preliminary step, an extensive characterization campaign on the adopted PMT was carried out before their integration into the sDOMS. The aim of this was to find the optimal working point for the PMTs, tailored on application features. In order to achieve a homogeneous response of the system, all the PMTs were set at the same gain. The measured quantities of each PMT include: single photoelectron (SPE) amplitude, gain, linearity, transit time spread (TTS) and an estimate of the dark counts. The setup used for the PMT characterization is described in Figure 3.10. It is mounted inside a sealed dark box and it is composed of: a picosecond pulsed laser (PiLas, $\lambda = (405 \pm 15)nm$, pulse width < 45 ps, up to 100 MHz), an optical attenuator (PiLas, attenuation range 0 to -80 dB), two different optical fiber splitters (50% and 10-90% emission ratio), a power meter (Newport 2936-R) with power probe (Newport 918D-UV-OD3R), and an oscilloscope (Teledyne LeCroy HDO6054, 500 MHz, 2.5 GS/s) [70].

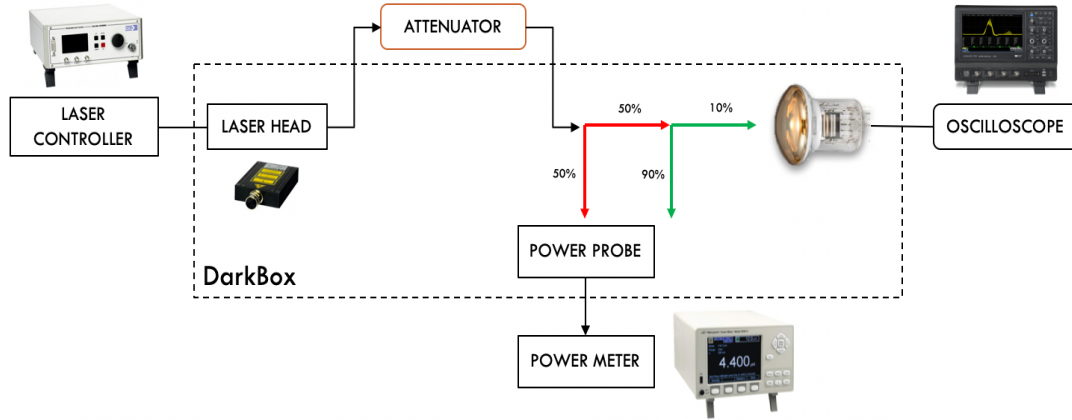


Figure 3.10: Setup scheme for the characterization of the PMTs [94].

3.4.4.1 Gain (or current amplification)

Photoelectrons that are emitted from a photocathode are accelerated by an electric field and strike the first dynode which leads to the emission of secondary electron. These secondary electrons then impinge upon the next dynode to produce additional secondary electron emissions. This process gets repeated over successive dynode stages (also called *cascade process*) and hence a high gain is achieved. Therefore a very small photoelectric current from the photocathode can be observed as a large output current from the anode of the PMT. Gain is simply the ratio of the anode output current to the photoelectric current from the photocathode. Ideally, the gain of the PMT is defined as δn , where n is the number of dynode stage and δ is an average secondary emission ratio. While the secondary electron emission ratio δ is given by

$$\delta = AE^\alpha \quad (3.6)$$

where A is constant, E is an interstage voltage, and α is a coefficient determined by the dynode material and geometric structure. It usually has a value of 0.7 to 0.8. When a voltage V is applied between the cathode and the anode of the PMT having n dynode stages, gain G becomes

$$G = (\delta)^n = (AE^\alpha)^n \quad (3.7)$$

$$\implies G = A^n \left(\frac{V}{1+n} \right)^{\alpha n} \quad (3.8)$$

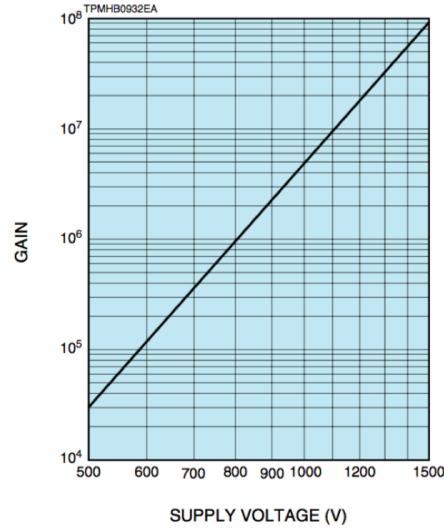


Figure 3.11: *Typical Gain characteristics of R12199 [94].*

From this equation, it is clear that the gain is proportional to the αn exponential power of the supply voltage. Figure 3.11 shows the typical gain characteristics i.e the gain vs. supply voltage for PMT R12199 as given by Hamamatsu.

It can be said that the current multiplication increases with the increasing supply voltage which means that the gain of a photomultiplier tube is susceptible to variations in the high-voltage power supply, such as drift, ripple, temperature stability, input regulation, and load regulation. Gain characterization was also done in the lab with the setup shown in Figure 3.10 for all the 10 PMTs with their own sockets. In order to measure the gain of the PMT, the single photoelectron charge was determined at different HV values. Simultaneously, for each HV value, the amplitudes of the single photoelectron signals have been measured (which was achieved by scaling down the laser light emission to the single photon level) with the aim of identifying the trigger thresholds for next steps. The acquisition was done by the oscilloscope, using the external trigger provided by the laser source.

Figures 3.12a shows the single photoelectron distribution at 1300V for one of the 10 PMTs characterized. On the other hand figure 3.12b shows the trend of the gain for the same PMT with HV on the x-axis. This was then done for all the other PMTs, the cumulative result for which is given in Figure 3.13. It was also noted in case of the single photoelectron

distribution that the peak moves away from the pedestal at higher PMT voltages.

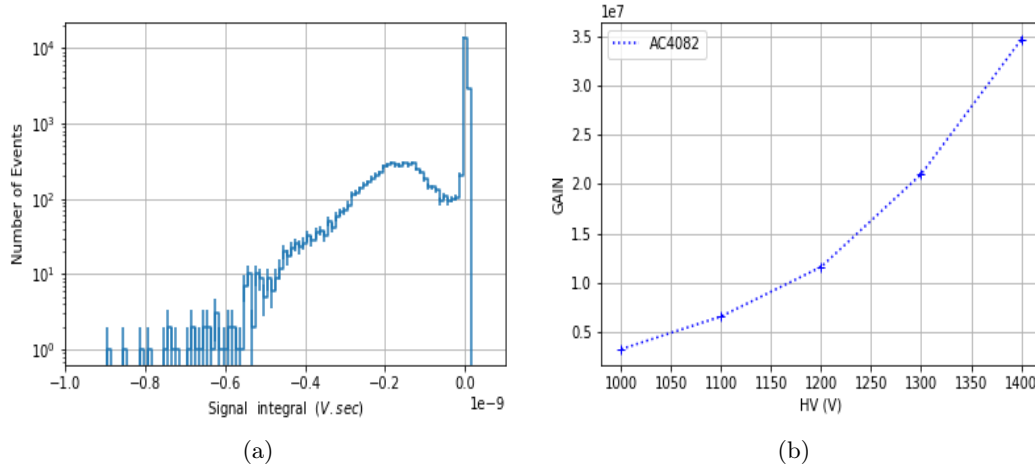


Figure 3.12: (a) Single photoelectron distribution at 1300 V and (b) Gain vs. supply voltage for AC4082.

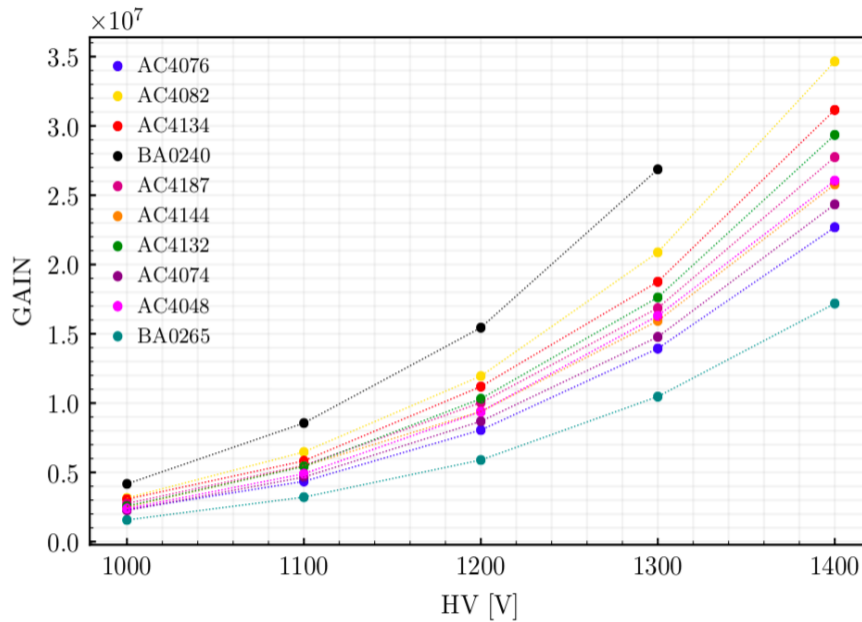


Figure 3.13: Gain vs. supply voltage for every PMT (tested with its own socket) of STRAW [70].

3.4.4.2 Dark current

A small amount of output current flows in a PMT even when it is operated in complete darkness. This current is called the anode dark current. The

dark current and the noise are critical factors to determine the lower limit of light detection. The causes of dark current may be categorized as follows [117] [118] :

- *Thermionic emission*: Since the materials of the photocathode and dynodes have very low work functions, thermionic electrons are emitted even at room temperatures. Most of the dark current originates from the thermionic emissions especially from the photocathode, and it is multiplied by the dynodes.
- *Ion feedback*: The flow of photoelectrons can ionize residual gases inside the PMT. When these ions strike the photocathode or earlier stages of dynodes, secondary electrons may be emitted. This could result in relatively large output noise pulses. These noise pulses are usually observed as afterpulses following the primary signal pulses and may cause problems in detecting short light pulses.
- *Glass scintillation*: Photocurrent can also be produced when electrons deviating from their normal trajectories strike the glass envelope causing scintillation and resulting in dark pulses. To eliminate these pulses, PMTs may be operated with the anode at high voltage and the cathode at the ground potential. Coating the glass bulb with a conductive paint connected to the cathode could also prove useful.
- *Ohmic leakage*: Insufficient insulation of the glass stem base and socket may lead to a leakage current between the anode and other electrodes inside the tube, and/or between the anode pin and other pins on the bulb stem. This could hence be another source of dark current. This is predominant when a PMT is operated at a low voltage or low temperature. Contamination by dirt and humidity on the surface of the tube may increase the chances of ohmic leakage, and therefore should be avoided.
- *Field emission*: When a PMT is operated at a voltage near the maximum rating value, some electrons may be emitted from electrodes by strong electric fields causing dark pulses. It is therefore recommended that the tube is operated at 100 V to 300 v lower than the maximum rating.

The anode dark current is known to decrease with time after a PMT is placed in darkness.

For the PMTs used in STRAW sDOMs, a long-term monitoring of the dark rate trend was performed revealing a day-night modulation induced by a slight temperature change in the laboratory. This modulation is not a matter of concern, since in its final working conditions, after the deployment at 2600 m depth in the Pacific Ocean, STRAW operates at a (stable) temperature of about 2°C . [70]

It was observed that the dark current increased with an increasing supply voltage, but the rate of increase was not constant. Figure 3.14 shows the dark rate trend vs. supply voltage characteristic for one of the sDOM PMTs. These measurements were taken after keeping the PMT for 24h in the dark and setting 1/3rd of the SPE amplitude as the threshold.

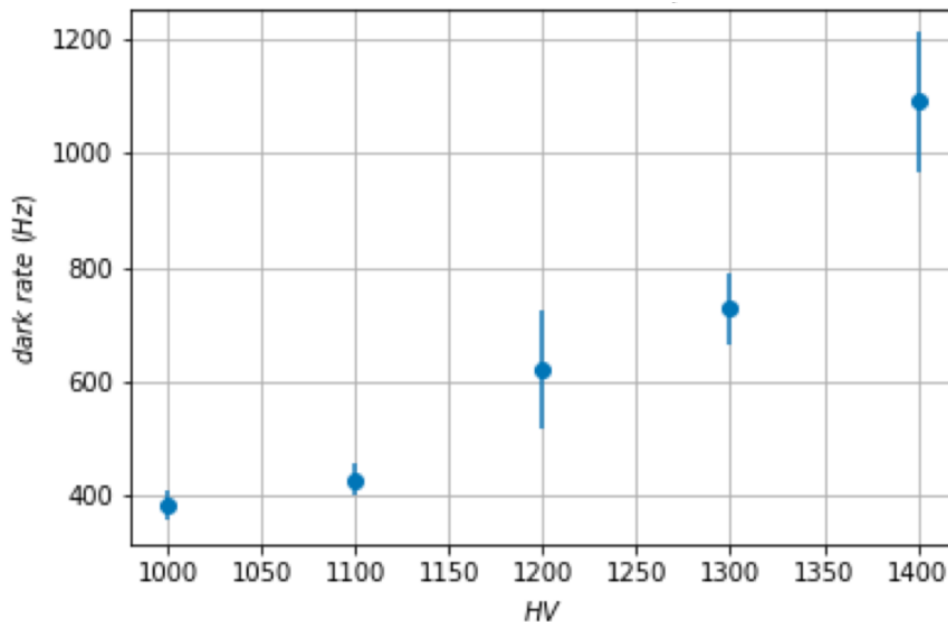


Figure 3.14: Dark rate trend in Hz for one of the sDOM PMTs [94].

3.4.4.3 Linearity

Another mandatory study done to better understand the PMT characteristics was the measurement and fine-tuning of the linearity and saturation of the PMTs. This was done in order to estimate the amount of POCAM light that would reach a certain sDOM over the two strings without saturating the PMTs.

In Figure 3.15 we show the trend of the saturation measurement vs. the input light power of three of the ten PMTs mounted in the sDOMs of STRAW. The dynamic range of the PMTs is expected to decrease with higher HVs (due to current saturation effects).

Figure 3.16 on the other hand shows the saturation trend vs. the number of incident photons for one of the sDOM PMTs. The number of photons has been calculated taking into account the readings of the power meter values, the frequency and the wavelength of laser light emission, while the number of electrons at the first dynode N_{pe} is calculated according to [117]

$$N_{pe} = \frac{Q_{TOT}}{G \cdot q_e} \quad (3.9)$$

where G is the Gain, Q_{TOT} is the total charge on the anode measured with the oscilloscope, and q_e is the electron charge.

In the linearity region, the slope of the fitted lines is the ratio between the number of photoelectrons that reach the first dynode and the number of incoming photons N_{ph} that hit the photocathode which is then given by the product of the quantum efficiency (Q.E) and the collection efficiency (C.E) of the PMT. The overall efficiency is therefore [117]

$$\frac{N_{pe}}{N_{ph}} = Q.E \times C.E \quad (3.10)$$

From Figure 3.16 it can also be inferred that the three slopes are in agreement and point to a value for the quantum efficiency (QE) of the PMT of around 29%.

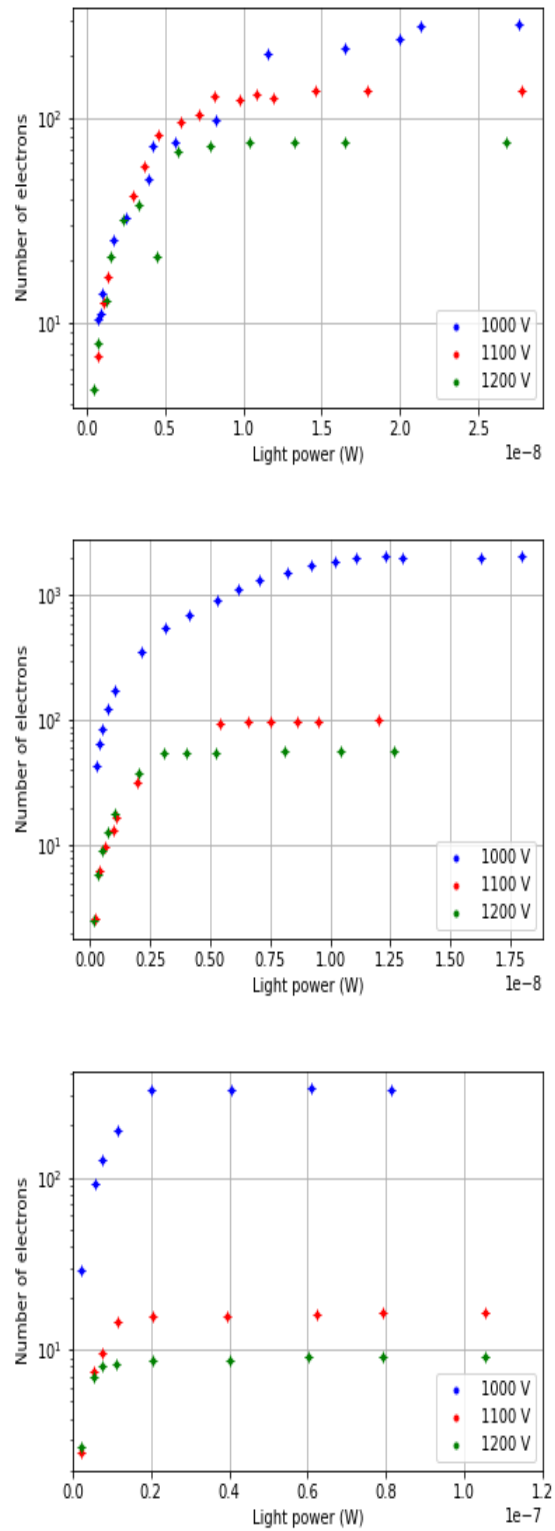


Figure 3.15: Saturation trend for three sDOM PMTs. Number of electrons vs the input Light Power(W)

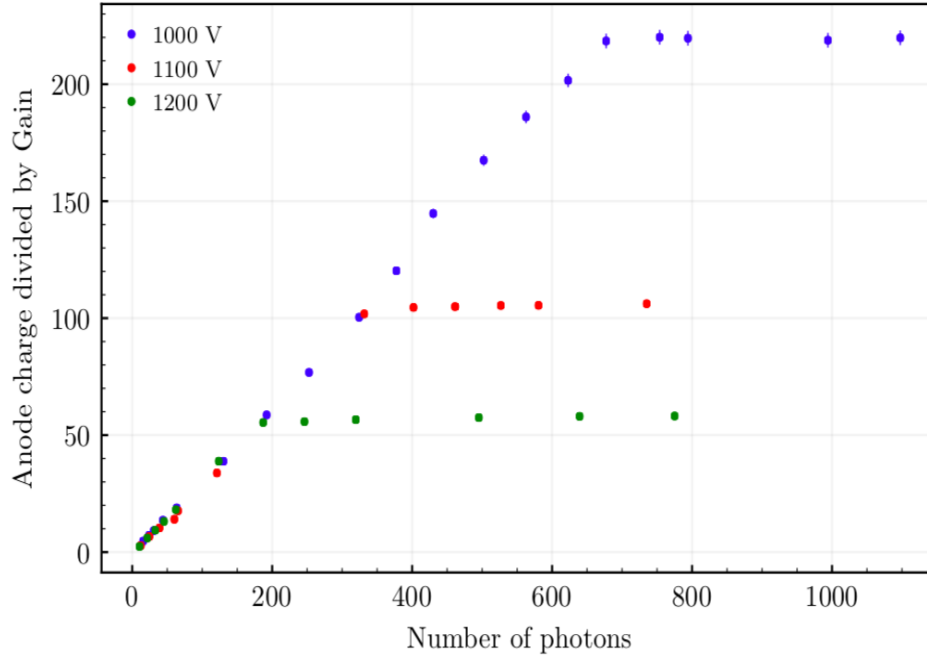


Figure 3.16: Saturation at different values of HV. Anode charge divided by the gain in units of elementary charge (e^- collected at the first dynode) vs. the number of photons impinging on the PMT [70].

3.4.4.4 Transit Time Spread or (TTS)

The photomultiplier tube is a photodetector that has an exceptionally fast time response. The time response is determined primarily by the transit time required for the photoelectrons emitted from the photocathode to reach the anode after being multiplied as well as the transit time difference between each photoelectron. Accordingly, fast response photomultiplier tubes are designed to have a spherical inner window and carefully engineered electrodes so that the transit time difference can be minimized.

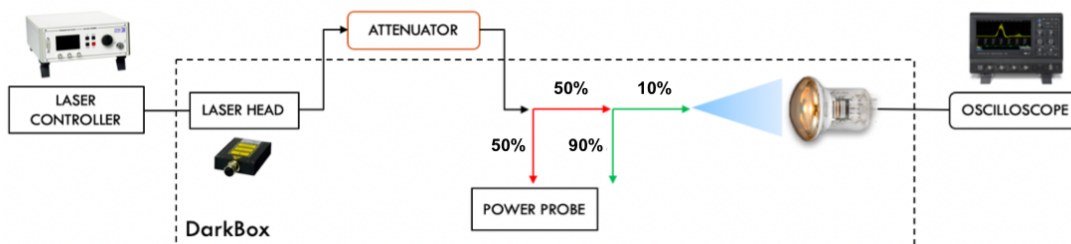


Figure 3.17: Setup for TTS measurement [94].

The time response is mainly determined by the dynode type, but also

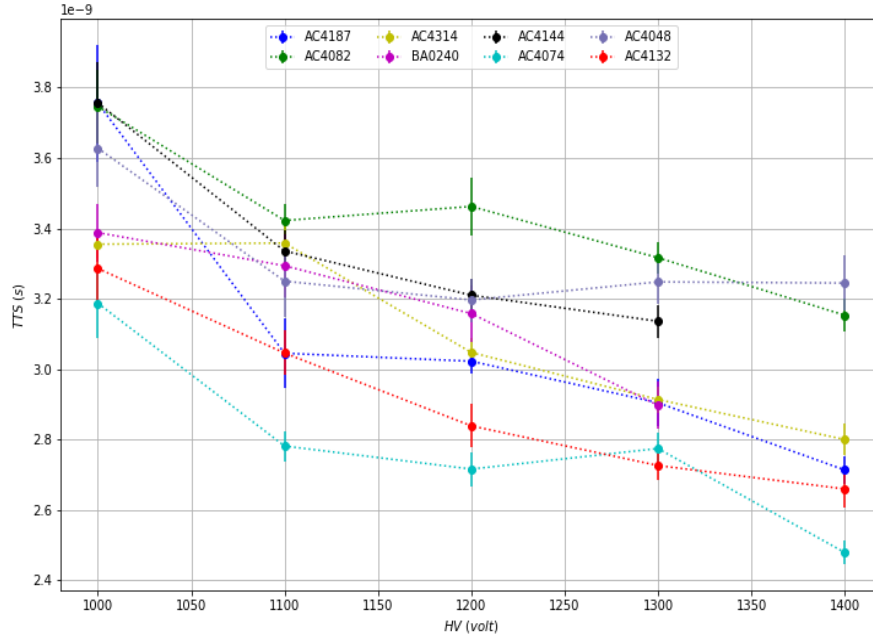


Figure 3.18: *Transit time spread trend at different HV for some PMTs used in STRAW: the value decreases with the increasing power supply [94].*

depends on the supply voltage. Increasing the electric field intensity or supply voltage improves the electron transit speed and thus shortens the transit time. In general, the time response improves in inverse proportion to the square root of the supply voltage. [118]

When a photocathode is fully illuminated with single photons, the transit time of each photoelectron pulse has a fluctuation. This fluctuation is called TTS (transit time spread) or the transit time jitter. This fluctuation in transit time between individual pulses may also be defined as the FWHM of the frequency distribution of electron transit times. T.T.S. mainly depends on the number of incident photons. A block diagram for TTS measurement scheme is shown in Figure 3.17 and typical measured data for some PMTs is shown in Figure 3.18. For the measurement of TTS the photocathode was fully illuminated with single photons. The external trigger of the Laser Controller was used as START and the output from the PMT was fed as the STOP signal via a discriminator. Finally the time interval between the "start" and "stop" signals was measured which is the

TTS or the FWHM of the distribution (setup shown in figure ??) [70].

3.4.5 Data readout

The PMTs are read-out using a Trigger Read-out Board (TRB3sc) and a PADIWA, both developed by GSI in Darmstadt which measures time-over-threshold (ToT) of the signal in multiple channels. The latter allows the reconstruction of charge and eventually the assessment of the absorption and scattering properties [70]. A central device, located inside both mini junction boxes, sends differential pulses with varying length to all TRB3sc in all sDOMs, where the pulses are measured by time-to-digital converters (TDC), and recorded by the trigger circuit inside the TRB3sc [93]. This allows event assembly across all sDOMs during the later analysis via software. A small Linux computer in each sDOM reads the TRB data and stores it locally. Timing calibration is therefore provided by checking the sDOM signal against the pulse length of the synchronization signal in the measured data, taking into account the signal run time through the data cable [93].

3.5 Testing, Deployment and First Data

Since only the calibration of the PMTs was one of the major works of this thesis, [70] has been referred for this section.

Testing: Both module housings of the POCAM and the sDOM were subject to environmental tests to guarantee their use in deep-sea applications. Both housings withstood vibration tests, several shock test as well other the standard test for subsea equipment. Furthermore, the new housing of the sDOM was successfully tested in a pressure chamber at the company Nautilus with a pressure sweep up to 385 bar qualifying for operating at a depth of 2600 m in the Cascadia Basin. The modules were also tested for their angular acceptance by operating them under water inside a custom-built darkened pool, which has been built at TUM. Specific holding structures were designed to place and rotate a POCAM and an sDOM independently and thus determining the angular acceptance between the two modules.

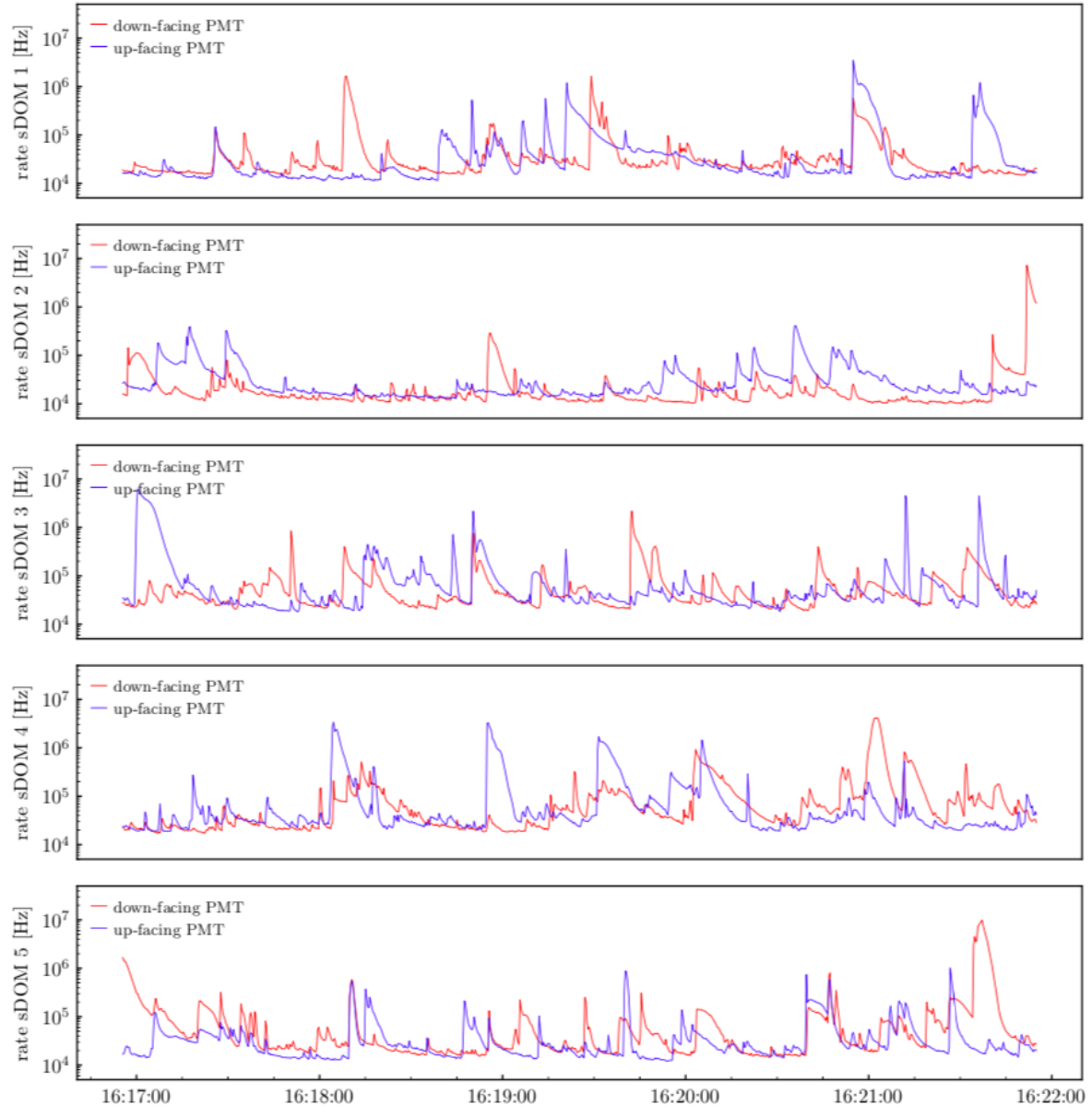


Figure 3.19: *Dark rates recorded by all five sDOMs for five minutes at a readout rate of 3 Hz. In this representation the fine structure of the flashes most likely caused by bioluminescence are visible [70].*

The modules were tested again at the ONC facilities for any current leakage or ground faults that might have resulted from the shipment to Canada. The modules were operated for about 10 minutes each in a salt-water pool and the ground current was monitored. No issues were identified during this test phase. Lastly, a test that lasted for several days, to test for water leakage and ensure proper functionality in a salt-water environment, was also performed on the fully integrated strings in a salt-water test pool at the ONC marine technology center. To be fully cautious, 3D-printed

protective shells covered and remained on the modules until right before the deployment. The ONC IT team also ran some tests with a driver software to make the measured data available on the ONC website.

Deployment: STRAW was deployed via top-down approach. The mooring lines were transported on custom-made spooling systems. Each spool being powered by an engine, allowed controlled winding. During the deployment and after the connection of the two buoys, a second smaller boat secured the top of the string during the unspooling in water. When the string was almost entirely in water the Mini Junction Boxes and the anchor were mounted at the end of the string. Before final deployment, an electric test of the mounted string was performed. Right after the test, the anchor was lifted into the sea via a crane on the back deck. At a controlled speed of 0.3 m/s, the whole structure was then lowered to the sea floor. After the anchor landed on the seabed, an acoustic release ensured the disconnection from the heavy lift line.

First Data: Figure 3.19 shows the rates measured by all the ten deployed sDOM PMTs over the course of 24 h. The rate varies between ca. 10 kHz and 100 kHz with spikes reaching several MHz for a few seconds. One of the major reasons for these spikes can be explained by the ambient bioluminescence from deep-sea animals and microorganisms.

The second focus of this work will be the study of bioluminescence in the deep sea and the expected wavelength range of these flashes. Moreover an idea for development of a spectrometer module for a third possible string in STRAW called STRAW-b will also be presented. STRAW-b will have various calibration modules and will be talked about in detail in the following chapter.



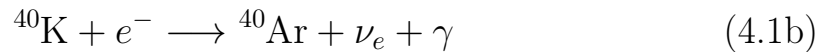
STRAW-b

The previous chapter discussed the idea and motivation behind the STRAW project. It was developed and deployed within an 8-month timeline and is presently taking data for the past few months now. As was discussed in the last section of the previous chapter, the sDOMs in STRAW see light from the POCAM as well as show peaked rates (upto \sim MHz) for some intervals. These flashes can be explained by the bioluminescence produced by various species in the deep sea. Apart from bioluminescence, radioactivity due ^{40}K present in the water and in glass hemispheres that are part of the sDOM and POCAM, and the atmospheric muons play a major role in being some of the sources of background in the STRAW detector site. This led to the possibility of a potential upgrade of STRAW called *STRAW-b*. The development of this upgrade is still *work in progress* and will be realized in 2020 with the deployment of a 500 m long mooring line with various modules to assess additional properties of the Cascadia Basin site.

4.1 Background radiation in the deep-sea

Daylight does not penetrate at any detectable level to depths beyond a kilometre. Backgrounds in a neutrino telescope can occur either by random light, not associated with particles traversing the detector, or by muons in air showers produce by cosmic ray interactions in the atmosphere. Thus *atmospheric muons* can penetrate the water above the detector and give rise to a reducible background. Moreover, sea water contains small amounts of the naturally occurring *radioactive potassium isotope*, ^{40}K , which via β -decay produces electrons which can further result in Cherenkov light

thereby producing a steady background of photons with rates of the order of 350 Hz/cm^2 . This isotope decays mostly through β -decay releasing electrons that produce Cherenkov light and produce a steady, isotropic background of photons with rates of the order of 350 Hz/cm^2 . Of all the radioactive isotopes present in natural sea water ^{40}K is by far the dominant one. Both ^{40}K decay channels



contribute to the production of optical noise in underwater neutrino detectors. Many life forms that inhabit the deep sea emit light. This emission, also called *bioluminescence*, has two contributions, a continuous component usually attributed to bioluminescent bacteria, and a component of localised bursts of light with high rates probably connected to macroscopic organisms passing the detector as was seen in the previous chapter. The next section will prominently discuss the background produced by bioluminescent life form in the deep sea.

4.2 Bioluminescence

Emission of visible light by an organism as a result of a natural chemical reaction is called bioluminescence. A large diversity of marine animals, microbes and even plants are able to produce their own light, making bioluminescence one of the most prominent sources of light in the ocean [89]. Bioluminescence is thus present everywhere in the deep sea and is believed to come from two major sources - the steady glow of bacteria and flashes produced by animals. The optical background due to these flashes is several orders of magnitude more than the one due to ^{40}K . Relatively little is known about bioluminescence at great depths [[89].

4.2.1 Bioluminescence spectrum

The colour of bioluminescent signal strongly depends on the organisms habitat. Thus, deep-sea species have blue emissions (450–490 nm), the bioluminescence of coastal marine species is green (490–520 nm), whereas of terrestrial and fresh water species is red (550–580 nm) [95]. The typical spectrum of bioluminescence light is centred around 470–480 nm [117] [118].

The wavelength of maximal transparency of water i.e 470 - 480 nm, which is also the range of the emissions by deep-sea species is of greatest interest for undersea neutrino telescopes.

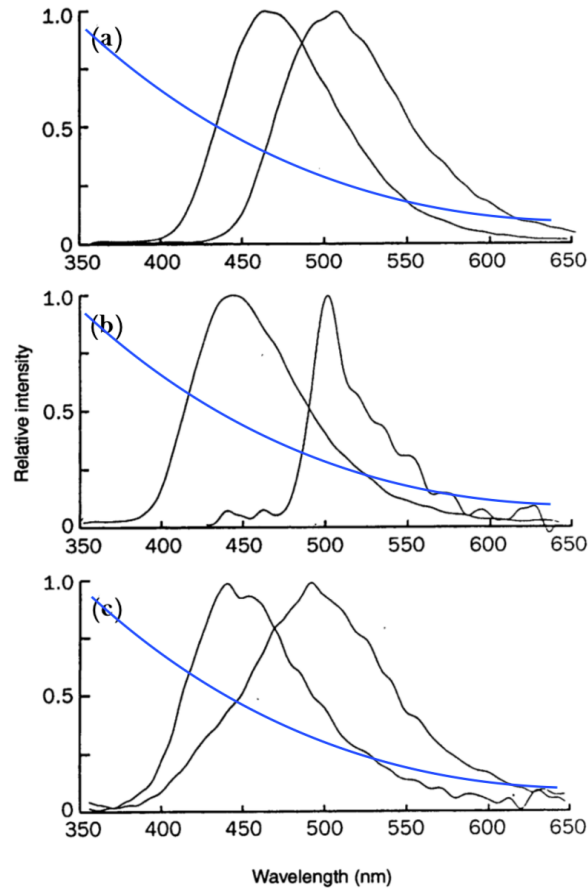


Figure 4.1: Representative spectra from extremes of each group of zooplankton (a) ctenophores with extremes at 464 nm and 502 nm. (b) medusae with extremes at 441 nm and 502 nm, irregularity in the second spectrum is due to smoothing of relatively noisy signal. (c) siphonophores: in this group, several species produced two colors of luminescence; surprisingly, *Bargmannia elongata* which emitted blue light (446 nm) and green light (493 nm) provided best examples of both extremes for siphonophores [88].

Figure 4.1 shows typical examples of the bioluminescence spectra for three groups of gelatinous zooplankton examined in [88]. The distribution of luminescent organisms, in the deep-sea varies with location, depth, and time but there is a general pattern of decrease in abundance with depth. Table 4.1 gives a detailed insight of the wavelength of light flashes produced from the various species in figure 4.1 and the depths they were collected from.

Table 4.1: Mean wavelengths of luminescence for groups of organisms tested [88]

Group	Mean(nm) \pm SE(standard error)	n
Ctenophores		
Shallow	490.8 \pm 1.6	18
Deep	482.3 \pm 2.2	23
Total	486.1 \pm 1.6	41
Medusae		
Shallow	494.7 \pm 6.4	7
Deep	468.4 \pm 2.3	27
Total	473.8 \pm 2.8	34
Siphonophores		
Green	486.3 \pm 2.3	9
Blue	450.0 \pm 1.3	16
Total		25

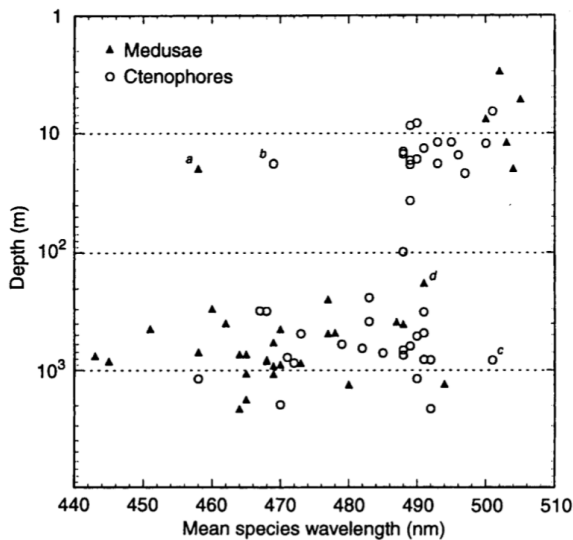


Figure 4.2: Relationship between wavelength of maximum emission and depth [88].

Finally, Figure 4.2, which was also adapted from [88], shows the wavelength dependence of bioluminescence with the depth for two of the three species talked about above. The most interesting overall trend is the clear distinction between shallow and deep populations of each species. Since the study of bioluminescence in the deep sea is yet to be thoroughly studied, depth distributions can therefore not be rigidly restricted [104].

4.3 Motivation for STRAW-b

The PMTs in the STRAW sDOMs also see very high rates at certain times. From STRAW it was inferred that this could be due a bioluminescent animal passing through the detector volume. One of the doctoral candidates of the group, I.C Rea, found a pyrosome entangled around an sDOM on one

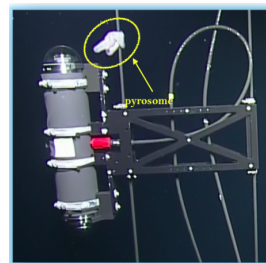


Figure 4.3: Pyrosome entangled on the STRAW string [courtesy I.C.Rea]

of the STRAW strings, in a picture of the STRAW detector taken underwater. The measurement of this radiation background proved to be one of the paramount motivations for building an upgrade for STRAW called STRAW-b. This upgrade aims to determine, apart from other background due to radioactivity, the wavelength of bioluminescence flashes in the Cascadia basin.

4.4 Modules

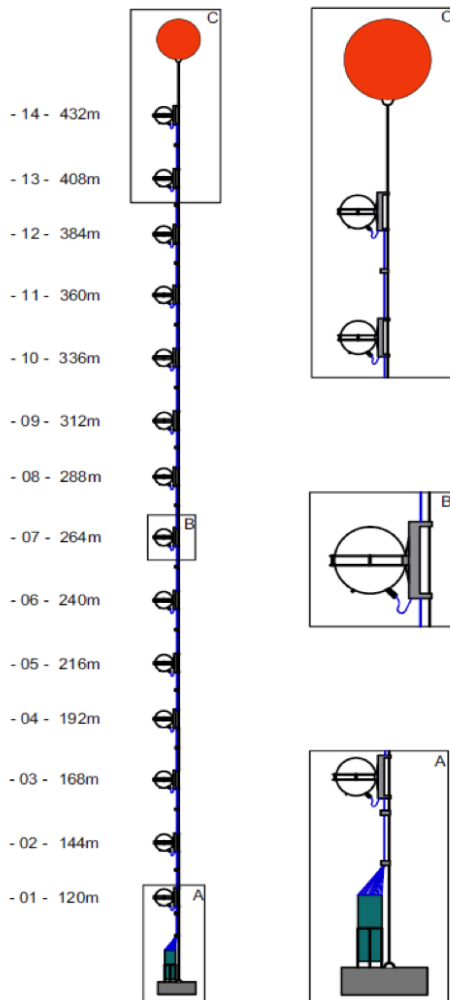


Figure 4.4: *STRAW-b string outline [Courtesy C. Spannfellner].*

Each module will also be provided with an ethernet connection and a 48V supply. Figure 4.5 shows a schematic of the standard module, courtesy C. Spannfellner.

STRAW-b is a 500m long mooring line, which will have various modules to assess additional properties of the STRAW detector site. So far this string is planned to consist of 5 standard modules and 5 specialized modules. Each module is housed in a 13" glass sphere. Glass hemispheres are held together by steel rings and an internal aluminium plate will mount the arbitrary electronics

4.4.1 Standard Module

The standard module is the basis for all the modules. It will host the TRBsc, Padiwa and Odroid system. The TRBsc and PADIWA are the similar ones used in STRAW. The standard module will carry out the measurement of time-over-threshold with upto 4 thresholds. It will provide 16 channels to the instrumentation, which will be amplified



Figure 4.5: Sketch of the standard module in STRAW-b showing the mounting system and the glass sphere with the lower half for the electronics and upper half for the specialized instrumentation [Courtesy C. Spannfellner].

4.4.2 Specialized Modules

Apart from 5 standard modules, STRAW-b will also have 5 specialized modules, which are nothing but the standard modules with special instrumentation on top of all the electronics under the aluminium plate. So far two PMT based spectrometer modules, one stand alone spectrometer module, a muon tracker and a LIDAR module are planned. The muon tracker is designed to measure the muon rate in the Pacific. It consists of two plates placed at a certain distance, each comprising of four plastic scintillator tiles. The energy deposited by the muon is read-out by SiPm arrays. By knowing which tile was hit, one gets information about the approximate direction of the muon. The LIDAR (Light Detection And Ranging) device within STRAW-b will serve as an alternative approach for measuring the absorption length and scattering properties at Cascadia Basin in order to complement the STRAW measurements. A scintillator module for radioactivity measurements was also planned but has now been cancelled. This work will lay emphasis only on the preliminary design and ideas of the spectrometer modules.

4.5 Spectrometer Module (I)

The basic function of a spectrometer is to take in light, break it into its spectral components, digitize the signal as a function of wavelength and read it out and display it through a computer. The first step in this process is to direct light through a fibre optic cable into the spectrometer through a narrow slit. In most spectrometers, the divergent light is then collimated by a concave mirror and directed onto a grating. The grating then disperses

the spectral components of the light at slightly varying angles, which is then focused by a second concave mirror and imaged onto the detector. [108]

The idea behind building a spectrometer module was to measure the spectrum of bioluminescence flashes in the Cascadia Basin site. As of now two approaches have emerged for building this module and are currently being worked upon. The first involves the use of a stand alone mini spectrometer by Hamamatsu whereas the second approach will use PMTs coupled with lenses and narrow width bandpass filters.

4.5.1 Mini-spectrometer

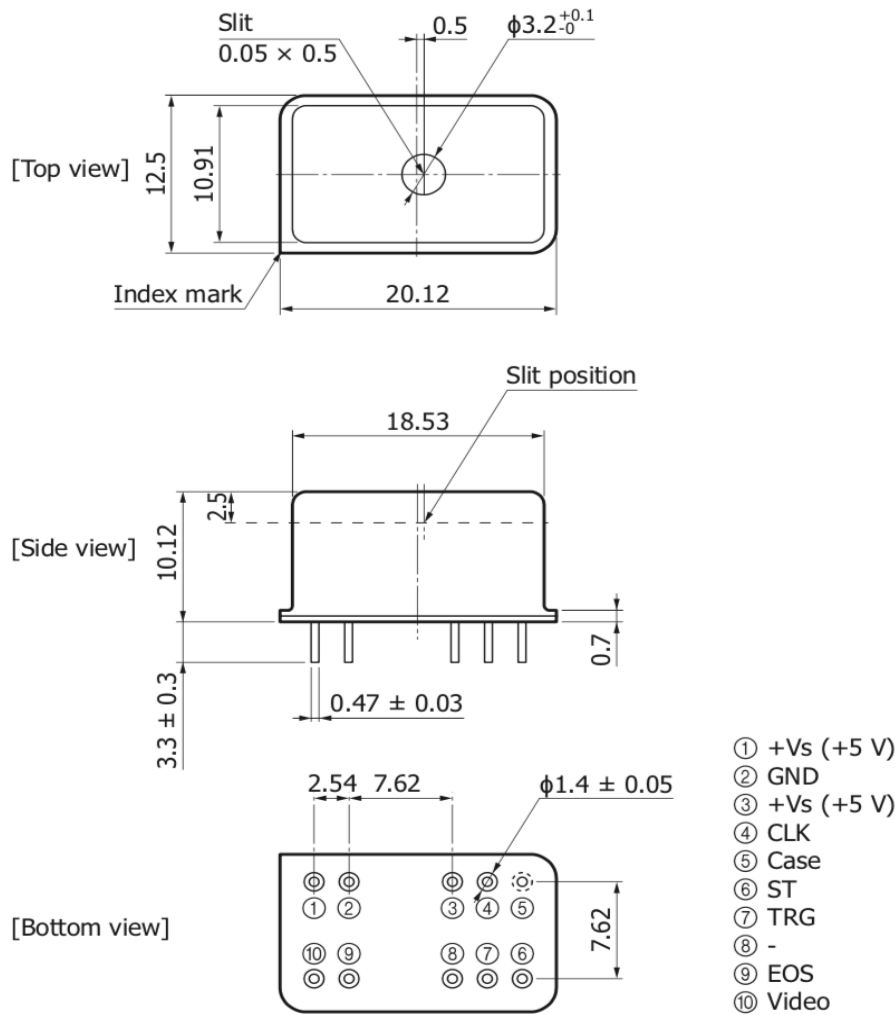
Mini-spectrometers are compact spectrometers whose optical system, image sensor, and circuit are condensed into a small case. In contrast to conventional spectrometer instruments, mini-spectrometers are compact and portable, making it possible to take real-time measurements on-site, rather than having to bring in measurement samples into a room in which a spectroscopic instrument is installed. This miniaturization thus made it possible to incorporate them into various types of equipment. The micro-series spectrometer C12880MA (Figure 4.6) by Hamamatsu is one of the two proposed ideas for the spectrometer module.



Figure 4.6: *Mini spectrometer C12880MA from Hamamatsu [5].*

Hamamatsu's C12880MA :The C12880MA is a highly sensitive, ultra-compact, finger-tip sized spectrometer head that supports the long wavelength region (up to 850 nm). Its airtight packaging provides improved humidity resistance and is also deemed suitable for integration into a variety of compact devices. It has a high-sensitivity CMOS (complementary metal-oxide semiconductor) linear image sensor with a slit. The entrance

slit aperture size is $50 \mu\text{m} \times 500 \mu\text{m}$. It weighs only 5 grams and has the dimensions $20.1 \text{ mm} \times 12.5 \text{ mm} \times 10.1 \text{ mm}$. It has a spectral response range from visible to near infrared (340-850 nm) and a maximum resolution of 15 nm. The C12880MA also employs a reflective concave blazed grating formed by nanoimprint. A dimensional structure of this spectrometer is shown in figure 4.7 [108], where we see the top, side and bottom view of the device with the specifications such as the width, length, height, slit dimensions and pin connections.



KACCA0356EB

Figure 4.7: Dimensional sketch (units:mm) of C12880MA [108].

The incident light enters through the input slit and falls on the grating chip provided inside the spectrometer. This grating, which is reflecting and concave, splits the light into its component colors and directs it towards the

CMOS sensor (Fig.4.8). CMOS image sensor built into the C12880MA has a large charge-to-voltage conversion gain. To perform high S/N (signal to noise ratio) measurement it is recommended to use the device even when the light level is low ($\sim 10^{-14}$ Watt). Depending on which of the 288 pixels are hit, the spectrometer can tell the corresponding wavelength of the light. A circuit board (named C13016) designed to simply evaluate the characteristics of the micro-spectrometer is also available separately. The micro-spectrometer is connected to a PC with a USB cable (named A9160). An exemplary connection for the same is shown in Figure 4.8 [108].

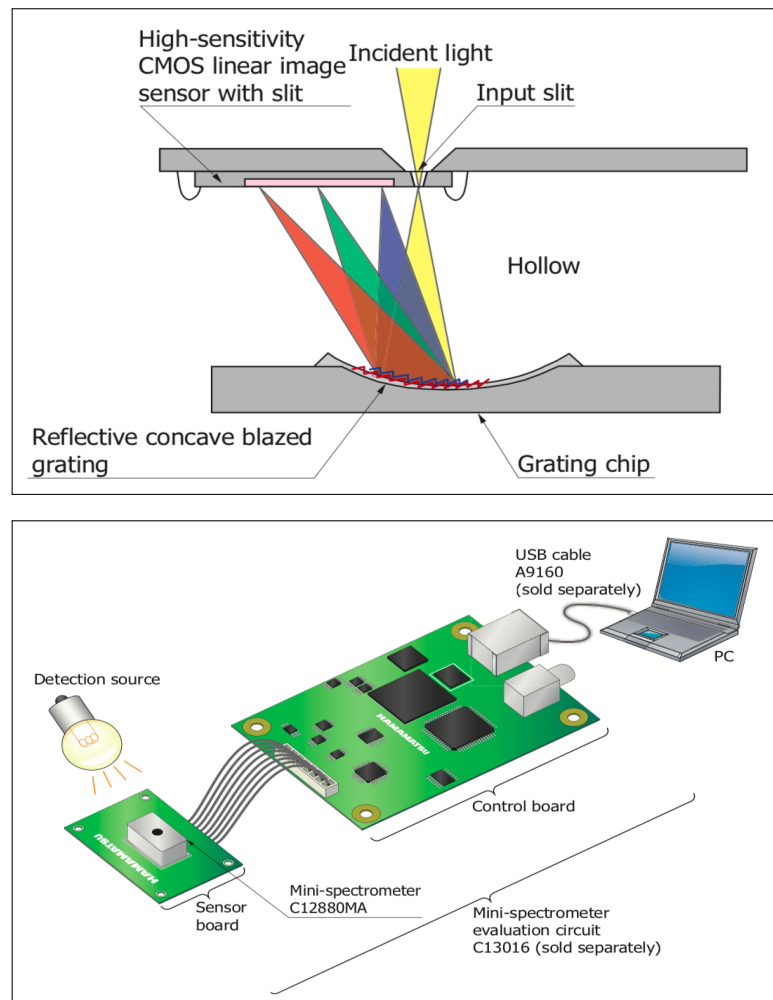


Figure 4.8: (top): C12880MA structure, (bottom): Exemplary connection of C12880MA on the circuit board C13016 connected via USB to the computer. [108]

An evaluation software, which only works with Windows comes with the

spectrometer. According to the hamamatsu data sheet the relationship between pixel p and wavelength λ is given by a fifth order polynomial

$$\lambda = A_0 + B_1p + B_2p^2 + B_3p^3 + B_4p^4 + B_5p^5 \quad (4.2)$$

where the coefficients have values $A_0 = 3.159526665 \times 10^2$,
 $B_1 = 2.708938073$,
 $B_2 = -1.232481824 \times 10^{-3}$,
 $B_3 = -6.837113718 \times 10^{-6}$,
 $B_4 = 5.900799329 \times 10^{-9}$ and
 $B_5 = 9.382541540 \times 10^{-12}$.

These values were found to be in agreement with the fit (Figure 4.9) obtained while taking measurements. The measurement procedure will be explained in the following paragraphs.

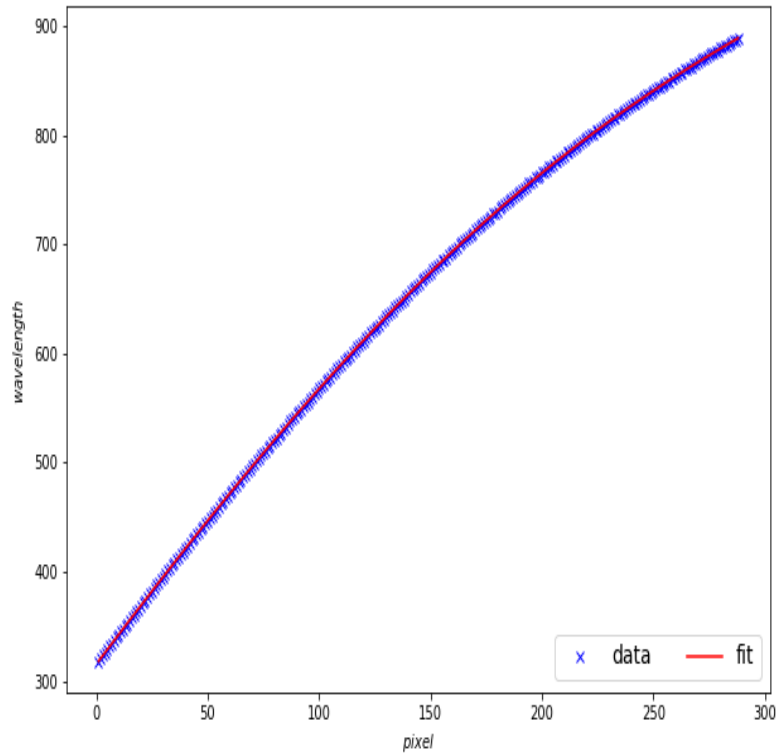


Figure 4.9: *Wavelength - pixel relationship for C12880MA*

4.5.2 Preliminary investigation of C12880MA

The tests with the spectrometer started with first installing the mini-spectrometer software provided by Hamamatsu. After this installation, the spectrometer was merely tested by flashing different colors of light and seeing the corresponding output spectra.

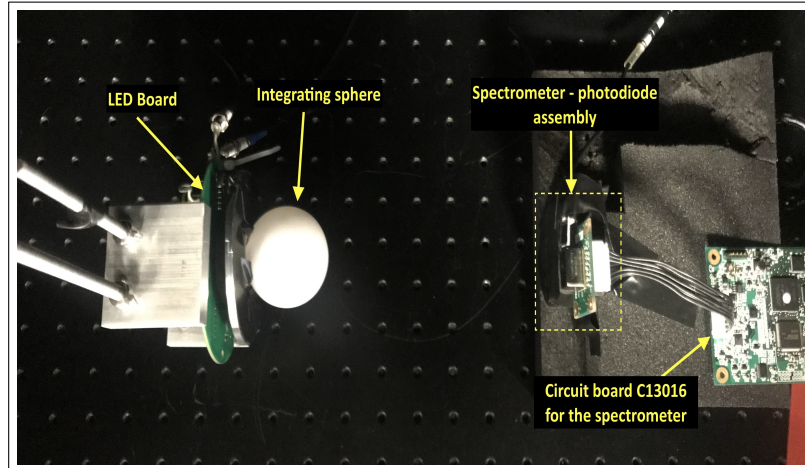


Figure 4.10: Setup within the dark box showing an LED matrix that sends light through the teflon sphere to the spectrometer and the photodiode placed symmetrically on either side of the integrating sphere axis.

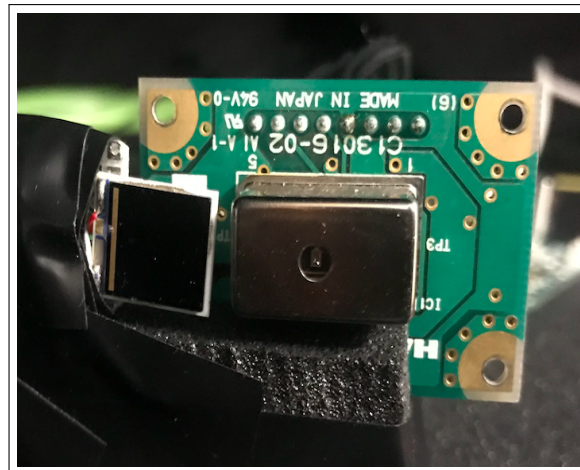


Figure 4.11: Closeup of the photocathode and mini-spectrometer arrangement

Further investigation was done by creating a setup inside a darkbox, as shown in figure 4.10 to measure the spectrum of different wavelengths of light from the POCAM LED Matrix. The LED matrix was connected to a teflon sphere, similar to the one used in the POCAM of STRAW, so as

to isotropically diffuse the light from the LEDs. The spectrometer along with a photodiode (fig 4.12) was placed at different distances (0cm, 10cm, 30cm and 50cm) and the spectra for the four LEDs was measured. The software allows us to measure the spectra at different integration times from 100 μs up to 1 sec.

4.5.3 Results

This section will show the different plot that were generated and some spectra that the micro-spectrometer generates. The measurements were done at 4 different wavelengths, at different distances, different input voltages and different integration times. From all the measurements it became clear that the spectrometer successfully generated a spectrum only for integration times larger than 10000 μs . Below this value, the spectrometer apparently was unable to see enough light to be able to generate a spectrum.

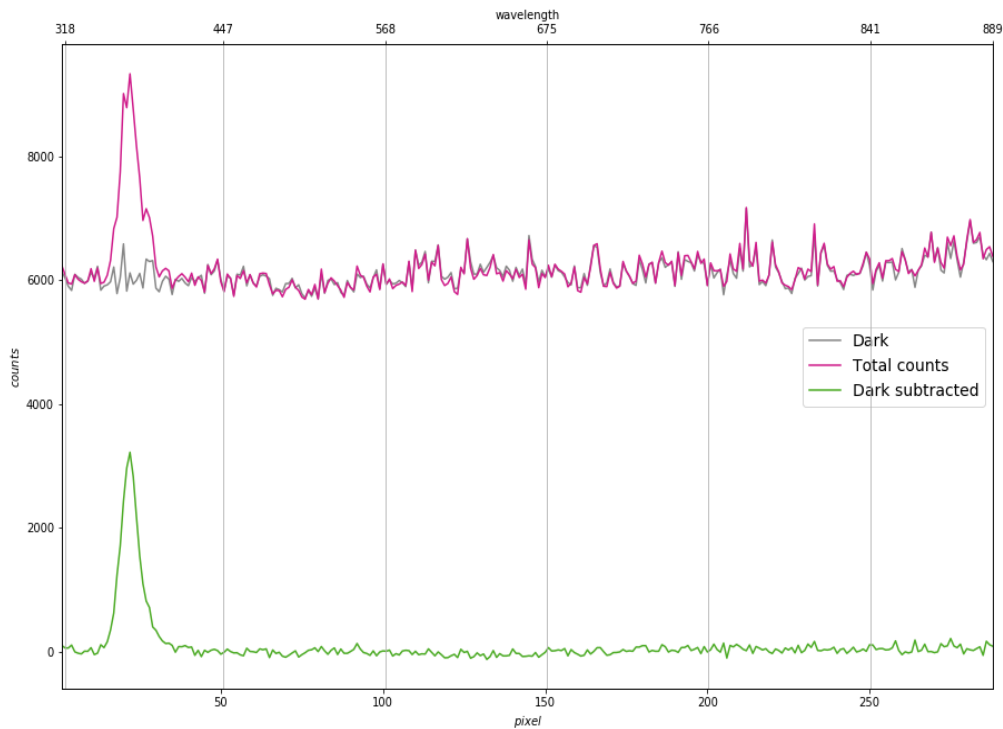


Figure 4.12: *The dark rate spectrum (grey), the total spectrum (pink) and the dark rate subtracted spectrum (green) of the 374 nm LED at 0 cm from the integrating sphere and 1 s integration time*

Further analysis to evaluate the sensitivity of the mini-spectrometer by understanding the photons emitted by the source and those detected by

the photodiode is still under investigation and will be a part of the doctoral thesis of *I.C.Rea*.

The mini-spectrometer could also possibly be integrated in all the standard modules rather than just one because of its state of the art compactness. A new circuit board to read this device is also under construction so that it can be read out via Linux systems too.

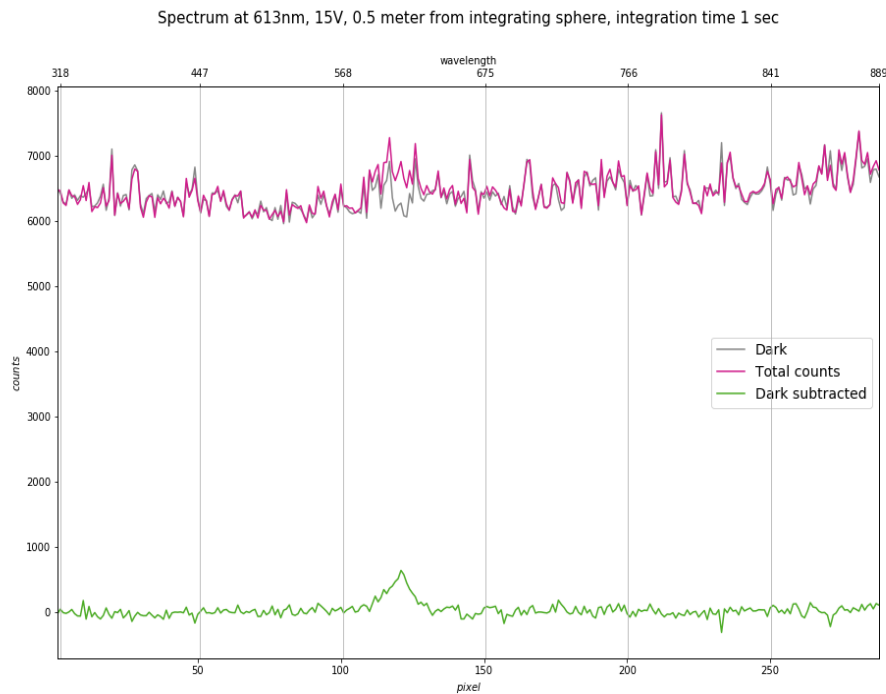


Figure 4.13: Another dark rate spectrum (grey), the total spectrum (pink) and the dark rate subtracted spectrum (green) of the 613 nm LED at 50 cm from the integrating sphere and 1 s integration time

The plots in figure [4.14](#), [4.15](#), [4.16](#) and [4.17](#) show the variation of the distance with counts for all the four LEDs. Note that for the 374nm LED, the spectrometer generated a spectrum only at 1sec integration time. It is clear and intuitive that as the spectrometer moves away from the light source, the number of photons reaching the spectrometer decreases.

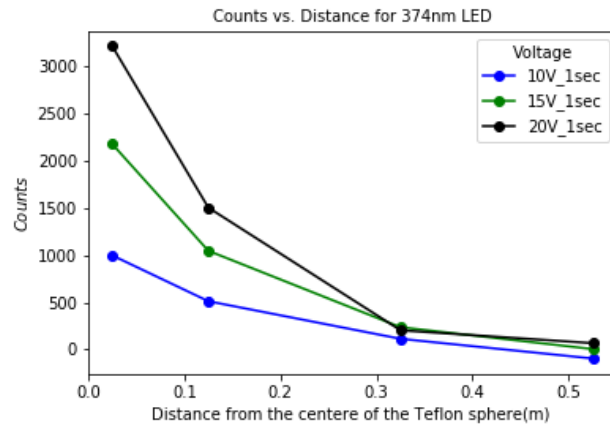


Figure 4.14: *Distance vs. counts for 374nm*

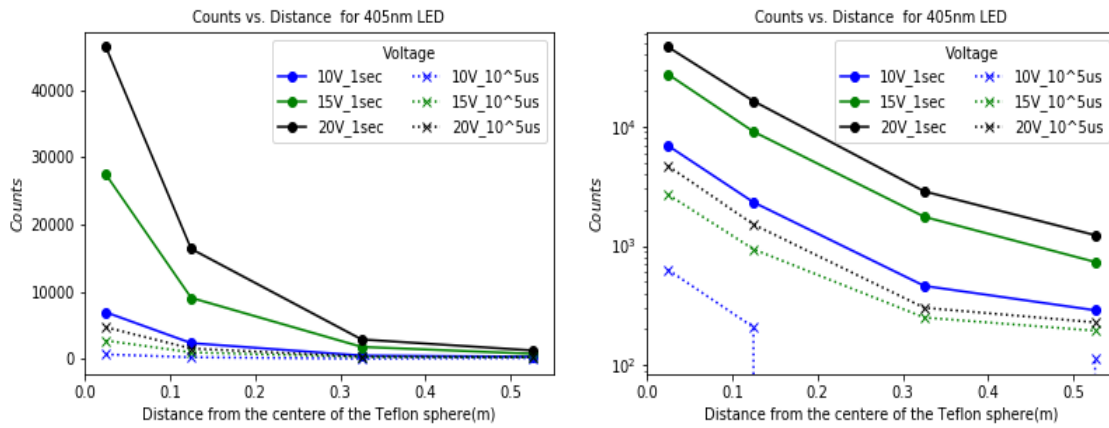


Figure 4.15: (left) *Distance vs. counts for 405 nm* (right) *Distance vs. counts in log scale for 405 nm*

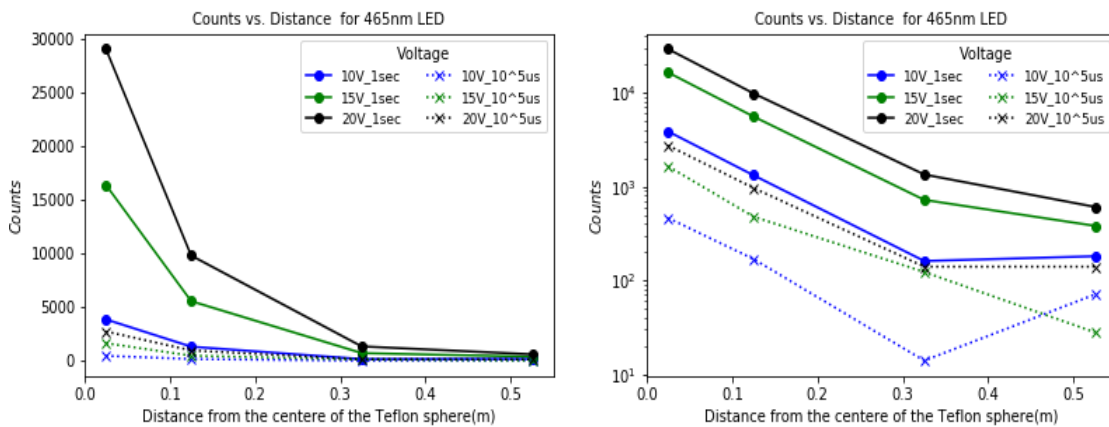


Figure 4.16: (left) *Distance vs. counts for 465 nm* (right) *Distance vs. counts in log scale for 465 nm*

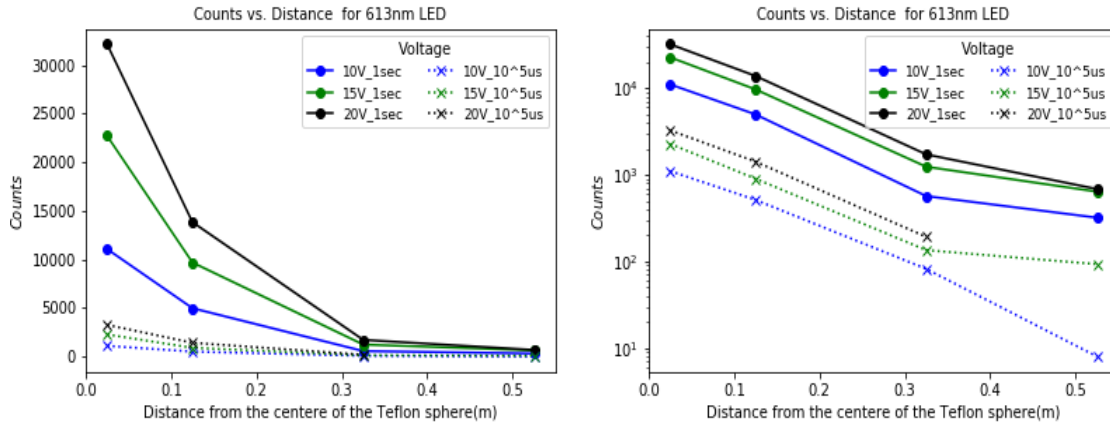


Figure 4.17: (left) Distance vs. counts for 613nm (right) Distance vs. counts in log scale for 613nm

4.6 Spectrometer Module (II)

Another complementary idea put forward for the measurement of bioluminescence in the deep sea was the use of PMTs. These PMTs will be coupled with lenses and bandpass filters. A band-pass filter, also bandpass filter or BPF, is a device that passes wavelengths within a certain range and rejects wavelengths outside that range. In this application, narrow width bandpass filters from Edmund Optics will be used.



Figure 4.18: Hamamatsu R1924A 1 inch PMT [103].

4.6.1 Setup

As mentioned in section 4.2, the expected spectrum of bioluminescence in the deep sea lies in the range of 440 nm to 490 nm. The glass spheres for the specialized modules have a radius of 15 cm with nearly 8 cm at the bottom containing the electronics, leaving around 22 cm for this setup to fit in (figure 4.19). Figure 4.20 shows a sketch of the top view of this module.

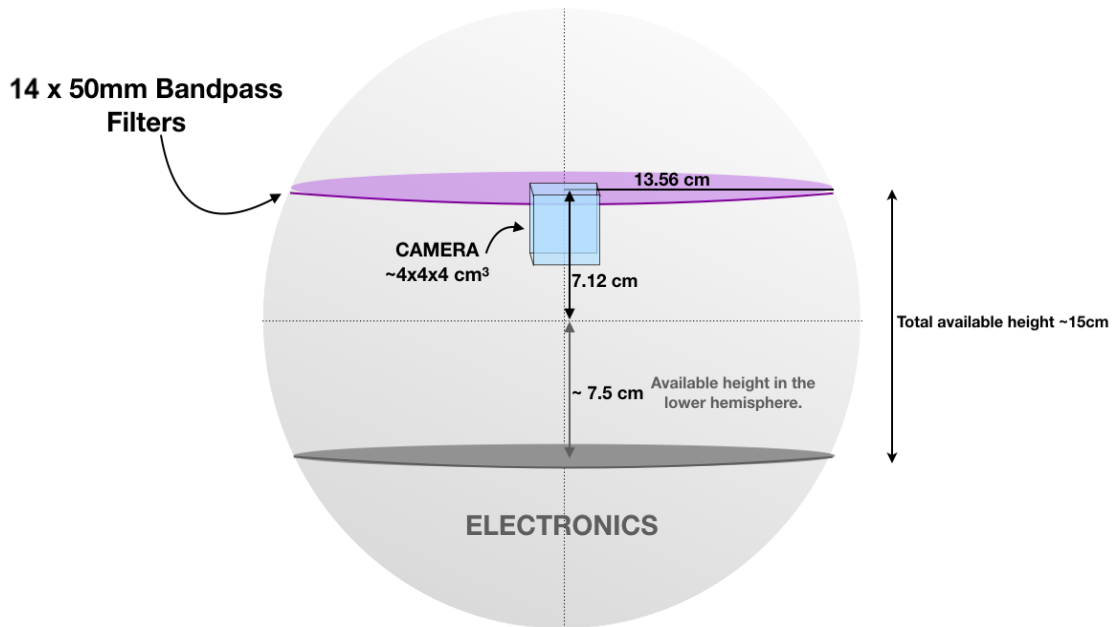


Figure 4.19: Specifications of the PMT spectrometer

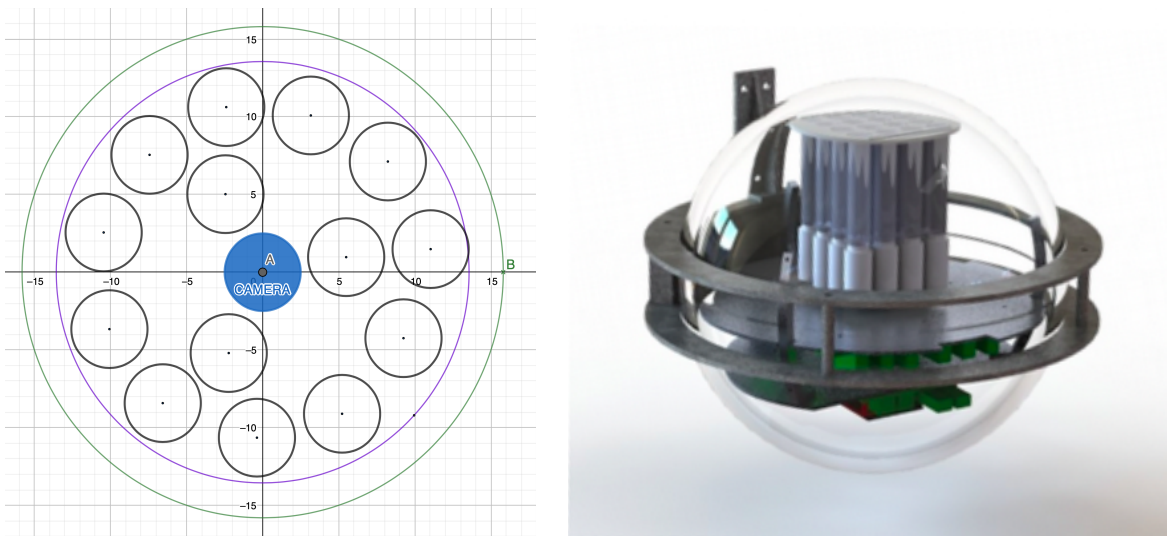


Figure 4.20: (left) Top view sketch of the spectrometer module. Black rings are the bandpass filters and the numbers on the axis are to get an idea of the dimensions of the components (right) 3D sketch of the module (Courtesy C. Spannfellner)

The PMT spectrometer module will consist of 14 one inch PMTs - Hamamatsu's R1924A, each coupled with a lens and a two inch bandpass filter. The bandpass filters are chosen in the range of 375nm to 580 nm with narrow range filters in the 440 nm - 490 nm region since it is the most prominent region for deep sea bioluminescence. R1924A is head-on type

PMT having a bialkali photocathode with an effective diameter of 22 mm and a spectral response in the range of 300 to 650 nm. This PMT has a gain of 2.0×10^6 and a quantum efficiency of nearly 26% peaked at 420 nm. The 14 PMTs are arranged in an array close to surface of the glass sphere and the space between glass sphere and array is filled up with optical gel hereby reducing optical effects. In addition a camera would also be mounted in the center of the PMTs which will be triggered when the PMTs see high rates and record pictures of the event. The read-out of the PMTs will be done via existing TRB3sc and Padiwa3 similar to the sDOM. The power supply board is mounted on a second aluminium mounting plate in the module thus providing protection from electrical noise and heat-sink for power supplies. A distribution of the filters based on an exemplary bioluminescence spectrum [88] is presented in figure 4.21.

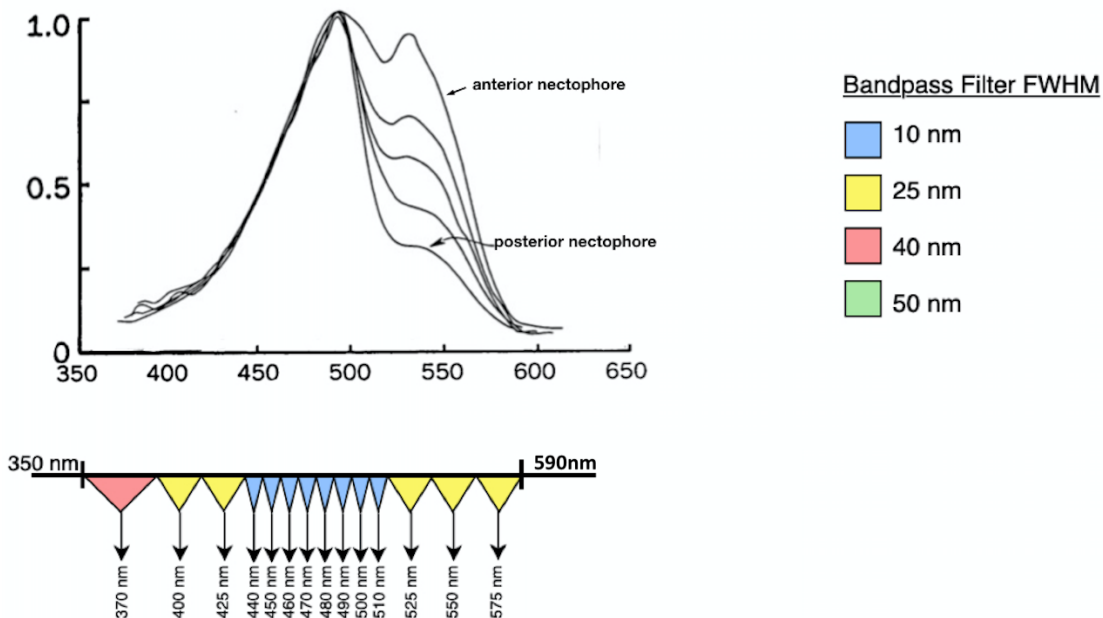


Figure 4.21: Choice range of filters based on an exemplary bioluminescence spectrum taken from [88]. The x-axis is the wavelength in nm and y-axis is the relative intensity

4.6.2 Rate estimation

Spectrometer modules in STRAW-b are motivated by the high rates (\sim MHz) seen by the sDOM PMTs in the STRAW detector. Keeping in mind the quantum efficiency of the PMT R1924A, superimposing on it the exemplary bioluminescence spectrum from [88], then multiplying this value with the transmittances of the chosen bandpass filters and the effec-

tive solid angle seen by by them, and scaling down with the area (3 inch in sDOM to 1 inch in this module), one can estimate the rate that the spectrometer module will see given the rate measured by the sDOM. The effective area ratio between the sDOM PMT and the spectrometer PMT is about ~ 10 . The effective solid angle seen by the sDOM is about 4.5 sr, while it is only 0.2 for the Spectrometer PMTs. This is due to the maximal angles that have to be respected for light entering the filters ($\pm 15^\circ$). Figure 4.22 and 4.23 show the quantum efficiency curve of the PMT and the bioluminescence spectrum used for calculations.

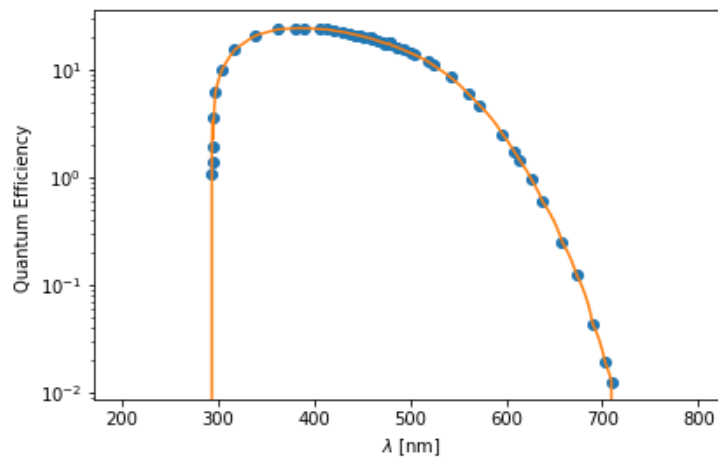


Figure 4.22: *Quantum efficiency of the PMT R1924A [103].*

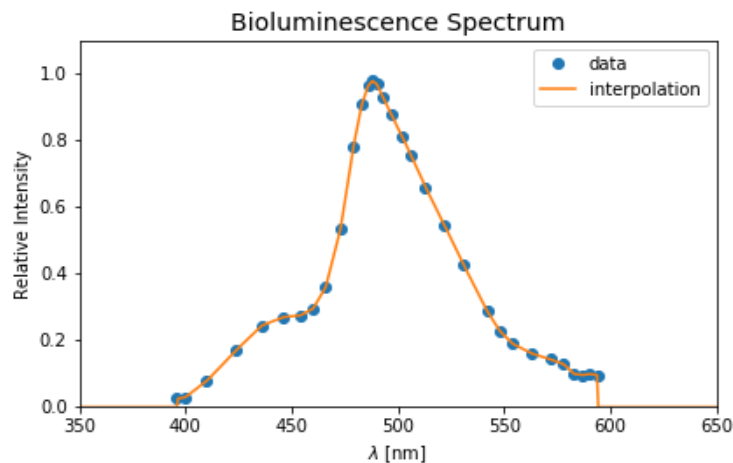


Figure 4.23: *Bioluminescence spectrum of nectophores [88].*

Figure 4.24 shows the transmittances of all the bandpass filters that will be used in this module. These plots have been generated using a plot

digitizer from the data of Edmund Optics [17].

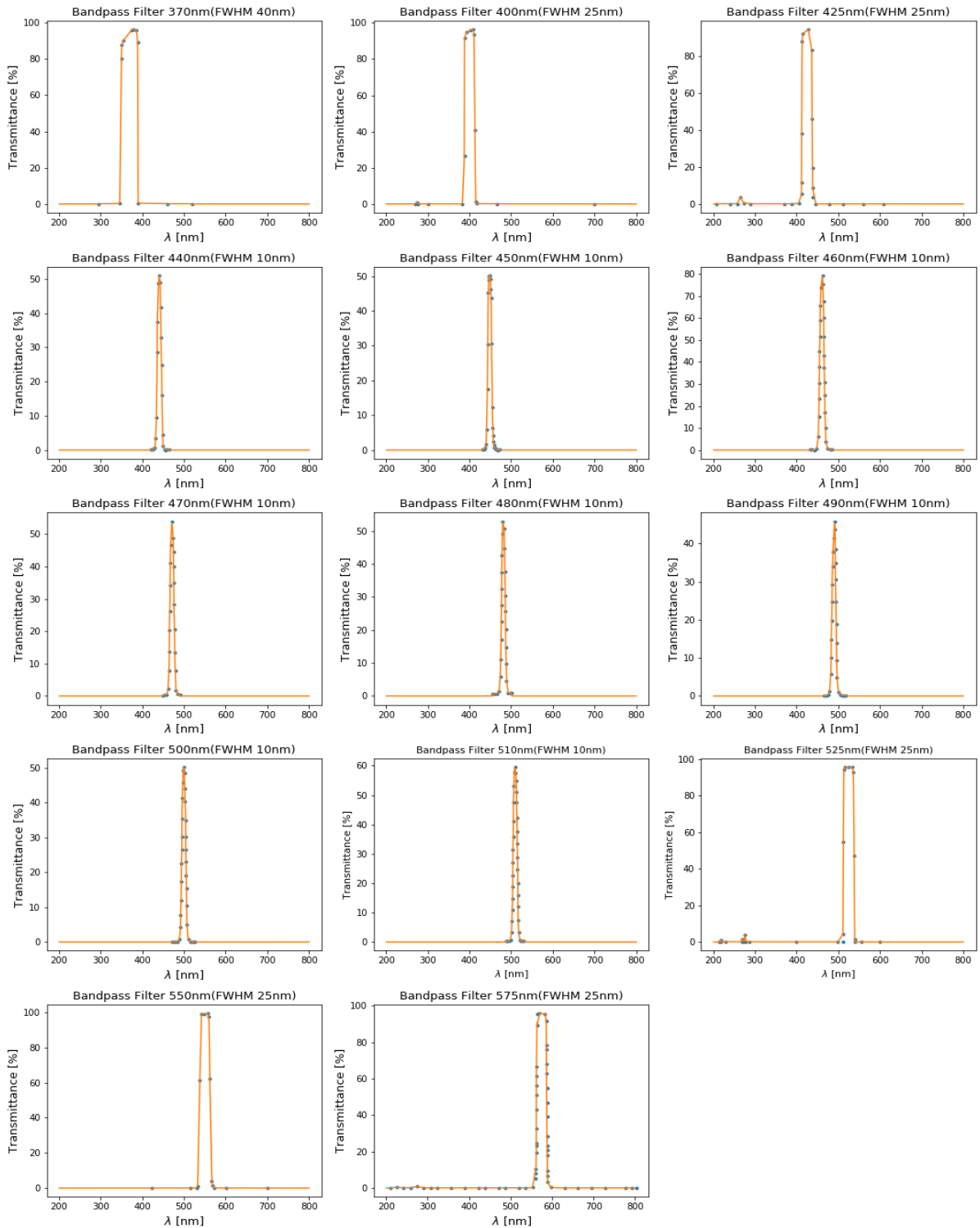


Figure 4.24: Transmittances of all the bandpass filters used [17].

Finally, figure 4.25 gives the simulated rate estimation seen by the PMT

spectrometer and its comparison to the sDOM rate. The area under the curves give the respective rates.

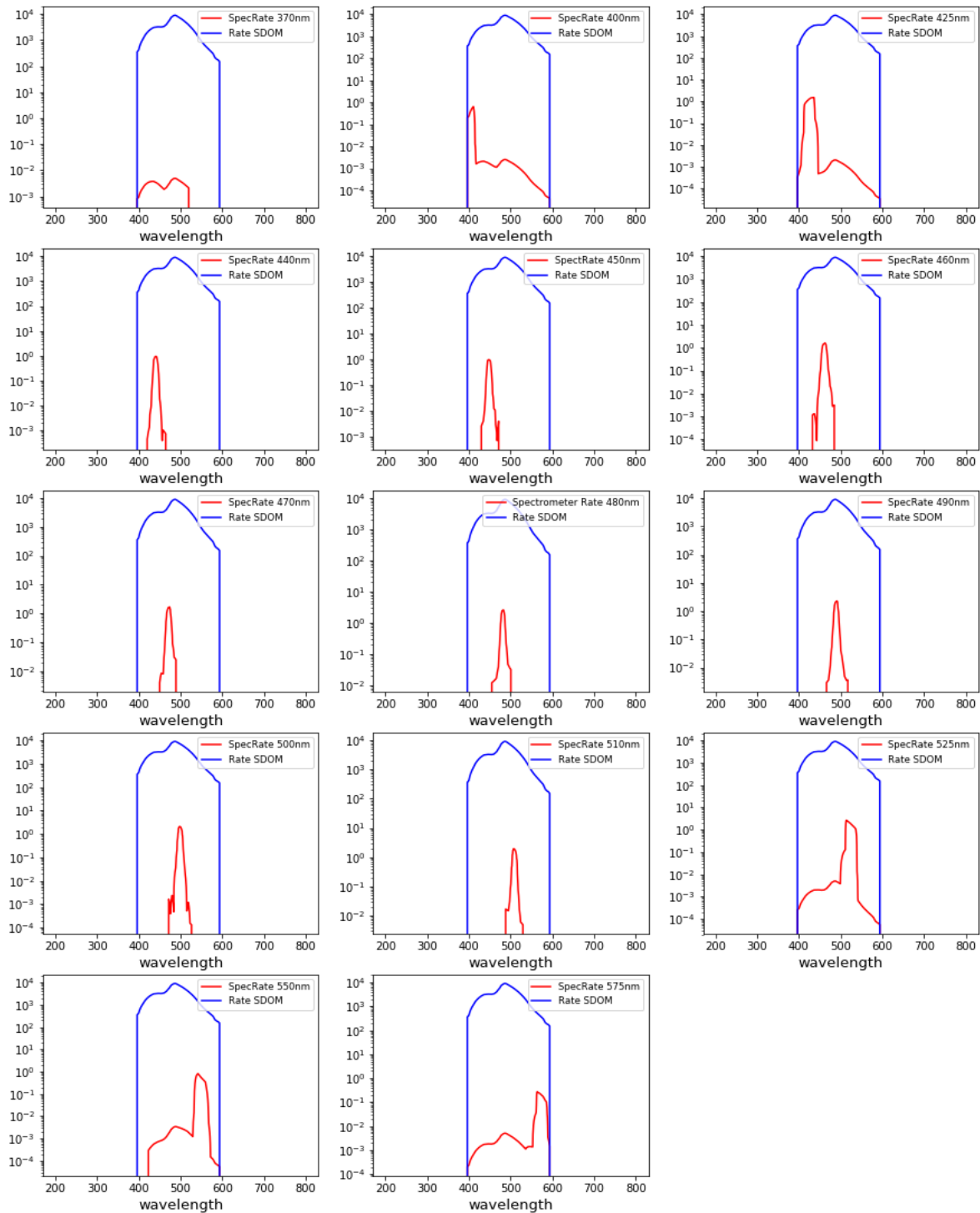


Figure 4.25: Rate comparison between STRAW sDOMs and PMT spectrometer. Here x-axis is the wavelength in nm and y-axis represents the rate in Hz.

Rate of SDOM: 1 Mhz

Expected rate seen by the Spectrometer for 370nm: 0.63 Hz
 Expected rate seen by the Spectrometer for 400nm: 12.06 Hz
 Expected rate seen by the Spectrometer for 425nm: 52.00 Hz
 Expected rate seen by the Spectrometer for 440nm: 16.88 Hz
 Expected rate seen by the Spectrometer for 450nm: 16.85 Hz
 Expected rate seen by the Spectrometer for 460nm: 31.35 Hz
 Expected rate seen by the Spectrometer for 470nm: 29.92 Hz
 Expected rate seen by the Spectrometer for 480nm: 42.53 Hz
 Expected rate seen by the Spectrometer for 490nm: 38.83 Hz
 Expected rate seen by the Spectrometer for 500nm: 36.15 Hz
 Expected rate seen by the Spectrometer for 510nm: 34.14 Hz
 Expected rate seen by the Spectrometer for 525nm: 80.23 Hz
 Expected rate seen by the Spectrometer for 550nm: 26.04 Hz
 Expected rate seen by the Spectrometer for 575nm: 8.88 Hz

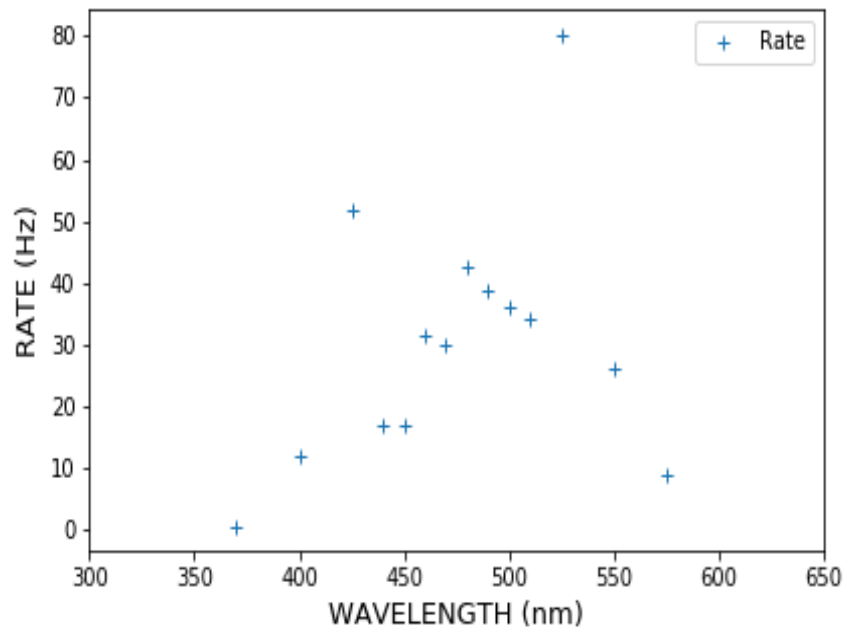


Figure 4.26: Rate estimation at different wavelngths

It can be inferred that since the bioluminescent flashes from pyrosomes vary between 10^{10} and 10^{12} photons emitted over a duration of 1–15 s [109], this could produce sufficient rates to be detected by the PMTs of

the spectrometer module. The expected rate seen by the spectrometer module for different wavelengths can be seen in Figure [4.26](#).

Further development of the STRAW-b modules is still in progress, results for which would be gradually released in other publications. Currently, the estimated year of deployment of this project is 2020.



Conclusion

The STRAW detector has started the characterization of the deep Pacific Ocean at the Cascadia Basin off the coast of Vancouver Island in Canada since August 2018. This work talks briefly about the design, construction and deployment of the STRAW instrumentation. A detailed characterization of the gain, linearity, dark rates and transit time spread of the photomultiplier tubes used in the STRAW digital optical modules (sDOM) was also presented. After investigating the rates from the sDOM it was inferred that extremely high rates in the sDOM could be caused by the bioluminescence produced by deep sea organisms. This led to building a potential upgrade of STRAW called STRAW-b. STRAW-b is the follow-up mooring line for STRAW and serves as a test mooring line for the potential large scale neutrino detector - "P-ONE" (Pacific Ocean Neutrino Explorer). STRAW-b will be a 450 m long string with 10 modules - 5 of which are standard modules and the other 5 will be specialized modules. This work will also briefly cover the preliminary design and investigation of the two proposed spectrometer modules. Further analysis is still in progress. The main goals of STRAW-b will be to test a scalable and safe deployment strategy for the 450m long string and even further characterisation of the optical properties of the ocean with focus on bioluminescence.



Bibliography

- [1] URL: <http://hep.bu.edu/~superk/solar.html>.
- [2] URL: <https://www.km3net.org/>.
- [3] Active galactic nuclei: Cosmos. URL: <http://astronomy.swin.edu.au/cosmos/A/ActiveGalacticNuclei>.
- [4] Blazar optical sky survey (boss) project. URL: http://observatory.phys.uoa.gr/research_blazars_gr.html.
- [5] C12880ma mems u-spectrometer. URL: <https://groupgets.com/campaigns/411-c12880ma-mems-u-spectrometer-round-20?archived=true>.
- [6] Characteristic x-rays. URL: <http://hyperphysics.phy-astr.gsu.edu/hbase/quantum/xrayc.html>.
- [7] Cherenkov effect. URL: http://www.radioactivity.eu.com/site/pages/Cherenkov_Effect.htm.
- [8] Cosmic neutrinos. URL: <https://neutrinos.fnal.gov/sources/cosmic-neutrinos/>.
- [9] Cosmic ray energies: Cosmos. URL: <http://astronomy.swin.edu.au/cosmos/c/cosmicrayenergies>.
- [10] Detector structure: Super-kamiokande official website. URL: <http://www-sk.icrr.u-tokyo.ac.jp/sk/detector/index-e.html>.
- [11] Dr. karl remeis-sternearte astronomisches institut der universität erlangen-nürnberg. URL: <https://www.sternwarte.uni-erlangen.de/reimis-start/research/x-ray-astronomy/active-galactic-nuclei/>.
- [12] Experimental technique: Super-kamiokande official website. URL: <http://www-sk.icrr.u-tokyo.ac.jp/sk/detector/cherenkov-e.html>.
- [13] Gamma-ray burst captured in unprecedented detail. URL: <https://astronomynow.com/2017/07/27/gamma-ray-burst-captured-in-unprecedented-detail/>.
- [14] Gamma-ray bursts. URL: <https://imagine.gsfc.nasa.gov/science/objects/bursts1.html>.
- [15] Geoneutrinos. URL: <https://neutrinos.fnal.gov/sources/geoneutrinos/>.
- [16] Greisen-zatsepin-kuzmin limit: Cosmos. URL: <http://astronomy.swin.edu.au/cosmos/G/Greisen-Zatsepin-KuzminLimit>.
- [17] Hard coated bandpass filters edmund optics. URL: <https://www.edmundoptics.com/f/hard-coated-od-4-10nm-bandpass-filters/13837/>.

- [18] H.e.s.s. URL: <https://www.mpi-hd.mpg.de/hfm/HESS/pages/about/telescopes/>.
- [19] A hybrid detector. URL: <https://www.auger.org/index.php/observatory/auger-hybrid-detector>.
- [20] Inverse compton scattering. URL: <https://www.nuclear-power.net/nuclear-power/reactor-physics/interaction-radiation-matter/interaction-gamma-radiation-matter/compton-scattering/inverse-compton-scattering/>.
- [21] Km3net: a telescope at the bottom of the sea. URL: https://www.ntvn.nl/magazines/2016-3/KM3NeT_1.html.
- [22] Neutrino flavors. URL: <https://neutrinos.fnal.gov/types/flavor/#basics>.
- [23] Neutrinos from supernovae. URL: <http://hep.bu.edu/~superk/gc.html>.
- [24] Neutron stars, pulsars, and magnetars. URL: https://imagine.gsfc.nasa.gov/science/objects/neutron_stars1.html.
- [25] Overview: Super-kamiokande official webiste. URL: <http://www-sk.icrr.u-tokyo.ac.jp/sk/sk/index-e.html>.
- [26] Photomultiplier tube r12199. URL: <https://www.hamamatsu.com/jp/en/product/type/R12199/index.html>.
- [27] Processes that create cosmic gamma rays. URL: https://imagine.gsfc.nasa.gov/science/toolbox/gamma_generation.html.
- [28] Pulsar wind nebulae. URL: <https://portal.cta-observatory.org/Pages/Pulsar-Wind-Nebulae.aspx>.
- [29] Pulsars and supernova remnants. URL: <http://www.physics.usyd.edu.au/sifa/rcfta/anrep94/anrep94/node18.html>.
- [30] Quasar: Cosmos. URL: <http://astronomy.swin.edu.au/cosmos/Q/Quasar>.
- [31] Solar neutrinos. URL: <https://neutrinos.fnal.gov/sources/solar-neutrinos/>.
- [32] Supernova neutrinos. URL: <https://neutrinos.fnal.gov/sources/supernova-neutrinos/>.
- [33] Supernova remnant. URL: <https://www.britannica.com/science/supernova-remnant>.
- [34] Supernova remnant: Cosmos. URL: <http://astronomy.swin.edu.au/cosmos/S/SupernovaRemnant>.
- [35] Supernova remnants. URL: https://imagine.gsfc.nasa.gov/science/objects/supernova_remnants.html.
- [36] What physical processes generate gamma rays? URL: <https://heasarc.gsfc.nasa.gov/docs/cgro/epo/vu/overview/whatare/process.html>.
- [37] What's a blazar? URL: <https://www.blazarventures.com/whats-a-blazar>.
- [38] Čerenkov light: Studio alicino. URL: <https://www.studioalicino.it/it/node/265>.
- [39] Cern accelerating science, 1912. URL: <https://timeline.web.cern.ch/events/victor-hess-discovers-cosmic-rays>.
- [40] Cosmic rays, 1912. URL: http://abyss.uoregon.edu/~js/glossary/cosmic_rays.html.

- [41] Icy life working with russia's underwater 'cosmic eye', Sep 2010. URL: <https://www.bbc.co.uk/news/science-environment-11384614>.
- [42] The early universe toward the beginning of time, Feb 2011. URL: <https://pages.uoregon.edu/jimbrau/astr123-2011/Notes/Chapter27.html>.
- [43] Pulsar wind nebulae. <https://phys.org/news/2016-11-pulsar-nebulae.html>, Nov 2016.
- [44] Air shower (physics), Nov 2018. URL: [https://en.wikipedia.org/wiki/Air_shower_\(physics\)#References](https://en.wikipedia.org/wiki/Air_shower_(physics)#References).
- [45] Pulsar wind nebula, Apr 2018. URL: https://en.wikipedia.org/wiki/Pulsar_wind_nebula.
- [46] Active galactic nucleus, Apr 2019. URL: https://en.wikipedia.org/wiki/Active_galactic_nucleus#Particle_acceleration.
- [47] Baikal deep underwater neutrino telescope, Apr 2019. URL: https://en.wikipedia.org/wiki/Baikal_Deep_Underwater_Neutrino_Telescope#cite_note-1.
- [48] Cosmic neutrino background, Jun 2019. URL: https://en.wikipedia.org/wiki/Cosmic_neutrino_background.
- [49] Cosmic ray, Jun 2019. URL: https://en.wikipedia.org/wiki/Cosmic_ray.
- [50] Gamma-ray astronomy, Jul 2019. URL: https://en.wikipedia.org/wiki/Gamma-ray_astronomy.
- [51] Gamma-ray burst, Jul 2019. URL: https://en.wikipedia.org/wiki/Gamma-ray_burst.
- [52] Geoneutrino, Mar 2019. URL: <https://en.wikipedia.org/wiki/Geoneutrino>.
- [53] Neutrino, Jul 2019. URL: <https://en.wikipedia.org/wiki/Neutrino#Supernovae>.
- [54] Solar neutrino, May 2019. URL: https://en.wikipedia.org/wiki/Solar_neutrino.
- [55] Supernova remnant, Jun 2019. URL: https://en.wikipedia.org/wiki/Supernova_remnant.
- [56] Synchrotron radiation, Apr 2019. URL: https://en.wikipedia.org/wiki/Synchrotron_radiation.
- [57] Weak interaction, Jul 2019. URL: https://en.wikipedia.org/wiki/Weak_interaction#Interaction_types.
- [58] MG Aartsen, K Abraham, M Ackermann, J Adams, JA Aguilar, M Ahlers, M Ahrens, D Altmann, T Anderson, I Anseau, et al. Icecube-gen2-the next generation neutrino observatory at the south pole: Contributions to icrc 2015. *arXiv preprint arXiv:1510.05228*, 2015.
- [59] AU Abeysekara, R Alfaro, C Alvarez, JD Álvarez, R Arceo, JC Arteaga-Velázquez, HA Solares, AS Barber, BM Baughman, N Bautista-Elivar, et al. The hawc gamma-ray observatory: Observations of cosmic rays. *arXiv preprint arXiv:1310.0072*, 2013.
- [60] J Abraham, P Abreu, M Aglietta, C Aguirre, EJ Ahn, D Allard, I Allekotte, J Allen, P Allison, J Alvarez-Muñiz, et al. The fluorescence detector of the pierre auger observatory. *Nuclear Instruments and Methods in Physics Research Section A: Accelerators, Spectrometers, Detectors and Associated Equipment*, 620(2-3):227–251, 2010.
- [61] Juan A Aguilar. Particle astrophysics. URL: https://w3.iihe.ac.be/~aguilar/PHYS-467/PA5_notes.pdf.
- [62] Hadiseh Alaeian. An introduction to cherenkov radiation. *Erişim Tarihi*, 2(12):2017, 2014.

- [63] G Alimonti, C Arpesella, H Back, M Balata, D Bartolomei, A De Bellefon, G Bellini, J Benziger, A Bevilacqua, D Bondi, et al. The borexino detector at the laboratori nazionali del gran sasso. *Nuclear Instruments and Methods in Physics Research Section A: Accelerators, Spectrometers, Detectors and Associated Equipment*, 600(3):568–593, 2009.
- [64] Ingo Allekotte, AF Barbosa, P Bauleo, C Bonifazi, B Civit, CO Escobar, B García, G Guedes, M Gómez Berisso, JL Harton, et al. The surface detector system of the pierre auger observatory. *Nuclear Instruments and Methods in Physics Research Section A: Accelerators, Spectrometers, Detectors and Associated Equipment*, 586(3):409–420, 2008.
- [65] F Arqueros, F Blanco, and J Rosado. Analysis of the fluorescence emission from atmospheric nitrogen by electron excitation, and its application to fluorescence telescopes. *New Journal of Physics*, 11(6):065011, 2009.
- [66] AV Avrorin, VM Aynutdinov, IA Belolaptikov, D Yu Bogorodsky, NM Budnev, R Wischnewski, ON Gaponenko, KV Golubkov, OA Gress, TI Gress, et al. An experimental string of the nt1000 baikal neutrino telescope. *Instruments and Experimental Techniques*, 54(5):649, 2011.
- [67] Philipp Baerwald, Mauricio Bustamante, and Walter Winter. Are gamma-ray bursts the sources of ultra-high energy cosmic rays? *Astroparticle Physics*, 62:66–91, 2015.
- [68] G Bellini, A Ianni, L Ludhova, Fabio Mantovani, and WF McDonough. Geo-neutrinos. *Progress in Particle and Nuclear Physics*, 73:1–34, 2013.
- [69] Adam Bernstein, Mary Bishai, Edward Blucher, David B Cline, Milind V Diwan, Bonnie Fleming, Maury Goodman, Zbigniew J Hladysz, Richard Kadel, Edward Kearns, et al. Report on the depth requirements for a massive detector at homestake. *arXiv preprint arXiv:0907.4183*, 2009.
- [70] M Boehmer, J Bosma, D Brussow, L Farmer, C Fruck, R Gernhäuser, A Gärtner, D Grant, F Henningsen, S Hiller, et al. Straw (strings for absorption length in water): pathfinder for a neutrino telescope in the deep pacific ocean. *Journal of Instrumentation*, 14(02):P02013, 2019.
- [71] J Boger, RL Hahn, JK Rowley, AL Carter, B Hollebhone, D Kessler, I Blevis, F Dalnoki-Veress, A DeKok, J Farine, et al. The sudbury neutrino observatory. *Nuclear Instruments and Methods in Physics Research Section A: Accelerators, Spectrometers, Detectors and Associated Equipment*, 449(1-2):172–207, 2000.
- [72] Hendrik Buiteveld, JHM Hakvoort, and M Donze. Optical properties of pure water. In *Ocean Optics XII*, volume 2258, pages 174–183. International Society for Optics and Photonics, 1994.
- [73] T Chiarusi and M Spurio. High-energy astrophysics with neutrino telescopes. *The European Physical Journal C*, 65(3-4):649–701, 2010.
- [74] Stirling A Colgate and Richard H White. The hydrodynamic behavior of supernovae explosions. *The astrophysical journal*, 143:626, 1966.
- [75] IceCube Collaboration et al. Neutrino emission from the direction of the blazar txs 0506+ 056 prior to the icecube-170922a alert. *Science*, 361(6398):147–151, 2018.
- [76] The T2K Public Website Committee. Neutrino detection. URL: <http://t2k-experiment.org/neutrinos/neutrino-detection/>.
- [77] The T2K Public Website Committee. Neutrino sources. URL: <http://t2k-experiment.org/neutrinos/sources-and-experiments/>.
- [78] The T2K Public Website Committee. Neutrino sources. URL: <http://t2k-experiment.org/neutrinos/sources-and-experiments/>.

- [79] The T2K Public Website Committee. Neutrino sources. URL: <http://t2k-experiment.org/neutrinos/sources-and-experiments/>.
- [80] The T2K Public Website Committee. Neutrino sources. URL: <http://t2k-experiment.org/neutrinos/sources-and-experiments/>.
- [81] Doug Cowen, Azadeh Keivani, and Derek Fox. The icecube observatory detects neutrino and discovers a blazar as its source, Dec 2018. URL: <https://theconversation.com/the-icecube-observatory-detects-neutrino-and-discovers-a-blazar-as-its-source-99720>.
- [82] Heino D Falcke, Michiel P van Haarlem, A Ger de Bruyn, Robert Braun, Huub JA Röttgering, Benjamin Stappers, Wilfried HWM Boland, Harvey R Butcher, Eugène J de Geus, Leon V Koopmans, et al. A very brief description of lofar—the low frequency array. *Proceedings of the International Astronomical Union*, 2(14):386–387, 2006.
- [83] R Franke. A new approach to the search for point-like sources of cosmic neutrinos at peV energies with amanda-ii. 2007.
- [84] S Fukuda, Y Fukuda, T Hayakawa, E Ichihara, M Ishitsuka, Y Itow, T Kajita, J Kameda, K Kaneyuki, S Kasuga, et al. The super-kamiokande detector. *Nuclear Instruments and Methods in Physics Research Section A: Accelerators, Spectrometers, Detectors and Associated Equipment*, 501(2-3):418–462, 2003.
- [85] Dipl.-Phys. Stefan Funk. *A new population of VHE gamma ray sources detected with H.E.S.S. in the inner part of the milky way*. PhD thesis, Ruprecht-Karls-University Heidelberg, 2005.
- [86] Andreas Gärtner. *Development of an optical sensor system for the characterization of Cascadia Basin, Canada*. PhD thesis, Technical University of Munich, 2018.
- [87] Claus Grupen. *Astroparticle physics*. Springer Science & Business Media, 2005.
- [88] Steven HD Haddock and JF Case. Bioluminescence spectra of shallow and deep-sea gelatinous zooplankton: ctenophores, medusae and siphonophores. *Marine Biology*, 133(3):571–582, 1999.
- [89] Steven HD Haddock, Mark A Moline, and James F Case. Bioluminescence in the sea. 2009.
- [90] Bettina Hartmann. Reconstruction of neutrino-induced hadronic and electromagnetic showers with the antares experiment. *arXiv preprint astro-ph/0606697*, 2006.
- [91] Qader Dorosti Hasankiadeh, Pierre Auger Collaboration, et al. Radio detection of air showers at the pierre auger observatory. In *Journal of Physics: Conference Series*, volume 632, page 012005. IOP Publishing, 2015.
- [92] Felix Henningsen. Optical characterization of the deep pacific ocean: Development of an optical sensor array for a future neutrino telescope. 2019.
- [93] Felix Henningsen. Straw (strings for absorption length in water): pathfinder for a neutrino telescope in the deep pacific ocean. In *EPJ Web Conf.*, volume 207, page 06006, 2019.
- [94] I.C.Rea. Pd2018 proceedings. URL: https://indico.ipmu.jp/event/166/contributions/2789/attachments/2153/2640/Rea_I.C._STRAW_PD18.pdf.
- [95] Kun Jia and Rodica Elena Ionescu. Measurement of bacterial bioluminescence intensity and spectrum: Current physical techniques and principles. In *Bioluminescence: Fundamentals and Applications in Biotechnology-Volume 3*, pages 19–45. Springer, 2015.
- [96] Martin Jurkovič, K Abraham, K Holzapfel, K Krings, E Resconi, and J Veenkamp. A precision optical calibration module (pocam) for icecube-gen2. In *EPJ Web of Conferences*, volume 116, page 06001. EDP Sciences, 2016.

- [97] T Kajita, E Kearns, M Shiozawa, Super-Kamiokande Collaboration, et al. Establishing atmospheric neutrino oscillations with super-kamiokande. *Nuclear Physics B*, 908:14–29, 2016.
- [98] Takaaki Kajita. Atmospheric neutrinos and discovery of neutrino oscillations. *Proceedings of the Japan Academy, Series B*, 86(4):303–321, 2010.
- [99] Takaaki Kajita. Atmospheric neutrinos. *Advances in High Energy Physics*, 2012, 2012.
- [100] Oleg E Kalashev, Alexander Kusenko, and Warren Essey. Pev neutrinos from intergalactic interactions of cosmic rays emitted by active galactic nuclei. *Physical review letters*, 111(4):041103, 2013.
- [101] Kappes. Humboldt-universität zu berlin - mathematisch-naturwissenschaftliche fakultät - experimentelle elementarteilchenphysik, Mar 2013. URL: <https://www.physik.hu-berlin.de/de/eephys/icecube>.
- [102] Peter Kiraly. Two centenaries: The discovery of cosmic rays and the birth of lajos jánossy. In *Journal of Physics: Conference Series*, volume 409, page 012001. IOP Publishing, 2013.
- [103] HAMAMATSU PHOTONICS KK. Photomultiplier tube r1924a. 2010.
- [104] John Lee. *Bioluminescence, the Nature of the Light*. 01 2017.
- [105] Alicia López Oramas and Enrique Fernández Sánchez. Multi-year campaign of the gamma-ray binary ls i+ 61^o 303 and search for vhe emission from gamma-ray binary candidates with the magic telescopes. 2014.
- [106] Christoph Nodes. *Particle Acceleration in Pulsar Wind Nebulae*. PhD thesis, Fakultät für Physik, Ludwig-Maximilians-Universität München, 2007.
- [107] Sirin Odrowski. *Neutrino triggered Target of Opportunity (NToO) gamma-ray observations triggered by IceCube: Development of the alert trigger*. PhD thesis, Fakultät für Mathematik und Physik, Leibniz University Hannover, May 2008.
- [108] Hamamatsu Photonics. Micro-spectrometer c12880ma, 2015.
- [109] Imants G Priede, Alan Jamieson, Amandine Heger, Jessica Craig, and Alain F Zuur. The potential influence of bioluminescence from marine animals on a deep-sea underwater neutrino telescope array in the mediterranean sea. *Deep Sea Research Part I: Oceanographic Research Papers*, 55(11):1474–1483, 2008.
- [110] Nola Taylor Redd. Icecube: Unlocking the secrets of cosmic rays, Jul 2018. URL: <https://www.space.com/41170-icecube-neutrino-observatory.html>.
- [111] A Gallo Rosso, Carlo Mascaretti, Andrea Palladino, and Francesco Vissani. Introduction to neutrino astronomy. *The European Physical Journal Plus*, 133(7):267, 2018.
- [112] Frank G Schröder, L Pankov, V Lenok, E Osipova, NM Budnev, A Haungs, T Huege, RR Mirgazov, O Fedorov, A Pakhorukov, et al. Overview on the tunka-rex antenna array for cosmic-ray air showers. Technical report, SISSA, 2017.
- [113] Daniel I. Scully. *Neutrino Induced Coherent Pion Production*. PhD thesis, The University of Warwick.
- [114] Patrick Slane. Pulsar wind nebulae. *arXiv preprint arXiv:1703.09311*, 2017.
- [115] Johannes Schumann Bachelor Thesis. *Simulation Study of Spectral Absorption Lengths in Seawater using 40K Decay*. PhD thesis, Friedrich-Alexander-University Erlangen-Nurnberg, 2018.

- [116] Satyendra Thoudam, JP Rachen, A van Vliet, A Achterberg, S Buitink, H Falcke, and JR Hörandel. Cosmic-ray energy spectrum and composition up to the ankle: the case for a second galactic component. *Astronomy & Astrophysics*, 595:A33, 2016.
- [117] HPKK Photomultiplier Tubes. Assemblies. *For Scintillation Counting and High Energy Physics*. URL [http://www.hamamatsu.com/resources/pdf/etd/High energy PMT TPMZ0003E.pdf](http://www.hamamatsu.com/resources/pdf/etd/High%20energy%20PMT%20TPMZ0003E.pdf), 2000.
- [118] Photomultiplier Tubes. Basics and applications. *Hamamatsu Photonics KK, Iwata City*, pages 438–0193, 2006.
- [119] Michael Unger. P o s (i c r c 2 0 1 7) 1 1 0 2 highlights from the pierre auger observatory. 2017.
- [120] Jacco Vink. Non-thermal bremsstrahlung from supernova remnants and the effect of coulomb losses. *Astronomy & Astrophysics*, 486(3):837–841, 2008.
- [121] Natalie Wolchover and Quanta Magazine. Ultrahigh-energy cosmic rays traced to hotspot. URL: <https://www.quantamagazine.org/ultrahigh-energy-cosmic-rays-traced-to-hotspot-20150514/>.